UNIVERSITY OF CALIFORNIA
RIVERSIDE

Experimental Study and Development of Rare Earth Iron Garnets as Pure Spin-Current Sources

A Dissertation submitted in partial satisfaction
of the requirements for the degree of

Doctor of Philosophy

in

Physics

by

Víctor Hugo Ortiz Hernández

December 2019

Dissertation Committee:

Dr. Jing Shi, Chairperson
Dr. Jory Yarmoff
Dr. Harry Tom

The Dissertation of Víctor Hugo Ortiz Hernández is approved:

Committee Chairperson

University of California, Riverside

Acknowledgments

After all these years, I culminate my PhD formation at UC Riverside. There have been all kind of moments, from the sad ones to the exhilarating ones, which all have contributed in one way or another in my formation process. In the next lines I want to acknowledge to all the people who played a role during this stage, which without them this achievement would not have been possible.

First of all, I want to acknowledge my advisor Dr. Jing Shi for his instruction and guidance during my PhD program. His insight and experience were always present, and his hunger for knowledge was an inspiration to keep pushing in this quest for acquiring a little bit more understanding about physics and nature.

I want also to recognize my committee members, Dr. Jory Yarmoff and Dr. Harry Tom, who provided useful comments and suggestions during the development of this project. I would like to mention also the contributions of Dr. Vivek Aji and Dr. Jianlin Liu as part of my qualifying exam committee.

This work would have been quite more difficult to achieve without the contribution of my laboratory colleagues, who assisted me during the whole research process. In no particular order, I would like to thank Junxue Li, Wei Yuan, Mohammed Aldosary, Yadong Xu, Zilong Jiang, Chi Tang, Zhisheng Lin, Bowen Yang, Mohammed Alghamdi, Yawen Liu, Mark I. Lohmann, Tang Su and Mason Biggerstaff. I want to thank also my colleagues from

other groups: Bassim Arkook, Fariborz Kargar, Mina Rashetnia, Arezoo Etesamirad, Paul Lou, Howard Chiang, Fatemeh Barati, John Spalding, Jack C. Tang, Xiong Huang, Edwin Preciado, Adrian Nosek, Rodolfo Rodríguez and Juan Aguilera. I want to acknowledge the visiting scholars in our group: Benjamin Madon, Zhong Shi, Jhen-Yong Hong and Shen Wang.

I would like to thank to our collaborators who provided invaluable assistance and insight: Dr. Cui-zu Chang and Yifan Zhao from PSU, Dr. Igor Barsukov, Dr. Rich Wilson and Michael Gómez from UCR, Dr. Kang L. Wang, Qiming Shao and Gen Yin from UCLA, Dr. Javier E. Garay, Chad Warren, Pathikumar Sellappan and Yasuhiro Kodera from UCSD.

For their technical support, I want to recognize Dong Yan, Frank Lee, Dexter Humphrey, John Butler, Nissim Amos and Mark Heiden in the Center for Nanoscale Science and Engineering; Dan Borchardt in the Analytical Chemistry Instrumentation Facility; Perry Cheung in the Marlan and Rosemary Bourns College of Engineering; Krassimir Bozhilov from the Central Facility for Advanced Microscopy and Microanalysis and Juan Bahena from Quantum Design. I want to thank also Derek E. Beving, Mayela Castillo, Carol Lynn González, Jhon González, Jazmin Chávez from Physics Department, and Glenda Barraza and Dorothea Northcutt from SHINES center for their invaluable help.

I want to thank COMEXUS, who provided financial support via the Fulbright – García Robles fellowship.

A special mention and enormous appreciation to Arturo Ledesma and Tatiana Hernández, who kindly opened their home and provided me with their friendship and support while establishing in the US.

I would like to greatly acknowledge to my longtime friends Héctor E. Gómez and David García, who have provided the necessary support to survive the PhD. I also want to thank Dr. Pedro A. R. M. Solórzano, who helped me in adapting to the American style of life and shared special moments in UCR. Also, I want to thank Juan A. Yoshino, Pável D. Sulca, Carlos E. López, Raúl Escamilla, Martín Romero, José Luis Pérez, Manuel Quintana, Raúl W. Gómez, José E. Marquina, Érick Guzmán, Leonardo R. Ramírez, Alan U. Ascencio, J. Ismael López, Grissel Montes, Alejandro Adame, Elisa Morales, Mario Saucedo, Eric Chau and to all people who in one way or another give emotional support during this process.

To M. Margarita López Titla, you have my love and gratitude for your understanding and support during these times.

And last but not least, I want to express my gratitude to my parents, Jesús Librado Ortiz y Castañeda and Elsa Hernández Olivo for their support, encouragement, advice and love during this process. I want also to acknowledge my sister Cynthia Aurora and my brother Jesús “Chuy” for their encouragement, to César Guerrero and to all my extended family who supported me during my PhD program.

Acknowledgment of previously published material

1. Part of Chapter 2: was published in “Víctor H. Ortiz*, Mohammed Aldosary*, Junxue Li, Yadong Xu, Mark I. Lohmann, Pathikumar Sellappan, Yasuhiro Kodera, Javier E. Garay and Jing Shi, **Systematic control of strain-induced perpendicular magnetic anisotropy in epitaxial europium and terbium iron garnet thin films**. *APL Materials*, *6*(12), 121113 (2018).

ABSTRACT OF THE DISSERTATION

Experimental Study and Development of Rare Earth Iron Garnets as Pure Spin-Current Sources

by

Víctor H. Ortiz

Doctor of Philosophy, Graduate Program in Physics
University of California, Riverside, December 2019
Dr. Jing Shi, Chairperson

The advent of spintronics in 1988 represents a step forward in the development of high efficiency electronics. Adding the spin degree of freedom allows the design of new technologies that do not require charge motion in a device, which translates in lower energy dissipation, for this reason ferromagnetic insulators have played an important role in the research of new spintronic applications.

Rare earth iron garnets are a type of ferromagnetic insulators which physical and chemical characteristics make them the ideal candidates for their use in spintronic research, for this reason is of great importance to understand their properties to exploit them to their full potential.

The first chapter covers an introduction to spintronics and rare earth iron garnets as candidates for their application on the development of new technologies, the basic concepts of spintronics are covered in this section.

In chapter two it is covered the concept of magnetic anisotropy and its control by thickness dependence in rare earth iron garnet thin films. Here, it is demonstrated that by exerting an adequate strain in the lattice structure of the rare earth iron garnet it is possible to align its magnetization perpendicular to the sample plane, and that the magnitude of this effect can be systematically tuned by the thickness of the rare earth iron garnet thin film.

In chapter three the effect of lattice strain in the dynamic magnetic properties of europium iron garnet are analyzed. The strain on the films is applied by lattice mismatch by the use of different garnet substrates, and then subsequently studied by ferromagnetic resonance technique, which provides important information about the dynamics of spin wave propagation. In this experiment, it was found that the intrinsic damping, which is associated to the energy dissipation of a spin wave, is independent of the lattice strain.

Finally, in chapter four the use of rare earth iron garnets as a source of pure spin currents is examined. By setting up spin Seebeck effect and spin pumping experiments, the spin wave transmission through different configurations and posterior charge conversion on materials with large spin-orbit coupling are studied.

Table of Contents

List of figures

Chapter 1: Introduction

Section 1.1: Rare earth Iron garnets

Generally speaking, garnets are a group of minerals that have the general chemical formula $X_3Q_2R_3O_{12}$, its basic crystal structure is a cube with eight formula units per unit cell. The Q cations occupy octahedral sites within the structure (called *a*-sites), while the R cations occupy tetrahedral sites (*d*-sites). The X ion is surrounded by eight oxygen ions located at the corners of a dodecahedron (in reality, it is more like a skewed cube), the site it fills is called a *c*-site (Figure 1-1). Naturally, the *d*-sites are filled with tetravalent

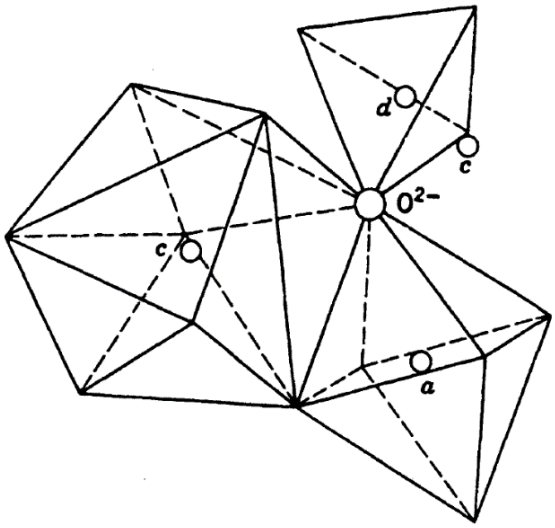

***Figure 1-1 Iron Garnet crystal structure**. Diagram of the positions of the a, c and d sites surrounding an O^{2-} ion. Adapted from Morrish, A.H. The Physical Principles of Magnetism, Wiley-IEEE Press, (1965).*

ions, the c-sites are occupied by divalent ions while the a-sites are host trivalent atoms. In the first half of the 20th century, a family of synthetic garnets were created, where the

c- and *d*-sites were populated with certain trivalent ions. The introduction of Fe^{3+} ions to the *a*- and *d*- sublattices resulted in an insulating garnet with magnetic properties. The most important of these garnets has the chemical formula $Y_3Fe_2Fe_3O_{12}$, which is commonly referred as YIG (*yttrium iron garnet*).

In YIG the magnetic ions (Fe^{3+}) occupy the *a* and *d* sublattices, the way these ions are arranged with respect with the O^{2-} ions promotes a rather large superexchange interaction between these two sites; on the other hand the interaction between sites of the same kind is negligible, for these reason the magnetizations of the *a* and *d* sublattices will be antiparallel [1].

Another kind of magnetic rare earth iron garnet (REIG) is where the Y^{3+} ion is replaced by another rare earth ion in the lanthanide series. Opposed to the Y^{3+} ions, which have a closed shell electronic configuration and therefore do not have magnetic moment contribution, most of the REIGs have some magnetic moment into the garnet structure. From the way ions are accommodated, the *c*-site will experience a superexchange interaction with the *d*-site, however this will be smaller than the interaction between *a*- and *d*-sites, this will cause that the coupling between rare earth and iron sublattices will be weak, with both *c*- and *d*-sites having antiparallel magnetization contributions.

As a result, the spontaneous magnetization for YIG only comes from the Fe^{3+} ions, each one contributing with a magnetic moment equal to 5 μ_B, therefore the total magnetic moment at 0 K is expected to be $(N_d - N_a)m_{Fe} = (3-2)\times 5\ \mu_B = 5\mu_B$ per formula unit, this

results is in agreement with the result obtained experimentally [2]. For the case of REIGs, the outer shell electrons will contribute with both orbital (L) and spin (S) angular momenta to the magnetic moment according to Hund's rules. The total magnetic moment contribution coming from the c-site on REIGs can be obtained from the Russell-Saunders coupling scheme, by $\mu = g_j\sqrt{J(J+1)}\mu_B$, where $g_J = \frac{3}{2} + \frac{S(S+1)-L(L+1)}{2J(J+1)}$, with $J = L - S$ for less than half filled and $J = L + S$ for more than half filled electron subshell. Being said this, for some of the heavier rare earth elements their contribution to the total magnetic moment increases dramatically when temperature decreases [3]. The temperature at which the magnetic moment of the *c* sublattice is equal to the resultant of the *a* and *d* sublattices is called the compensation temperature(Figure 1-2). Above this temperature, the total magnetic moment will be parallel to that of the *d* sublattice.

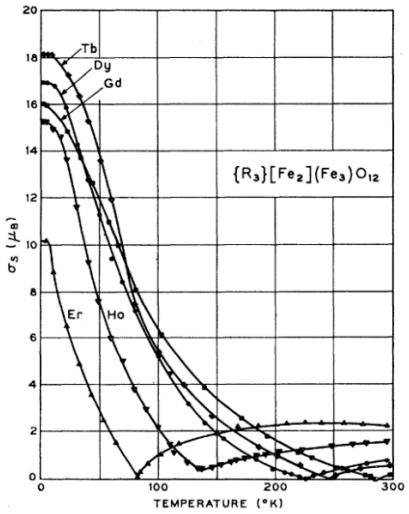

Figure 1-2 Compensation temperatures in rare earth iron garnets. *Experimental values for spontaneous magnetization vs temperature for some of the heavy rare earth iron garnets, showing clearly the compensation temperature. From Geller S. et al. Phys. Rev.* ***137*** *3A (1965).*

Section 1.2: Dynamic magnetic response: ferromagnetic resonance

When a magnetic field that is being applied to a sample changes, the magnetization of the sample is perturbed in response, relaxing in a short time to the new equilibrium state. The major changes occur by the rotation of the intrinsic magnetization $\vec{M}$ (where its magnitude remains constant), this process is followed by an irreversible flow of energy which dampens the rotation of $\vec{M}$ governing the rate of the magnetizing processes. The mathematical model that describes the motion of $\vec{M}$ in response to an effective magnetic field $\vec{H}$ is given by the Landau-Lifshitz equation

$$\frac{d\vec{M}}{dt} = -\gamma\vec{M} \times \vec{H} - \lambda\vec{M} \times \left(\vec{M} \times \vec{H}\right) \tag{1-1}$$

where γ is the magnetogyric ratio and λ the phenomenological damping parameter, this term is usually written in the form $\lambda = \alpha\frac{\gamma}{|\vec{M}|}$, being α a dimensionless factor called the Gilbert damping factor, this parameter is related to the amount of energy dissipated during the precession process. If the equation (1-1) is used to analyze the response to a uniformly magnetized sample to a sudden change in the effective field $\vec{H}$, it can be found that the motion of $\vec{M}$ precesses at a frequency $\omega_o = \gamma H$ about the new field direction, with a relaxation time given by $T = \frac{1}{\alpha\omega_o}$ (Figure 1-3).

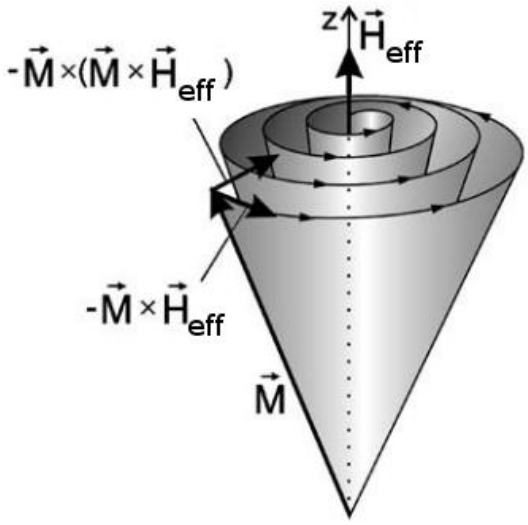

Figure 1-3 Magnetization precession relaxation. *Relaxation of the precession of the magnetization $\vec{M}$, according to Landau-Lifshitz equation. Adapted from Lenz, K. et al. Phys. Rev. B.**73** 14 (2006).*

A more convenient way to study the motion $\vec{M}$ and/or the damping that it experiences is provided by *ferromagnetic resonance* (FMR), which consists in inducing $\vec{M}$ into resonance by applying a high frequency (in the GHz range) magnetic field *h* perpendicular to $\vec{H}$, under that condition $\vec{M}$ will precess around the effective magnetic field H_{eff} at the frequency ω of the field *h*. By varying the magnitude of $\vec{H}$ the precession frequency ω_o is changed as well, and $\vec{M}$ will undergo into resonance under the appropriate external field H_{res} , which will depend on the contributions to the magnetic environment of the system, such as magnetic anisotropies. The linewidth ΔH of this resonance is given by

$$\Delta H = \frac{2}{\gamma T} = 2\alpha H_{res}. \qquad (1\text{-}2)$$

When single crystal YIG was studied by FMR, it showed a smaller Gilbert damping ($\alpha_{YIG}\sim10^{-4}$) compared to other ferromagnetic materials ($\alpha\sim10^{-2}$). This is a desirable attribute for the development of magnetic technologies, which will be covered in the following chapters.

Section 1.3: Spin currents

The concept of charge current is easy to understand: a flow of charged particles (in most of the cases, electrons) moves along a conducting path due to a potential differential. If now the spin degree of freedom is added, a spin-polarized charge current (i.e., a charge current where the spins of the carriers are all aligned in one direction) will generate an accumulation of spin in the direction of the charge current. As spin is a vector quantity, an equivalent spin-polarized charge current with opposite spin and in the opposite direction will generate the same accumulation of spin as in the first case. If the previous conditions are combined, it is possible then to have a spin accumulation in the medium with no net charge transferred, under these conditions a pure spin current has been achieved [4].

In the case of conducting materials with strong spin-orbit coupling, a charge current can generate a pure transversal spin current that is perpendicular to both charge current and spin-polarization of the current, this process is known as the *Spin Hall Effect (SHE)* (Figure 1-4) [5]. In an analogous way, a pure spin current applied to the same material can generate a charge current, hence this is known as the *Inverse Spin Hall Effect (ISHE)* [6].

A spin current, as opposed to a charge current, is invariant to time reversal, this means that if the time ran backwards, the spin current would still flow in the same direction. Also, as mentioned before, spin is a vector quantity that is associated to angular momentum, thus it has the potential to transmit quantum information along the adequate structures [7].

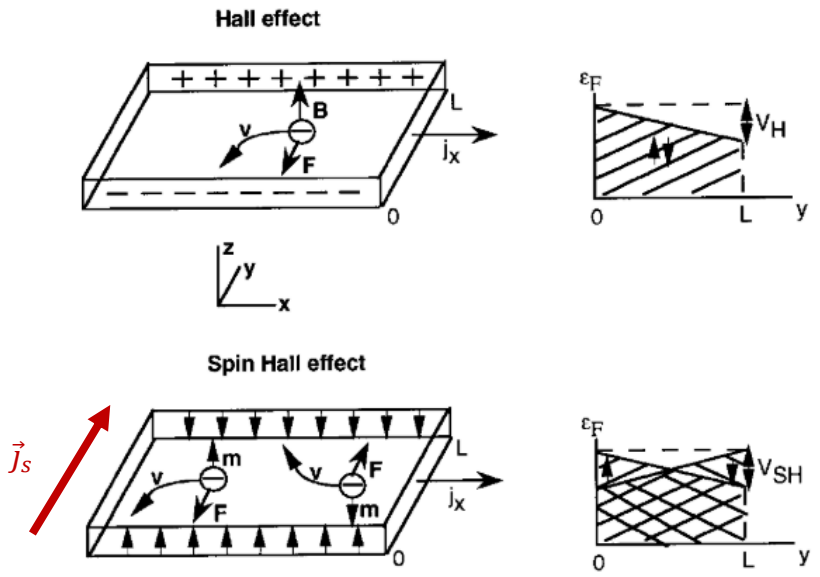

Figure 1-4 Spin Hall Effect. *Analogy between Hall Effect and Spin Hall Effect. In this diagram, the spin polarization is on the z-axis and the charge current in the x-axis, therefore the spin current will be along the y-axis. Adapted from Hirsch J.E. Phys. Rev. Lett.* ***83****, 9 (1999).*

Section 1.4: Spin waves

Like their mechanical counterparts, spin waves can be regarded as collective disturbances in the magnetic ordering of a material. In the case of crystalline rare earth iron garnets, the orientation of neighboring magnetic-dipole moments is strongly coupled and therefore these disturbances can propagate through the crystal array. As it was described

in Section 1.2:, the motion of the magnetization vector is precessional, however, as the disturbance propagates along the material the phase of this precession changes, thus generating the spin wave (Figure 1-5). The frequency of this spin wave is dependent of the exchange energy (which is increased because the magnetic dipole moments in the crystal are no longer collinear), and from the magnetic self-energy associated with the non-zero divergence of $\vec{M}$ due to the wave.

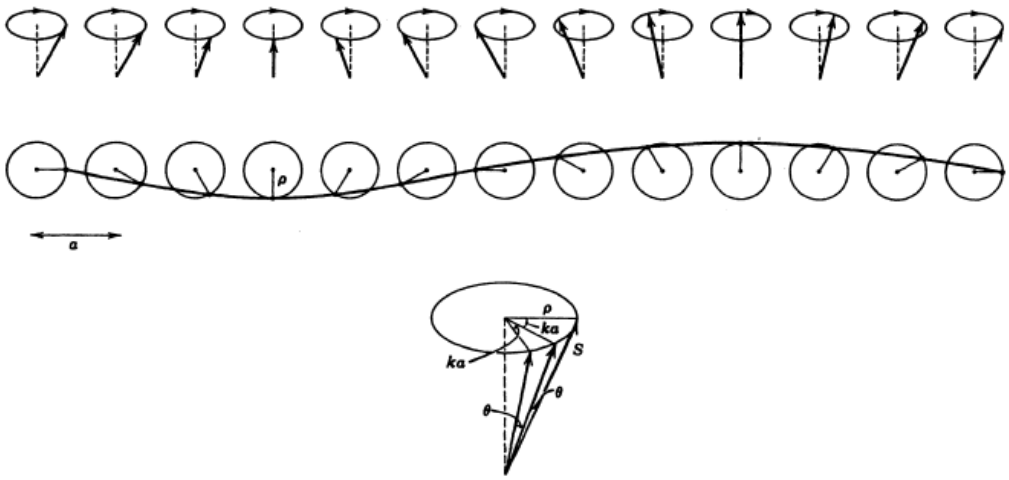

Figure 1-5 Spin wave. *Illustration of a spin wave with wave vector k, being a the lattice spacing of the magnetic sublattice. The bottom image illustrates the angular relationships between three successive magnetic sites. Adapted from Morrish, A.H. The Physical Principles of Magnetism, Wiley-IEEE Press, (1965).*

A spin wave can also be treated as a particle with associated energy E_k and momentum p_k that obeys Bose - Einstein statistics. In this aspect, spin waves have properties like those of photons and phonons, for this reason a quantized spin wave is also referred as a *magnon*. Magnons in a magnetic material can be generated by microwave excitations,

and they can diffuse by a thermal or density gradient along the same material. Together with spin-polarized charges, magnons are responsible of spin current propagation.

Section 1.5: Rare earth iron garnets and spintronics

The birth of spintronics (a term coined from the term *spin-based electronics*) is considered to be the discovery of the giant magnetoresistive effect (GMR) in 1988 [8], since then GMR has been successfully used in the development of new electronic applications such as spin-valves and magnetic tunnel junctions (MTJs), increasing greatly the capabilities of magnetic storage units like *Magnetic Random Access Memory* (MRAM) devices. However, these technologies still rely on the flow of electrons to transport the desired information, with the associated ohmic dissipative losses. Therefore, a material with insulating properties that retains its magnetic properties is desirable for the development of low power spintronic applications, such material would allow the flow of spin information only. Among ferromagnetic insulators (such as EuS, EuO, $Cr_2Ge_2Te_6$ to name a few), rare earth iron garnets are considered the ideal candidates for this task: they have a large electronic band gap ($\sim$ 2.8 eV), have a high Curie temperature ($T_c \sim$ 500 K, while most of the other ferromagnetic insulators have $T_c <$ 100K), they are chemically stable (i.e., they do not degrade over time due to oxidation like their metallic counterparts), they have low energy dissipation when transmitting spin waves (as a result of low Gilbert damping), they can be easily conformed into thin films for the fabrication of nanoscale devices and last but not least, they offer a robust way to control their magnetic properties either by

thickness, crystal strain or ion substitution in their crystal structure. For these reasons, in the recent years the study of the properties of thin film rare earth iron garnets has attracted the attention of the scientific community, with the subsequent development of spin orbitronics, spin caloritronics and magnon spintronics.

Chapter 2: Tuning of Magnetic Anisotropy in Rare Earth Iron Garnets

Section 2.1: Introduction to magnetic anisotropy

The investigation of thin film magnetic materials where the magnetization vector $\vec{M}$ lays perpendicular to the plane (such condition being known as *perpendicular magnetic anisotropy*, PMA) is of high importance in the design of spintronic devices such as MTJs and MRAMs. As opposed to metallic thin films, rare earth iron garnet films provide a larger versatility in tuning the PMA, allowing a greater flexibility in the development of magnetic technologies.

In a crystalline system, the magnetization of a ferromagnetic specimen is far from being isotropic: it has been found that the magnetization $\vec{M} = M_s\vec{\alpha}$ (being $\vec{\alpha}$ the direction vector of the magnetization) tends to lie along certain crystallographic axes, this effect is known as *crystalline anisotropy*. The crystallographic axes along which the magnetization tends to align are referred as *easy directions* or *easy axes*, on the other hand those along which it is most difficult to align are called *hard directions* or *hard axes*. If the exchange fields are assumed to be large in comparison with the external fields, the magnetic anisotropy free energy *F* can be expressed as

$$F_{MA} = F_o + F_e(\bar{\bar{\varepsilon}}) + F_a(\alpha) + F_{me}(\alpha, \bar{\bar{\varepsilon}}) \tag{2-1}$$

where F_o is a constant with respect to α and the strain tensor $\bar{\bar{\varepsilon}}$, $F_e(\bar{\bar{\varepsilon}})$ represents the pure elastic energy given by the strain tensor $\bar{\bar{\varepsilon}}$, $F_a(\alpha)$ the crystalline anisotropy energy

and $F_{me}(\alpha, \bar{\bar{\varepsilon}})$ is the magnetoelastic component of the energy. In the case of magnetic systems, the term $F_e(\bar{\bar{\varepsilon}})$ is usually smaller than the other parameters and can be disregarded. The term $F_a(\alpha)$, also known as magnetocrystalline energy, is defined as the work requires to rotate the magnetization $\vec{M}$ along a given direction α compared to an easy direction. Finally, the term $F_{me}(\alpha, \bar{\bar{\varepsilon}})$ originates from the interaction of the spin system with the lattice, causing a dependence of the dimensions of magnetic single crystals on the direction of magnetization, this phenomenon is known as *magnetostriction*. On the other hand, it is possible to affect the direction of the magnetization under the presence of a stress σ, in this case this is referred as *magnetoelastic effect*.

The total free energy of a ferromagnetic specimen in an applied magnetic field can written as the sum of the different free energy terms, which includes the energy of the magnetization of the specimen under an applied field H (also referred as Zeeman's energy), the aforementioned magnetic anisotropy energy F_{MA} and the self-energy of the magnetization in its own field, also referred as the demagnetizing energy F_d. In the case of thin films, the demagnetizing energy (which is associated to the shape anisotropy) can be approximated to $F_d = 2\pi M_s^2 \cos^2\theta$ (where M_s is the magnitude of M when the specimen is saturated), the magnetocrystalline anisotropy component to the first order can be approximated to $F_a = K_1 \sin^2\theta$ (being K_1 known as the first anisotropy constant) and the

magnetoelastic anisotropy component can be approximated to $F_{me} = -\frac{3}{2}\lambda\sigma cos^2\theta$, being λ the magnetostriction constant associated to the direction the stress is being applied.

Usually the magnetic anisotropy energy is written together with the shape anisotropy term, leading to

$$F_{MA} = (2\pi M_s^2 - K_u)\, cos^2\,\theta \tag{2-2}$$

where K_u is the uniaxial anisotropy term and englobes the magnetoelastic and crystalline anisotropy components of the anisotropy energy. After minimizing F_{MA} with respect to the angle θ, we define then

$$4\pi M_{eff} = 4\pi M_s - \frac{2K_u}{M_s} \tag{2-3}$$

being $4\pi M_s$ the shape anisotropy field and we define $4\pi M_{eff}$ as the effective in-plane demagnetizing field. The term $\frac{2K_u}{M_s}$ is usually referred as the PMA field $H_{2\perp}$. Because of the shape anisotropy, the magnetization vector $\vec{M}$ will favor an in-plane orientation in a thin film. In order to promote the perpendicular orientation of $\vec{M}$, then it is necessary that $H_{2\perp} > 4\pi M_s$, making the term $4\pi M_{eff} < 0$.

Section 2.2: Systematic Control of Strain-Induced Perpendicular Magnetic Anisotropy in Epitaxial Europium and Terbium Iron Garnets Thin Films

REIG thin films are often grown by pulsed laser deposition (PLD) on crystalline substrates. As mentioned before, under strain-free conditions, the magnetization of a REIG thin film

lies in the film plane because the magnetocrystalline anisotropy is generally smaller than the shape anisotropy which favors the in-plane orientation. However, due to relatively large magnetostriction constant λ, the strain-induced magnetic anisotropy energy can be even more important in thin films. This property gives epitaxial growth of REIG films a unique advantage in controlling magnetic anisotropy. Depending on the sign of λ, suitable substrates can be chosen to not only manipulate the magnitude, but also the sign of the total magnetic anisotropy energy, therefore the orientation of the magnetization vector. For example, for positive (negative) λ, compressive (tensile) strain is required to drive the magnetization normal to the film plane, which can be accomplished by controlling lattice mismatch in the pseudomorphic growth regime. The same mechanism was used for ferromagnetic metal thin films, but the interfacial strain quickly relaxes as the film thickness increases, consequently the so-called spin reorientation transition occurs only at some very small thickness (e.g., a few monolayers) [9] [10]. REIGs in general have larger Burger's vectors, $\boldsymbol{b}$ which give rise to larger dislocation formation energies than metals (energy scales with $|\boldsymbol{b}|^2$); therefore, the interfacial strain at garnet interfaces can extend to a larger thickness range, which makes the film thickness an additional knob to control the magnetic anisotropy in REIG films.

In order to orient the magnetization normal to the film, the PMA field $H_{2\perp}$ must be positive and larger than the demagnetizing field as it was established earlier. For the case of strained films grown on (100) and (111)-oriented substrates, $H_{2\perp}$ is given by

$$H_{2\perp} = \frac{2K_1 - 3\lambda_{100}\sigma_{\parallel}}{M_S} \quad (2\text{-}4)$$

$$H_{2\perp} = \frac{-4K_1 - 9\lambda_{111}\sigma_{\parallel}}{3M_S}, \quad (2\text{-}5)$$

where K_1 is the first-order cubic anisotropy constant, $\sigma_{\parallel}$ is the in-plane stress and λ_{lmn} is the magnetostriction constant for the film grown in the [*lmn*] direction. From these equations, it follows that $H_{2\perp}$ can be controlled by tuning the in-plane stress of the film, which can be achieved by controlling growth.

In previous experiments [11] [12], it has been demonstrated that $Tm_3Fe_5O_{12}$ (TmIG) can acquire strong PMA by inducing an interfacial tensile strain, since the magnetostriction constant for TmIG is negative for films grown on substituted gadolinium gallium garnet (SGGG) in [111] direction. For the cases of $Eu_3Fe_5O_{12}$ (EuIG) and $Tb_3Fe_5O_{12}$ (TbIG), the magnetostriction constants at room temperature are $\lambda_{100} = 21\times10^{-6}$, $\lambda_{111} = 1.8\times10^{-6}$ for EuIG; and $\lambda_{100} = -3.3\times10^{-6}$, $\lambda_{111} = 12\times10^{-6}$ for TbIG [13]; therefore, a compressive strain is required for all cases except TbIG (001). Given that a reasonable strain (<1%) can be accommodated for pseudomorphic growth of the film on the substrate, the candidates chosen for this study are gadolinium gallium garnets (GGG) in different orientations, i.e., GGG(001)/EuIG and GGG (111)/TbIG. The lattice mismatch between these REIG films and GGG gives rise to the compressive strain that is needed for a strong PMA field. Since the strain relaxes in thicker films, the average strain in films determines the magnetic anisotropy, hence we accomplish the full anisotropy tuning by leveraging both the substrate structure and the REIG film thickness.

Thin films were grown by PLD from targets densified from powders synthesized using similar methods as described before [14]. High quality ultra-flat EuIG and TbIG films, with thickness ranging from 4 nm to 180 nm for EuIG, and 5 nm to 100 nm for TbIG, were deposited on (001)- and (111)-oriented GGG substrates respectively. After the standard cleaning process, the substrates were baked at ~ 220°C for five hours with a base pressure < 10^{-6} Torr before EuIG or TbIG deposition. After this annealing process, the substrates were then annealed at ~ 600°C under a 1.5 mTorr oxygen pressure with 12% (wt. %) ozone for 30 minutes; then under these oxygen and temperature conditions, a 248 nm KrF excimer laser pulse was set to strike the target with a power of 156 mJ and at a repetition rate of 1 Hz. After deposition, the films were annealed *ex situ* at 800°C for 200 seconds under a steady flow of oxygen using rapid thermal annealing (RTA).

To characterize the structural properties of the deposited garnets, reflection high energy electron diffraction (RHEED) was used to track the evolution of the film growth. Right after deposition, RHEED shows the absence of any crystalline order. After the *ex situ* RTA process, RHEED patterns appear for both EuIG and TbIG, revealing a single crystal structure for all the samples (Figure 2-1(a)). Atomic force microscopy (AFM) was performed on all grown samples, indicating uniform and atomically flat films with low root-mean-square (RMS) roughness (<2 Å RMS) and with no superficial defects (Figure 2-1(b)). The absence of three-dimensional islands on the surface from AFM measurements confirms the uniformity of the thin films.

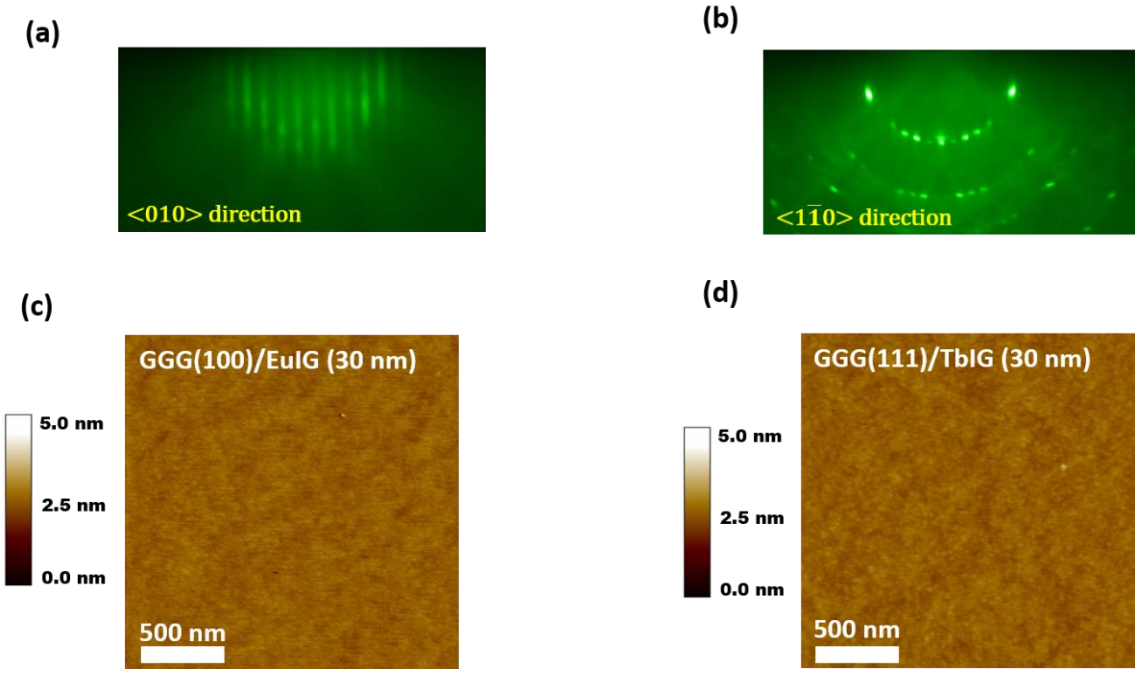

Figure 2-1 Crystal and morphology characterization of EuIG and TbIG thin films. *(a) and (b): RHEED patterns of (a) EuIG along <010> direction and (b) TbIG along <1$\bar{1}$0> direction. Both show single crystal structure after annealing. (c) and (d): $2\mu m \times 2\mu m$ AFM surface morphology scans of EuIG (30nm) thin film (c) with RMS roughness of 1.13 Å and TbIG (30 nm) thin film (d) with RMS roughness of 1.34 Å.*

X-ray diffraction (XRD) was performed on all the samples to further confirm their crystalline structure, using a PANalytical Empyrean diffractometer with Cu K_α radiation and a Ni filter, at room temperature in 0.002° steps in the 2θ range of 10°-90°. For the EuIG samples, two main peaks for EuIG and GGG were observed, corresponding to the (004) and (008) Bragg peaks, while for the TbIG samples one main peak for TbIG and GGG is observed, corresponding to the (444) Bragg peak, thus confirming epitaxy and the single crystal structure of both films. For both EuIG and TbIG cases, no secondary phases were observed. These results (XRD, AFM and RHEED) combined corroborate the high quality of the obtained films.

Magnetic hysteresis curves (*M* vs. *H*) were obtained on the grown films using a vibrating sample magnetometer (VSM) at room temperature with the applied magnetic fields normal and parallel to the plane (Figure 2-2). From the raw data, the linear paramagnetic background from the GGG substrate was subtracted. For the EuIG samples, a clear easy-axis loop can be observed for fields perpendicular to the plane for thickness *t* up to 38 nm, while the in-plane hysteresis loop shows a hard axis behavior, thus indicating the strong PMA in these samples. For t > 56 nm, a transition from easy- to hard-axis loop can be observed for fields perpendicular to plane (Figure 2-2(a)). This behavior can be attributed to the gradual relaxation of the strain of the films as the thickness increases, until $H_{2\perp}$ is comparable with or less than the demagnetizing field. For the case of TbIG films, an easy-axis hysteresis loop can be observed in all films up to 100 nm for magnetic fields perpendicular to the plane, and a hard-axis loop for in-plane magnetic fields (Figure 2-2(b)). In contrast to the EuIG thin films case, the TbIG thin films preserve the strong PMA over the entire thickness range (up to 100 nm). As the product of the magnetostriction constant and in-plane lattice strain($\lambda_{lmn}\sigma_{\parallel}$) is generally larger in EuIG than in TbIG, the apparently larger $H_{2\perp}$ in TbIG can be attributed to the smaller saturation magnetization in TbIG compared to EuIG (to be discussed later).

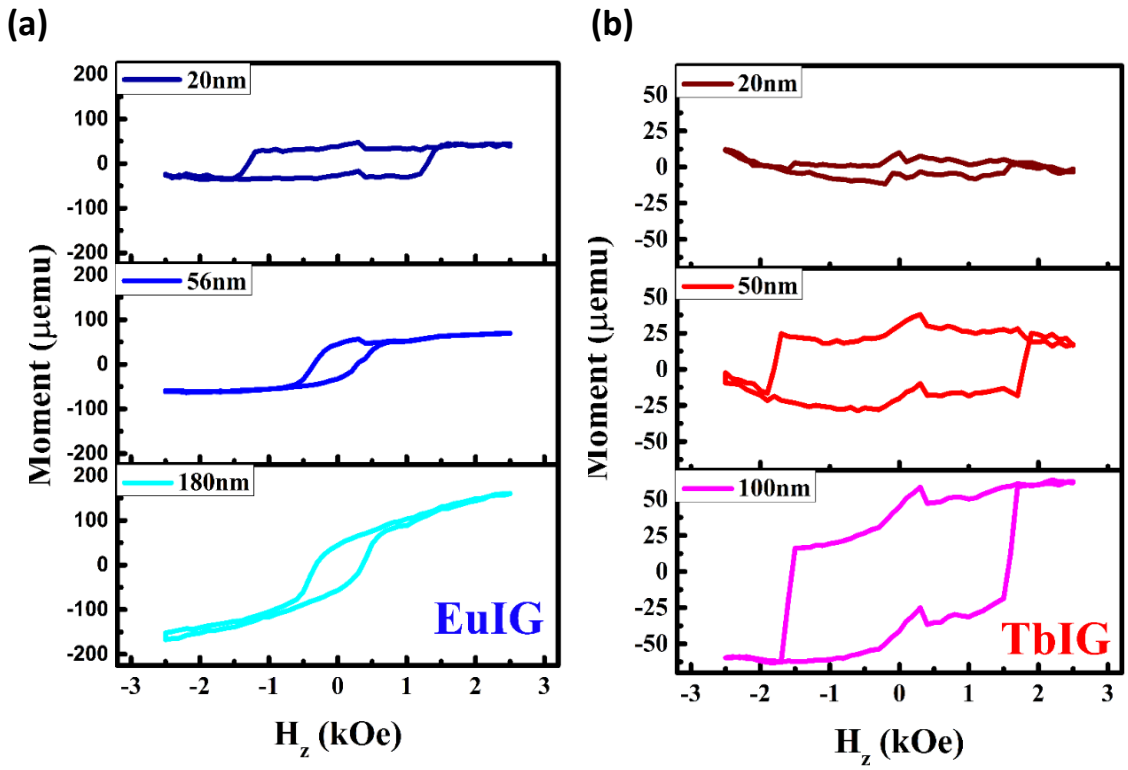

Figure 2-2 Magnetic hysteresis loop evolution to film thickness. *Magnetic hysteresis curves for out-of-plane applied field (H_z) for different film thicknesses of (a) EuIG (b) TbIG. For EuIG, the transition from easy axis to hard axis due to strain relaxation can be observed.*

The hysteresis loops for 38 nm EuIG and 100 nm TbIG films are shown in Figure 2-3. These loops clearly indicate PMA in the films. For thinner films, i.e., t < 38 nm for EuIG and t <100 nm for TbIG, both REIGs have stronger PMA. The saturation magnetization for all films is summarized in Table 2-1. For EuIG films with t < 14 nm and for TbIG films with t < 20 nm, the magnetic moment signal is too small to be resolved by the VSM due to the large background signal from GGG and their magnetization data are not included. The average saturation magnetization for EuIG is $4\pi M_s$ = (913 $\pm$ 7) G, which is 23.5% smaller than the reported value for bulk EuIG ($4\pi M_s$ = 1192.83 G) [15], which might be caused by

a variation in stoichiometry as it has been observed in similar studies [16]. For the case of TbIG, the average saturation magnetization is $4\pi M_s$ = (234 $\pm$ 5) G, which is only 3.4% below the reported value for bulk TbIG ($4\pi M_s$ = 242.21 G).

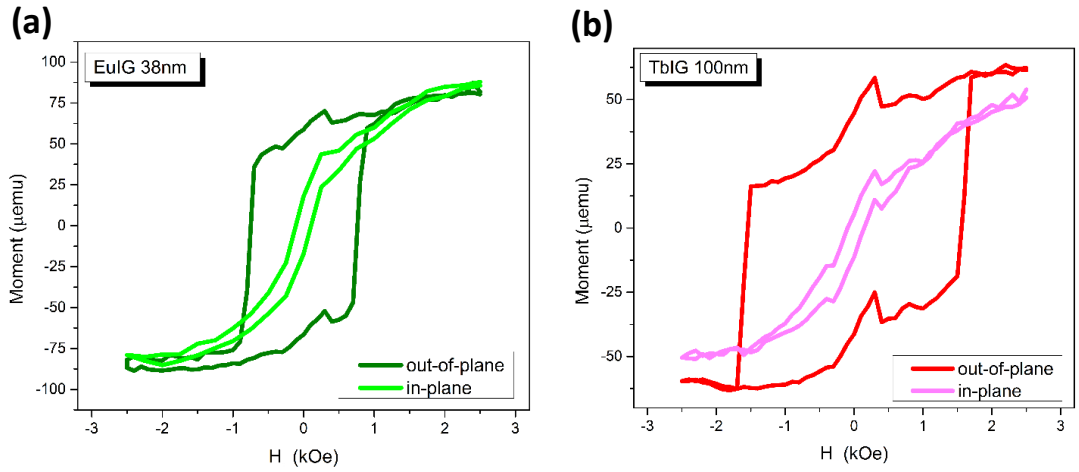

Figure 2-3 Easy axis vs. hard axis VSM measurements on EuIG and TbIG thin films. *Magnetic hysteresis curves for out-of-plane and in-plane applied magnetic field for (a) 38 nm EuIG and (b)100 nm TbIG, where the out-of-plane loops show a clear easy-axis behavior for both films.*

For films with t > 10 nm, the XRD data shows that the Bragg peak corresponding to both REIGs is shifted to the left from the expected peak positions for the respective bulk

crystals (Figure 2-4(a,b)), thus indicating an elongation on the lattice parameter perpendicular to the surface, leading to a compressive in-plane strain in the lattice.

Moreover, a systematic shift to higher 2θ values of the diffraction peaks for both EuIG and TbIG as the thickness of the thin film increases is a direct measurement of the

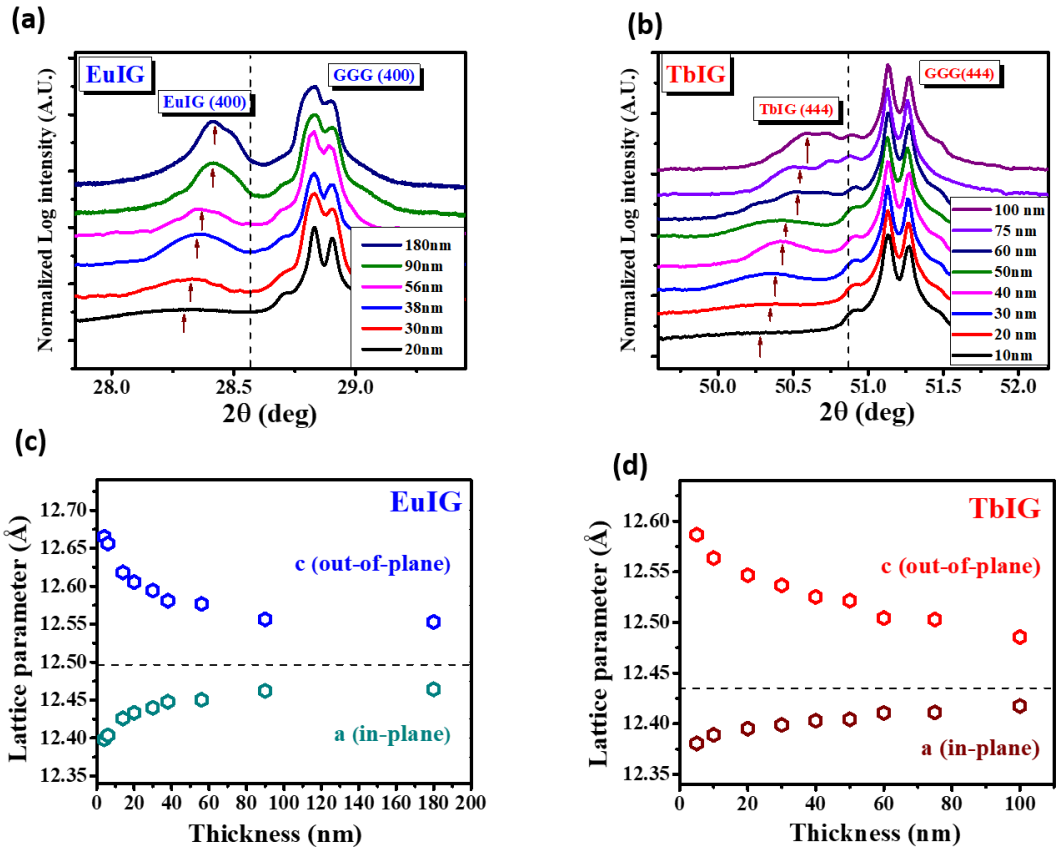

Figure 2-4 Structural characterization in EuIG and TbIG thin films: thickness dependence. *(a) and (b): Normalized semi-log plot of θ-2θ XRD scans of (a) EuIG films of thickness t = 20, 30, 38, 56, 89, 178 nm grown on GGG (100) and (b) TbIG of thickness t= 10, 20, 30, 40, 50, 60, 75 and 100 nm grown on GGG(111) substrate. The dashed line shows the 2θ positions of the bulk material. The arrows indicate the position evolution of (004) peak for EuIG and (444) peak for TbIG as strain relaxes. (c) and (d): Thickness dependence of the out-of-plane lattice constant c and in-plane lattice constant a for EuIG films on GGG(001) (c) and TbIG on GGG(111) (d). The dashed line represents the bulk lattice constant (a=12.497 Å) for EuIG and (a= 12.435 Å) for TbIG.*

relaxation of the lattice parameters towards the bulk values (Figure 2-4(c,d)), in contrast to the results obtained by Rosenberg *et al.* [16]. The surprisingly slow relaxation behavior in REIG thin films contrasts sharply with ferromagnetic metal films, demonstrating a unique magnetic anisotropy control possibility by film thickness.

In order to determine the in-plane stress $\sigma_{\parallel}$ in the garnet films, it is necessary to consider the elastic deformation tensor of the material. When a film with cubic crystalline structure is grown on a single crystal substrate, and assuming the material originally is isotropic, then two strain components can be considered: an in-plane biaxial strain $\varepsilon_{\parallel}$ and an out-plane uniaxial strain $\varepsilon_{\perp}$. These parameters are related through the elastic stiffness constants by [17] [18]

$$\varepsilon_{\parallel} = -\frac{c_{11}}{2\,c_{12}}\,\varepsilon_{\perp} \qquad \text{for film grown on (001) substrate,} \qquad (2\text{-}6)$$

$$\varepsilon_{\parallel} = -\frac{c_{11}+2\,c_{12}+4\,c_{44}}{2c_{11}+4\,c_{12}-4\,c_{44}}\,\varepsilon_{\perp} \qquad \text{for film grown on (111) substrate,} \qquad (2\text{-}7)$$

and

$$\varepsilon_{\perp} = \frac{a_{\perp}-a_o}{a_o} \qquad (2\text{-}8)$$

$a_{\perp}$ being the out-of-plane lattice parameter for the strained film, and a_0 the lattice parameter for the relaxed (bulk) material; $a_{\perp}$ can be obtained from the XRD data according to the equation $a_{\perp} = d_{hkl}\sqrt{h^2+k^2+l^2}$. For the case t < 10 nm, $\varepsilon_{\parallel}$ can be obtained directly from the RHEED pattern. $\sigma_{\parallel}$ can be calculated then by

$$\sigma_{\parallel} = -\frac{c_{11}}{2c_{12}}\left(c_{11} + c_{12} - \frac{2c_{12}^2}{c_{11}}\right)\epsilon_{\perp} \qquad \text{for the (001) case, and} \qquad (2\text{-}9)$$

$$\sigma_{\parallel} = -6c_{44}\frac{c_{11}+2c_{12}}{2c_{11}+4\,c_{12}-4\,c_{44}}\epsilon_{\perp} \qquad \text{for the (111) case,} \qquad (2\text{-}10)$$

where c_{ii} corresponds to the elastic stiffness constants. For EuIG (c_{11} = 25.10×10^{11} dyne/cm^2, c_{12} = 10.70×10^{11} dyne/cm^2, c_{44} = 7.62×10^{11} dyne/cm^2) [19] and TbIG (c_{11} = 26.53×10^{11} dyne/cm^2, c_{12} = 11.07×10^{11} dyne/cm^2, c_{44} = 7.15×10^{11} dyne/cm^2) [20], the values for $\sigma_{\parallel}$ can be calculated then from equations (2-9) and (2-10), which are listed in Table 2-1.

An important factor is the combination of the lattice-mismatch-induced in-plane compressive strain and positive magnetostriction coefficients which can drive the magnetization perpendicular to the film plane in both EuIG and TbIG. As mentioned before, in TmIG, due to negative magnetostriction constant, tensile strain is needed to obtain PMA, which was achieved by growing it on SGGG or NGG substrates. The strong PMA in those garnet films are characterized by squared magnetic hysteresis loops for out-of-plane fields but a hard-axis behavior for in-plane fields. To quantify $H_{2\perp}$ in EuIG and TbIG films, magneto-transport measurements in REIG/Pt bilayers are performed at room temperature, this approach allows us to measure values of anisotropy field as large as 14T, compared to the limited field range presented by typical VSM or SQUID systems; moreover it comes with the advantage that the paramagnetic signal coming from the substrate is neglected using this technique. Since these REIG films are magnetic

insulators, the Hall response of Pt imprints the magnetic anisotropy of the REIG films via the magnetic proximity effect and/or the spin current effect [11]. Therefore, a 5 nm thick Pt layer was sputtered into the Hall bar geometry with a length of l = 600 µm and a width of w = 100 µm using standard photolithography. The inset of Figure 2-5(a) shows the optical image of the Hall bar shape and dimensions. Measured Hall response contains two parts: the ordinary Hall effect (OHE) which is linear in field, and the anomalous Hall effect (AHE) which is proportional to the out-of-plane magnetization. Figure 2-5(a) shows sharp squared out-of-plane AHE hysteresis loops after subtraction of linear background of OHE. These loops resemble M vs. H loops with the easy axis character of TbIG and EuIG

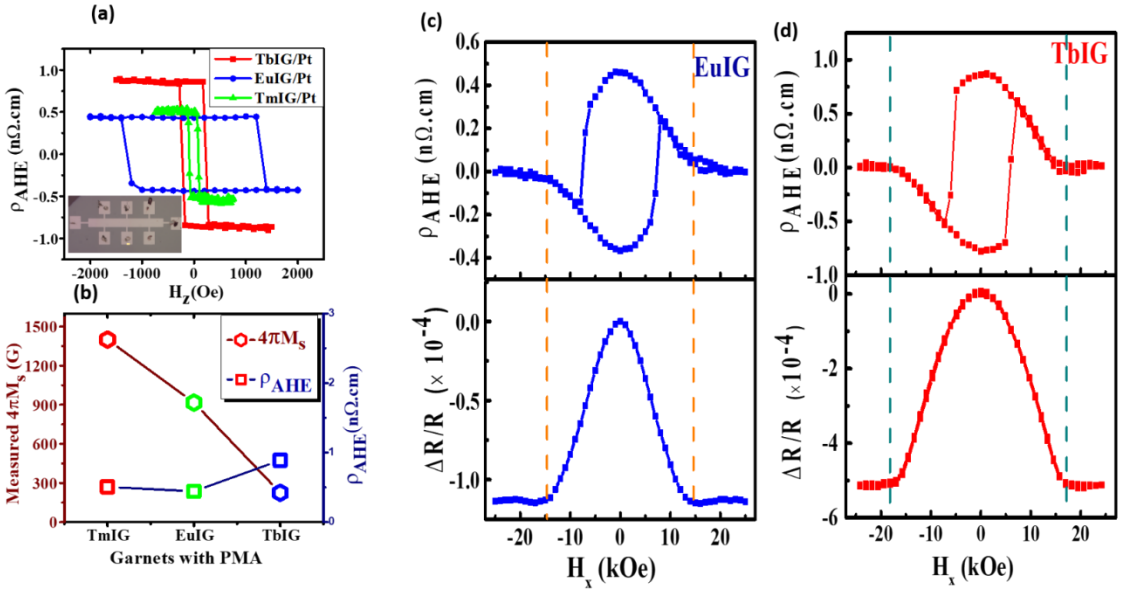

Figure 2-5 Transport measurements in EuIG/Pt and TbIG/Pt heterostructures. *(a) The anomalous Hall resistivity measured with an out-of-plane field sweep for three PMA garnets (TbIG (30 nm)/Pt(5 nm), EuIG(30 nm)/Pt(5 nm) and TmIG(30 nm)/Pt(5 nm)). Inset: Optical microscope image of Hall-bar device with a length of L= 600 µm and a width of w= 100 µm. (b) Measured magnetization values ($4\pi M_S$) and anomalous Hall resistivity magnitude as a function of PMA garnets (TbIG, EuIG and TmIG). (c) and (d) Hall resistivity (ρ_{AHE}) and longitudinal magnetoresistance ratio ($\Delta R/R$) as a function of in-plane magnetic field for (c) EuIG (20 nm)/Pt(5 nm) and (d) TbIG (60 nm)/Pt(5 nm). The dashed lines represent the saturation magnetic field for in-plane geometry.*

taken with an out-of-plane magnetic field (Figure 2-6). Two mechanisms can give origin to the AHE in Pt: 1) by proximity coupling between the REIG and the Pt interfacial layer, acquiring then the behavior of a ferromagnetic metal and thus the hysteresis arises from conventional AHE mechanism, 2) by spin-Hall AHE, which is an effect that originates from spin precession around the exchange field due to the presence of a ferromagnetic layer. In other experiments [11], it has been shown that both mechanisms play a role in the obtained AHE signal. To compare the AHE magnitude, we kept the REIG and Pt thicknesses constant at 30 nm and 5 nm respectively for the two bilayers, and an NGG/TmIG/Pt bilayer as reference. Measured AHE resistivity magnitude (ρ_{AHE}) for the REIG/Pt systems are 0.429, 0.529, and 0.89 $n\Omega \cdot cm$ for EuIG/Pt, TmIG/Pt and TbIG/Pt, respectively. Figure 2-5(b) shows the comparison of both measured $4\pi M_s$ and ρ_{AHE} from Figure 2-5(a) among all three bilayers. The $4\pi M_s$ value is 1400 G for TmIG, 915 G for EuIG,

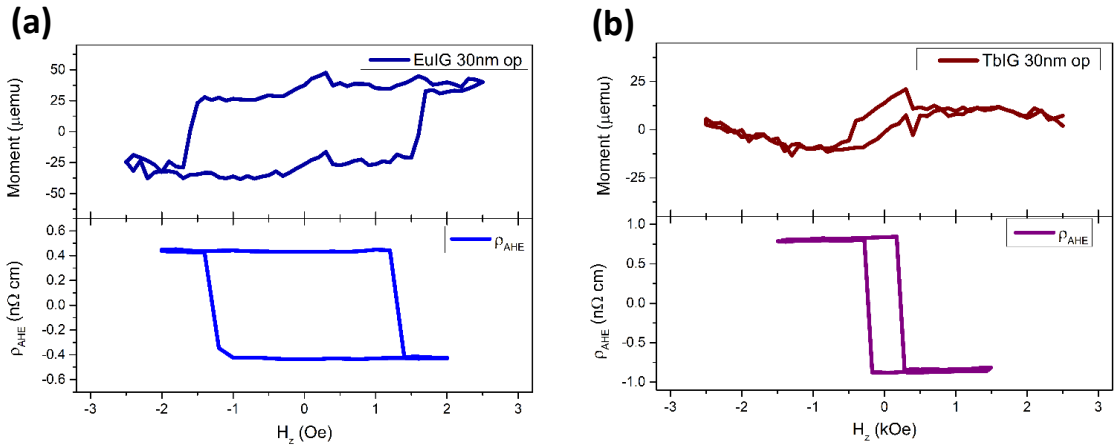

Figure 2-6 VSM vs. AHE measurements for TbIG and EuIG. *Comparison between magnetic hysteresis curves measured by vibrating sample magnetometry for out-of-plane applied field (H_z) and anomalous Hall resistivity measurements for (a) 30 nm EuIG and (b) 30 nm TbIG.*

and 225 G for TbIG. The difference in the magnetization is due to the different magnetic moment of the rare-earth elements which are coupled antiferromagnetically with the net Fe^{3+} moment and causes partial compensation of the net Fe^{3+} moment. Note that ($4\pi M_s$)

GGG (001)/EuIG								
Thickness (nm)	c (Å)	$\varepsilon_\perp$(%)	$\varepsilon_\parallel$(%)	$\sigma_\parallel \times 10^{10}$ dyne/cm^2	$4\pi M_s$ (Gauss)	$4\pi M_{eff}$ (kOe)	$H_{2\perp}$ (kOe)	$K_u \times 10^5$ (erg/cm^3)
4	12.665	1.35	-1.58	-4.21	--	-32.00	32.91*	11.96*
6	12.656	1.28	-1.50	-3.99	--	-24.00	24.91*	8.719*
14	12.618	0.97	-1.14	-3.03	916	-17.50	18.42	6.375
20	12.605	0.87	-1.02	-2.72	899	-14.50	15.40	5.185
30	12.594	0.78	-0.91	-2.44	932	-7.75	8.68	2.874
38	12.581	0.67	-0.79	-2.10	911	-5.00	5.91	1.811
56	12.577	0.64	-0.75	-1.99	879	-3.25	4.13	1.137
90	12.556	0.48	-0.56	-1.49	927	3.50	-2.57	-1.290
180	12.553	0.45	-0.52	-1.40	927	6.00	-5.07	-1.870
GGG (111)/TbIG								
Thickness (nm)	c (Å)	$\varepsilon_\perp$(%)	$\varepsilon_\parallel$(%)	$\sigma_\parallel \times 10^{10}$ (dyne/cm^2)	$4\pi M_s$ (Gauss)	$4\pi M_{eff}$ (kOe)	$H_{2\perp}$ (kOe)	$K_u \times 10^5$ (erg/cm^3)
5	12.587	1.22	-1.16	-3.71	--	-66.50	66.73*	6.213*
10	12.564	1.03	-0.98	-3.14	--	-47.25	47.48*	4.421*
20	12.547	0.90	-0.86	-2.73	253	-36.00	36.25	3.652
30	12.537	0.82	-0.78	-2.48	223	-32.00	32.22	2.852
40	12.525	0.73	-0.69	-2.21	242	-26.75	26.99	2.598
50	12.522	0.70	-0.66	-2.11	221	-20.25	20.47	1.803
60	12.504	0.56	-0.53	-1.69	230	-17.25	17.48	1.603
75	12.503	0.55	-0.52	-1.66	247	-10.25	10.50	1.030
100	12.486	0.41	-0.39	-1.24	222	-8.75	8.97	0.792

Table 2-1 *Structural and magnetic property parameters for epitaxially strained EuIG films with thickness $4 \le t \le 180$ nm on GGG (001) and TbIG films with thickness $5 \le t \le 100$ nm on GGG (111). The $H_{2\perp}$ and K_u values marked with (*) were calculated using the average $4\pi M_s$ values.*

decreases from TmIG to TbIG by a factor of five whereas ρ_{AHE} stays in nearly the same range for all of them. This sharp contrast clearly indicates that the ρ_{AHE} of the Pt layer is correlated with the net magnetic moment of sublattices of Fe^{3+} ions, which is a constant, rather than the total magnetic moment of REIGs (including Fe^{3+} and RE^{3+}). This can be explained by the fact that the conduction electrons of Pt are primarily hybridized with the 3*d* Fe^{3+} electrons which are more spatially extended than the 4*f* electrons of the rare earth elements. As it has been reviewed in Equation (2-3), the magnetic anisotropy energy of thin films in is in function of a K_u term, which as it was mentioned previously englobes the magnetocrystalline anisotropy which can be approximated by the first-order cubic anisotropy constant (K_1). In EuIG and TbIG, (K_1) is negative and ($\approx -\frac{10^4 erg}{cm^3}$); the term $2\pi {M_s}^2$corresponds to the shape anisotropy ($\approx \frac{10^4 erg}{cm^3}$) which gives the in-plane demagnetizing field; and the strain-induced anisotropy K_σ (related to the magnetoelastic effect) which is determined by magnetostriction coefficient (λ_{lmn}) and in-plane strain ($\varepsilon_{\parallel}$). For EuIG and TbIG, K_σ is positive and large ($\approx \frac{10^5 erg}{cm^3}$) as can be seen in Table 2-1. As a result, comparing these three anisotropies, K_σ is at least one order of magnitude larger than K_c and $2\pi {M_s}^2$. Therefore, to evaluate how the compressive strain influences the magnetic anisotropy, we first determine the anisotropy field from the hard-axis AHE loops and quantitatively study *t*-dependence in EuIG/Pt(5 nm) and TbIG/Pt(5 nm). The EuIG films with *t* up to 56 nm show out-of-plane magnetization whereas those above 56 nm show in-plane magnetization, indicating that the PMA field is overcome by the

demagnetizing field above this thickness. On the other hand, TbIG shows perpendicular magnetization for all films with the thickness up to 100 nm. This is primarily due to a smaller saturation magnetization value in TbIG which causes the PMA field to be dominant over the demagnetizing field in the entire thickness range. Detailed transport measurements for the Hall resistivity (ρ_{AHE}) and longitudinal magnetoresistance (MR) (R_{xx}) responses are performed with *hard-axis field sweeps* to reach magnetic field saturation value (H_S^{ha}) in which both ρ_{AHE} and R_{xx} signals saturate, this term is equivalent to the absolute value of the demagnetizing field $4\pi M_{eff}$. Figure 2-5(c,d) show two examples of the $4\pi M_{eff}$ extraction procedure on EuIG (20 nm)/Pt (5 nm) and TbIG (60 nm)/Pt (5 nm) with perpendicular magnetization easy axis from the Hall and MR which have the same values. Dashed lines in Figure 2-5(c & d) define the demagnetizing field $4\pi M_{eff}$ for 20 nm thick EuIG with saturation of 14.50 kOe and for 60 nm thick TbIG with saturation of 17.50 kOe. From equation (2-3), the value of $H_{2\perp}$ is extracted from

$$H_{2\perp} = 4\pi M_s - 4\pi M_{eff} \quad (2\text{-}11).$$

For samples with PMA, $4\pi M_{eff}$ is obtained by sweeping the external magnetic field in the in-plane direction, and in this case, $4\pi M_{eff} < 0$. On the other hand, for samples where the magnetization is in-plane, the Hall voltage may contain a planar Hall component when an in-plane field is applied (Figure 2-7). In this case, $4\pi M_{eff} > 0$, and an out-of-plane saturation field is measured instead (Figure 2-7).

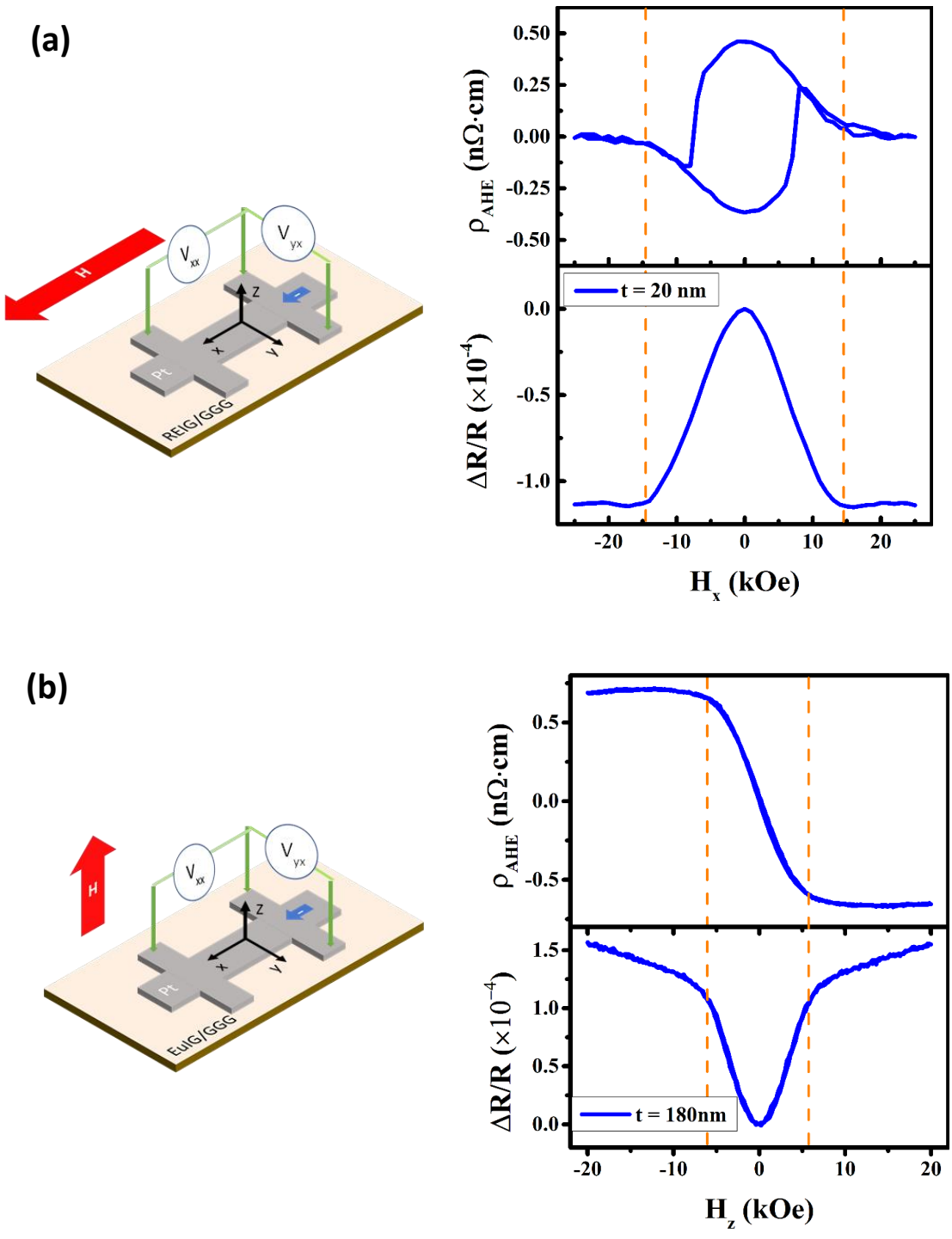

Figure 2-7 Transport measurement configuration for anisotropy field extraction. *Electrical transport measurement geometries used for the H_{sat} extraction for a) TbIG and EuIG t ≤ 56 nm, b) EuIG t> 56 nm.*

Figure 2-8 (a) and (b) show the plot $H_{2\perp}$ as a function of film thickness t; $H_{2\perp}$ follows a $1/(t+t_o)$ behavior (fitted as $H_{2\perp} = \left(\frac{691.05}{t+13.69} - 8.48\right)\ kOe$ for EuIG, $H_{2\perp} = \left(\frac{4472.76}{t+48.50} - 24.36\right)\ kOe$ for TbIG), as it has been observed in other works [21]. As described in equations (2-4) and (2-5), $H_{2\perp}$ has a linear relation with the in-plane strain $\varepsilon_{\parallel}$, and is expected to follow the same behavior as the out-of-plane strain, $\varepsilon_{\perp}$, according to equations (2-6) and (2-7). There are two regimes for the effect of lattice mismatch in thin films [22]: for film thickness t below certain critical value t_c, the film will be pseudomorphic and the strain is given by $\eta = \frac{a_f - a_s}{a_s}$, while for $t > t_c$, the strain relaxes as $\varepsilon_{\parallel} \propto \eta \frac{t_c}{t}$. The insets in Figure 2-8(a,b) show that for the measured thickness (t > 4 nm), the $1/(t+t_o)$ behavior is observed, indicating that the strain in the lattice relaxes over the entire thickness range. The fitted equation for the out-of-plane strain versus thickness is consistent with this $1/(t+t_o)$ behavior, with a residual value of 0.34% for EuIG and 0.01% for TbIG as $t \to \infty$. The relatively large residual strain in the thick EuIG film limit suggests that the PLD films differ somewhat from the bulk crystals. The difference may be caused by oxygen deficiency or other defects in PLD films, which may account for the relatively low saturation magnetization as mentioned earlier. Nevertheless, this slow relaxation of strain in garnets is quite striking, considering that metallic materials have their strain relaxed usually for thickness less than 10 nm; this slow strain relaxation in garnets allows us to tune the magnetic properties over a wide range.

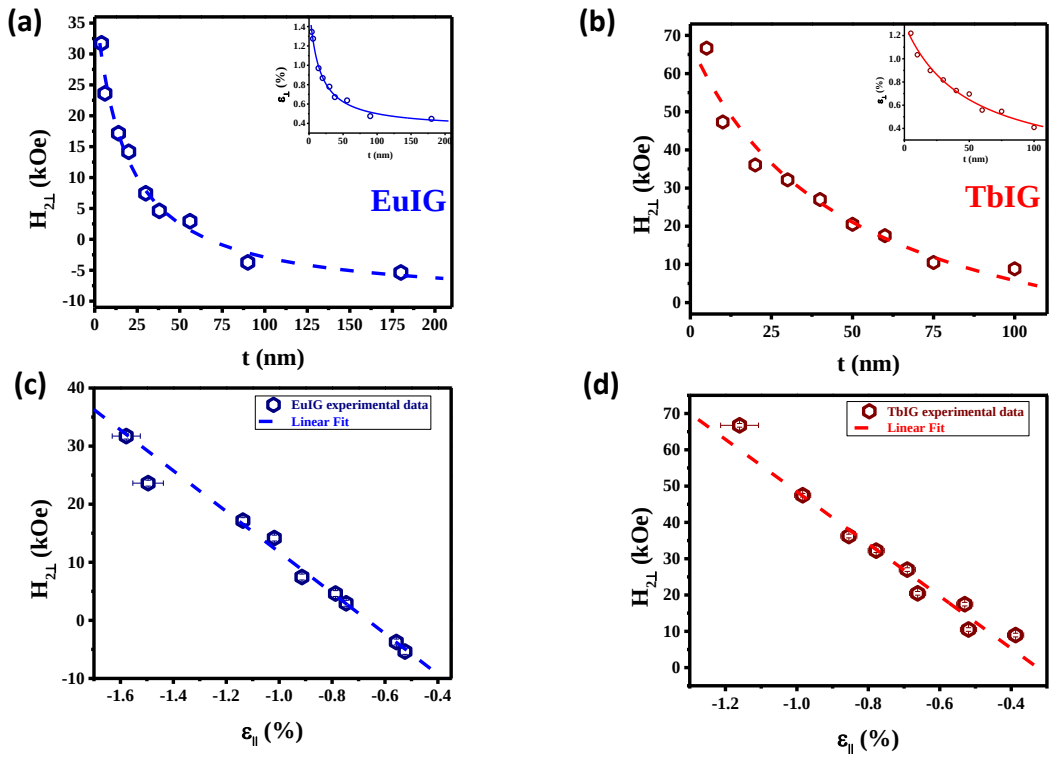

Figure 2-8 Magnetic anisotropy and in-plane strain in EuIG and TbIG thin films. *(a) and (b): $H_{2\perp}$ vs. t for (a) EuIG and (b) TbIG. In the inset the out-of-plane strain $\varepsilon_\perp$ as a function of film thickness, showing the corresponding $1/t+t_0$ behavior for the measured interval. (c) and (d): $H_{2\perp}$ as a function in-plane strain $\epsilon_\parallel$ for (a) EuIG and (b) TbIG. The dashed line is linear fit to obtain thin film magnetostriction constant (λ_{100}) for EuIG and (λ_{111}) for TbIG.*

Figure 2-8 (c,d) show $H_{2\perp}$ as a function of $\varepsilon_\parallel$ for both EuIG and TbIG respectively, where a linear relation was observed. A least square fitting was performed and the magnetostriction coefficient λ was calculated. For EuIG, it was found that $\lambda_{100EuIG} = (2.7 \pm 0.1)\times10^{-5}$, which is about 29% larger than the reported value ($\lambda_{100} = 2.1\times10^{-5}$), while for TbIG, it was found that $\lambda_{111TbIG} = (1.35 \pm 0.06)\times10^{-5}$, being only 12% larger than the literature value ($\lambda_{111} = 1.2\times10^{-5}$) [13], these variations may be attributed to the difference

in growth conditions of both bulk and thin film samples which result in slightly different material properties and additionally the difference in measurement techniques.

In summary, we have used compressive in-plane strain to control the perpendicular magnetic anisotropy in coherently strained epitaxial EuIG (001) and TbIG (111) thin films. We performed electrical measurements on Pt Hall bars fabricated on these films and they showed squared AHE hysteresis loops which are primarily sensitive to the net magnetic moments of Fe^{3+}. The PMA field relaxes slowly as the ferrimagnetic insulator thickness increases, which allows our experimental approach to demonstrate a full control of magnetic anisotropy of REIG ferrimagnetic insulators using epitaxial growth.

Chapter 3: Effects of Strain on the Dynamic Magnetic Properties of Europium Iron Garnet Thin Films

As it was briefly introduced in Section 1.4:, REIGs can be used as a source of spin waves by inducing excitations to the magnetization $\vec{M}$ of a specimen. Spin waves in REIGs can propagate for long distances as it has been demonstrated in previous experiments [23] [24]. One major advantage of REIGs over ferromagnetic metal thin films is that they show a smaller damping of the precession of $\vec{M}$ for a given excitation, allowing a more efficient transmission of spin wave signals on REIGs due to its lower dissipation, this attribute along with the ones mentioned in Section 1.5: make REIGs a suitable material for the development of low power, high density spintronic devices.

In order to study the magnetic dissipative properties of REIGs, the FMR technique has shown to be a powerful tool to determine the magnetic properties and the spin dynamics of ferromagnetic materials. To understand the FMR phenomenon, it is necessary to develop the energy equation of the magnetic free energy in a thin film, which in the general case in a spherical coordinate system can be written as:

$$F = -\vec{H} \cdot \vec{M} + F_{MA} \tag{3-1}$$

where the term $-\vec{H} \cdot \vec{M}$ corresponds to the Zeeman energy due to an external field $\vec{H}$ and F_{MA} the magnetic anisotropy energy. Usually the first order approximation for F_{MA} term is

more than enough to analyze the dynamics of the magnetization (equation 2-2), and then equation (3-1) takes the form

$$F = -\vec{H} \cdot \vec{M} + (2\pi M_s^2 - K_u)\, cos^2\, \theta \qquad (3\text{-}2)$$

However, it has been observed that for structural deformed systems higher order terms are necessary to describe more accurately the magnetic behavior of the specimen, therefore equation (3-1) has to be adjusted accordingly depending on the orientation of the magnetization in the sample.

Compared to other magnetic materials, an unparalleled attribute of REIGs is their rich magnetoelastic property, with the magnetostriction coefficient ranging from -8.5×10^6 to $+21\times10^6$ at room temperature, and up to two orders of magnitude increases at low temperatures. This property allows for tailoring desired magnetic anisotropy of the REIG thin films via growth, for example, by means of lattice mismatch, film thickness, oxide pressure, and chemical substitution. For magnetic thin films, the shape anisotropy usually dominates; therefore, the magnetization prefers to be in the film plane. The PMA can be introduced by utilizing the magneto-crystalline anisotropy or interfacial strain, both of which have been demonstrated through epitaxial growth [25] [12] [16] [26]. In TbIG and EuIG, it has been shown that the PMA field $H_{2\perp}$ can be as high as 7 T, much stronger than their bulk demagnetizing field. While using strain is an effective and convenient way of manipulating magnetic anisotropy, however, it comes at a cost of increasing the FMR linewidth ΔH [27]. The causes of this increase in the linewidth had remained unexplored.

In this work, we choose EuIG as the system to study the effect of strain on magnetic anisotropy and spin dynamics for the following reasons: (1) it has shown PMA under adequate strain for different substrate orientations and even in polycrystalline form [28]; it has shown PMA under moderate strain for different substrate orientations and even in polycrystalline form [28]; (2) the spin dynamics in EuIG bulk crystals is interesting, but has not been studied in the thin film form. Compared to other REIGs, the Eu^{3+} ions occupying the dodecahedral sites (c-site) have the J = 0 ground state, which should not contribute

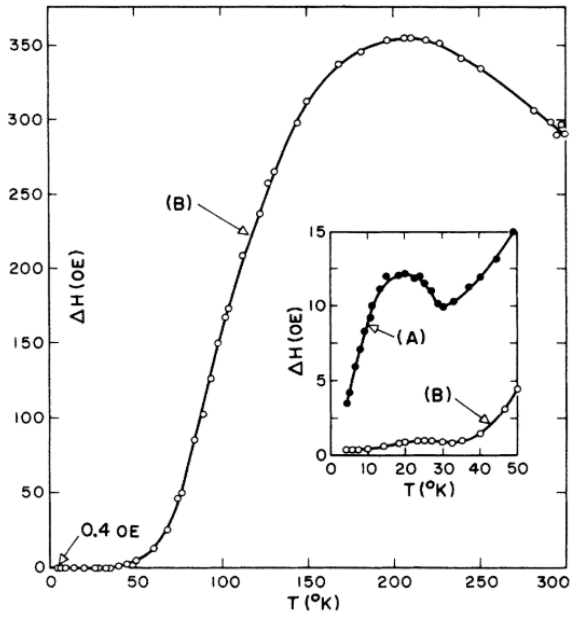

Figure 3-1: Temperature dependence of FMR linewidth in bulk EuIG. *The EuIG sample was a 1.4mm sphere, and the field direction was along the [111] axis. The inset shows the low temperature regime for samples grown under A) ordinary and B) highly purified lead oxide-boron fluxes. Adapted from Le Craw, R. et al. Phys. Rev. Lett.* ***11*** *11 (1963).*

to the total magnetic moment; therefore, EuIG may have narrow FMR linewidth just as YIG or LuIG [29]. In EuIG crystals, a narrow linewidth (< 1 Oe) [30] was observed at low

temperatures, but it showed a nearly two orders of magnitude increase at high temperatures (Figure 3-1), which raises very interesting physics questions regarding the fundamental damping mechanism.

EuIG films were grown by PLD from a target densified by powders synthesized using the method described in Section 2.2:. The films were deposited on (111)-oriented $Gd_3Sc_2Ga_3O_{12}$ (GSGG), $Nd_3Ga_5O_{12}$ (NGG), $Gd_{2.6}Ca_{0.4}Ga_{4.1}Mg_{0.25}Zr_{0.65}O_{12}$ (SGGG), $Gd_3Ga_5O_{12}$ (GGG), $Tb_3Ga_5O_{12}$ (TGG) and $Y_3Al_5O_{12}$ (YAG), these substrates were selected as they provide a wide range for lattice mismatch, with η ranging from +0.45% (GSGG) to -3.95% (YAG). The thin films were grown by PLD technique as described in Section 2.2:. RHEED was used to evaluate the crystalline structural properties of the EuIG films which after the *ex situ* RTA process all EuIG films reveal single crystal structure (Figure 3-2(a)). Atomic force microscopy was performed on all samples, where atomically flat and uniform films RMS roughness < 2 Å RMS) can be observed in all the grown films, with no surface defects visible. (Figure 3-2(b)).

To assess both purity and strain on the EuIG films, X-ray diffraction (XRD) was performed on all samples, using a PANalytical Empyrean diffractometer with Cu Kα radiation and a Ni filter, at room temperature in 0.002° steps in the 2θ range of 10°–90° (Figure 3-2(c)).

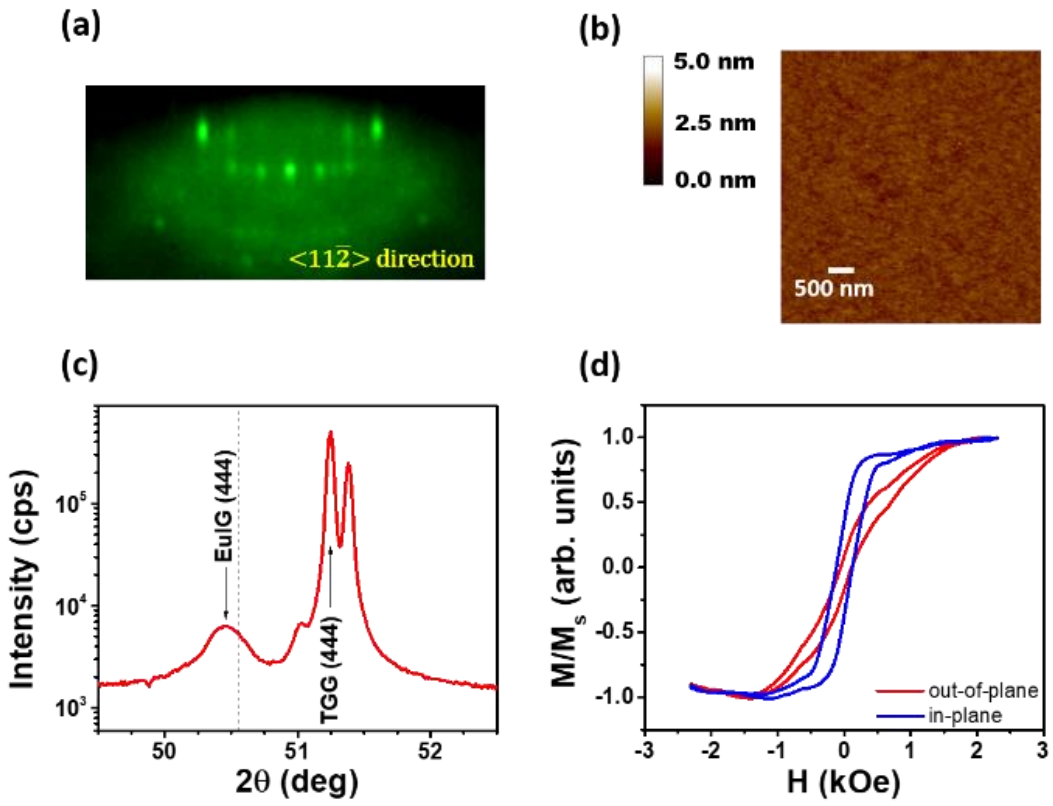

Figure 3-2 Structural, morphology and magnetic characterization of EuIG thin films*. EuIG 50 nm thin film grown on TGG(111). a) RHEED pattern along the* $\langle 11\bar{2} \rangle$ *direction, displaying single crystal structure after RTA process. b) 5 mm* $\times$ *5 mm AFM surface morphology scan, with an RMS roughness of 1.8 Å. c) Intensity semi-log plot of* θ *-* 2θ *XRD scan. The dashed line corresponds to the XRD peak for bulk EuIG. d) Magnetization hysteresis loops for external field in out-of-plane and in-plane directions.*

For all samples, one main peak for EuIG and the substrate is present, corresponding to the (444) Bragg peak, thus confirming the epitaxy and single crystal structure of the films. No secondary phases were observed. The Bragg peak corresponding to EuIG (a_o = 12.497 Å) is shifted with respect to the expected peak position of the bulk crystal, indicating a change in the lattice parameter perpendicular to the surface ($a_\perp$). In the example shown in Figure 3-2c, the peak position for EuIG (444) displays a shift to the left with respect to its bulk value, indicating an in-plane compressive strain in the EuIG lattice. To quantify the

in-plane biaxial strain $\varepsilon_{\parallel}$ of the EuIG films, we use the relationship to the elastic constants given in equations (2-7) and (2-8), with the parameters shown in Table 3-1 [17].

Substrate	a_s (Å)	η (%)	t (nm)	$\varepsilon_{\parallel}$ (%)	g	$H_{2\perp}$ (Oe)	$H_{4\perp}$ (Oe)	α ($\times 10^{-2}$)	ΔH_o (Oe)	Γ_o (Oe)
GSGG	12.554	0.45	20	0.10	1.40	-1394.2 ± 44.9	339.79 ± 6.59	2.46 ± 0.03	21.4 ± 1.7	6.05
NGG	12.508	0.06	50	0.06	1.38	-1224.4 ± 5.7	18.34 ± 0.05	2.41 ±0.01	8.9 ± 0.7	0.20
SGGG	12.480	-0.14	50	-0.09	1.40	-909.6 ± 15.2	164.8 ± 1.36	2.13 ± 0.01	5.6 ± 0.4	0.50
YSGG	12.426	-0.57	50	-0.06	1.37	-709.4 ± 22.0	377.3 ± 5.09	2.47 ± 0.03	9.9 ± 1.8	2.47
GGG	12.383	-0.92	50	-0.13	1.38	-1015.0 ± 81.3	887.2 ± 37.27	2.20 ± 0.14	412.2 ± 8.4	3.35
TGG	12.355	-1.14	50	-0.11	1.38	-393.4 ± 53.6	245.0 ± 10.00	2.29 ± 0.20	253.4 ± 11.8	0.20
YAG	12.004	-3.95	20	-0.12	1.37	-36.8 ± 47.1	424.8 ± 20.91	1.86 ± 0.20	217.0 ± 22.6	0.20

Table 3-1 Structural and magnetic parameters for the EuIG thin films grown on different substrates.

One important fact that we have to consider when engineering the magnetic anisotropy of rare earth iron garnets using film thickness as a knob is that this is proportional to $\eta/(t+t_o)$ [22]. Indeed, our lattice parameter calculations show that for small lattice mismatch (as in the case of EuIG/NGG) the strain in the EuIG is mostly preserved for a 50 nm thick film (pseudomorphic regime), whereas for larger η the lattice parameter of EuIG shows complete relaxation almost back to the bulk value parameters. For this reason, in the samples with larger η (YAG = -3.95 %, GSGG = 0.45%) we grew thinner EuIG films (20 nm) in order to have a larger in-plane strain (compressive for YAG, tensile for GSGG). For

the cases of EuIG grown on TGG and GGG substrates, the paramagnetic background of the substrates is too large to obtain a reliable measurement of the magnetic properties of the EuIG films, therefore the study of thinner films on these two substrates was discarded.

Room temperature magnetic hysteresis curves M vs. H for TGG/EuIG sample are shown in Figure 3-2(d) with the magnetic field applied parallel and perpendicular to the films. The saturation field for the out-of-plane loop (~1500 Oe) is clearly larger than that of the in-plane loop, indicating that the magnetization prefers to lie in the film plane, if we consider that for our EuIG films $M_s \approx 920$ Oe, then in this example the film does not show PMA. As shown in this example, from these curves, we can qualitatively track the evolution of the magnetic anisotropy in samples with different strain, however in some cases this approach can proof to be challenging because of the additional anisotropy contributions that can arise.

To quantitatively determine magnetic anisotropy, we first performed polar angle dependent FMR measurements using a X-band microwave cavity with f = 9.32 GHz under the geometry show in Figure 3-3(a), the samples were rotated from 0° to 180° in 10° steps, being 90° the sample orientation parallel to the applied field (i.e. static field in the in-plane direction). The spectra for all samples show a well-defined single resonance peak which can be described by a Lorentzian derivative. Despite different strains in all samples, the resonance field H_{res} is lower for the in-plane direction ($\theta_H = 90°$) than for the out-of-

plane direction ($\theta_H = 0°$). A quick inspection reveals that the out-of-plane (apparent hard-axis) resonant field H_{res} shifts to larger values as the lattice mismatch becomes larger and positive, corresponding to a weaker easy-plane anisotropy. The H_{res} shifts to smaller values for samples which lattice mismatch turns more negative (Figure 3-3(b)), corresponding to a stronger easy-plane anisotropy. Furthermore, the H_{res} values for all samples spread over a large range at $\theta_H = 0°$, indicating a significant effect of the strain on magnetic anisotropy. Figure 3-3(c) shows a comparison of FMR spectra between two representative samples at four selected polar angles: NGG/EuIG (small $\varepsilon_{\parallel}$) and YAG/EuIG (large $\varepsilon_{\parallel}$).

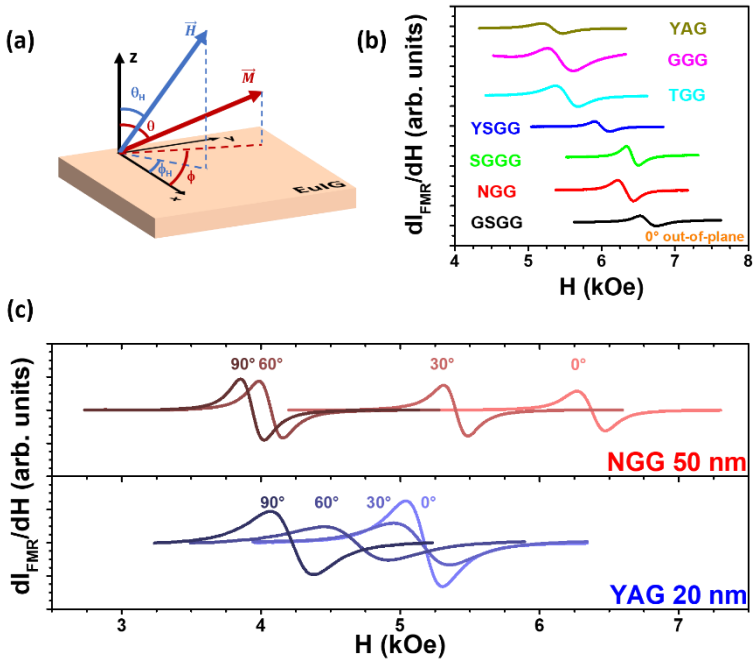

Figure 3-3 Polar angular dependent FMR. *a) Coordinate system used for the FMR measurement. b) Room temperature FMR derivative absorption spectra for $\theta_H = 0°$ (out-of-plane configuration) for EuIG on different (111) substrates. c) FMR derivative absorption spectra for 50 nm EuIG on NGG(111) ($\epsilon_{\parallel} \approx 0$) and 20 nm EuIG*

on YAG(111) ($\epsilon_{\parallel} < 0$) with polar angle θ_H ranging from 0° (out-of-plane) to 90° (in-plane) at room temperature.

To perform the corresponding fitting from the data obtained, we write the magnetic free energy density F equation that can be approximated by the sum of the Zeeman energy and the first (K_u) and second order (K_2) anisotropy terms:

$$F = -\vec{H} \cdot \vec{M} + (2\pi M_s^2 - K_u)\cos^2\theta - \tfrac{1}{2}K_2\cos^4\theta \qquad (3\text{-}3)$$

with H being the external magnetic field and M_s the magnetization of the sample. The equilibrium polar angle for the magnetization is obtained from $\frac{\partial F}{\partial \theta} = 0$, and using Smit Beljers formalism we write

$$\omega = \frac{\gamma}{M_s \sin\theta_H}\sqrt{\frac{\partial^2 F}{\partial \theta_H^2}\frac{\partial^2 F}{\partial \varphi_H^2} - \left(\frac{\partial^2 F}{\partial \theta_H \partial \varphi_H}\right)^2} \qquad (3\text{-}4)$$

being $\omega = 2\pi f$ the frequency of the electromagnetic wave driving the magnetization vector and θ_H, ϕ_H the polar and azimuthal angles of the applied magnetic field with respect to the axis normal to the film plane correspondingly. From equation (3-4) the gyromagnetic ratio $\gamma = \frac{g\mu_B}{\hbar}$, and the anisotropy related parameters can be calculated from the corresponding fitting. As including the whole set of anisotropy parameters in the fitting can lead to an overly complicated process, we qualitatively studied the in-plane azimuthal angular dependence FMR on all the samples, here we found an in-plane uniaxial with a six-fold contribution which effect on H_{res} was deemed very small to be considered (~ 15

Oe) (Figure 3-4); for this reason, we disregarded the in-plane anisotropy contributions in the fitting model.

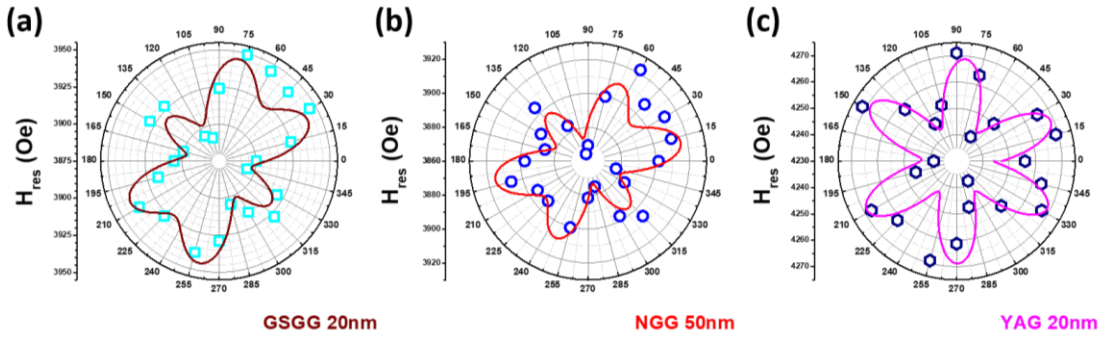

Figure 3-4 In-plane azimuthal angle dependent FMR on strained EuIG. *In-plane azimuthal angle dependent FMR of resonance field H_{res} for a) tensile in-plane strain ($\epsilon_{\parallel} > 0$) b) in-plane strain close to zero ($\epsilon_{\parallel} \approx 0$) c) compressive in-plane strain ($\epsilon_{\parallel} < 0$). Solid curves represent cosine approximation just as reference, to quantify the change in H_{res} as f is rotated; it clearly shows a uniaxial and a six-fold component. As the difference between the central value and the extrema is around 15 Oe, then its contribution can be neglected in the fitting model.*

From the polar angle dependent FMR, we plot the resonance field H_{res} as a function of θ_H (Figure 3-5(a,c)). From these set of plots, it can be observed that the required field to saturate the sample increases as the in-plane strain $\varepsilon_{\parallel}$ becomes more positive (i.e., the in-plane lattice parameter of the film is expanding). Once established the model to be fitted, we extracted the parameters $4\pi M_{eff} = 4\pi M_s - \frac{2K_u}{M_s}$ and $H_{4\perp} = \frac{2K_2}{M_s}$ from the corresponding fitting, from these we can plot both anisotropy related terms as a function of in-plane strain $\varepsilon_{\parallel}$, as shown in Figure 3-5(d,e). From this graph, we can clearly observe that $4\pi M_{eff}$ increases as the in-plane lattice parameter of the EuIG film becomes larger, as expected given the (111) orientation of our films and that the positive

magnetostriction constant for EuIG ($\lambda_{111} = +1.8 \times 10^6$), a straight line representing the magnetoelastic model described in equation (2-5) is traced showing that the data corresponding to the lower strain is in good agreement to this model, the more strained

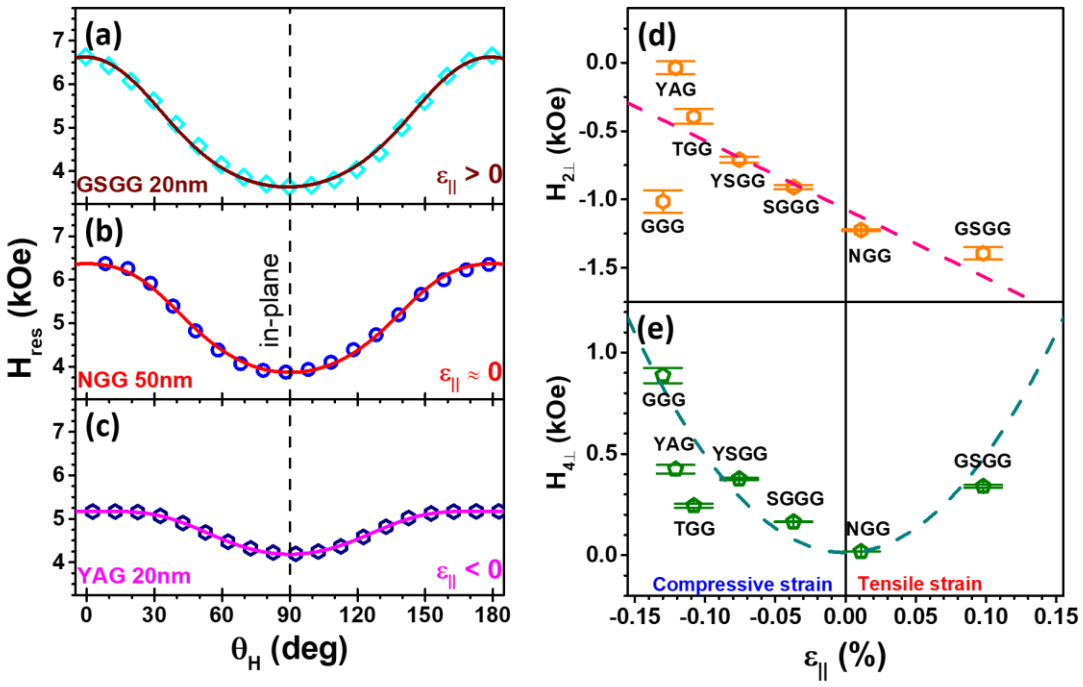

Figure 3-5 Polar angle dependent FMR on strained EuIG*. Polar angular dependent FMR of resonance field H_{res} for a) tensile in-plane strain ($\epsilon_{\parallel} > 0$) b) in-plane strain close to zero ($\epsilon_{\parallel} \approx 0$) c) compressive in-plane strain ($\epsilon_{\parallel} < 0$). Solid curves represent the best fitting. d) In-plane strain dependence of the anisotropy fields $H_{2\perp}$ and e)$H_{4\perp}$ obtained from fitting. The straight line in d) describes the dependence of $H_{2\perp}$ according to the magnetoelastic effect model, with $\lambda_{111} = 1.8 \times 10^{-6}$.*

data deviation may be due to difference in $4\pi M_s$ (920 Oe) due to possible oxygen deficiencies product of the higher strain levels. However, the term $4\pi M_{eff}$ cannot account for the whole out-of-plane contribution for the anisotropy field, the parameter $H_{4\perp}$ appears as the strain becomes larger in the field. For the case of small strain

(EuIG/NGG), the $H_{4\perp}$ term is small, whereas for larger in-plane strains (be it positive or negative) favors an abrupt increase in $H_{4\perp}$, this is a clear indication that the higher order contributions to the anisotropy in EuIG films make themselves present only when a crystal deformation takes place; indeed if we consider the magnetoelastic model and expand to higher order terms, we can find that strain will have a $cos^4\theta$ that will provide a contribution to $H_{4\perp}$ according to the magnetic energy equation (3-3); this is supported by the quadratic behavior observed in $H_{4\perp}$ as indicated by the parabola traced in Figure 3-5. Moreover, if we consider the values for $4\pi M_s$ = 920 Oe for our EuIG films [25], then from the calculated parameters for $4\pi M_{eff}$ the first order anisotropy term K_u is positive for all thicknesses, as well as the second order anisotropy term K_2, thus revealing that the magnetization lays in an easy plane. For the samples grown on YAG and TGG, the K_u term is very close to zero, approaching a coexistence region where both perpendicular and in-plane orientations present a minimum in the magnetic free energy region [31].

As the polar angle dependent FMR revealed different broadening levels of the linewidth for the different samples, we performed broad-band frequency dependent FMR up to 15 GHz using a coplanar waveguide (CPW) with field modulation, from this measurement we first plot microwave frequency f as a function of the resonant field H_{res}, where we can obtain from Kittel equation

$$f = \frac{|\gamma|}{2\pi}\sqrt{H_{res}\left(H_{res} + 4\pi M_{eff}\right)} \qquad (3\text{-}5)$$

the parameters γ and $4\pi M_{eff}$, these values match within the uncertainty level to the ones obtained by the polar angular dependent FMR. We proceeded then to plot the half width, half maximum (HWHM) ΔH of each spectrum and plotted this parameter as a function of the microwave frequency f (Figure 3-6(a)). This data can be fitted by [32]

$$\Delta H = \Delta H_{Gilbert} + \Delta H_{TMS} + \Delta H_o \tag{3-6}$$

where $\Delta H_{Gilbert}$ corresponds to the intrinsic damping of the system according to the Landau-Lifshitz-Gilbert equation, and it is given by

$$\Delta H_{Gilbert} = \frac{2\pi\alpha f}{|\gamma|} \tag{3-7}$$

being α the Gilbert damping parameter; ΔH_{TMS} corresponds to the two-magnon scattering contributions and it is expressed by

$$\Delta H_{TMS} = \Gamma_o \arcsin \sqrt{\frac{\sqrt{f^2+\left(\frac{f_o}{2}\right)^2}-\frac{f_o}{2}}{\sqrt{f^2+\left(\frac{f_o}{2}\right)^2}+\frac{f_o}{2}}} \tag{3-8}$$

where Γ_o denotes the magnitude of the two-magnon scattering, $f_o = 2\gamma M_{eff}$; and ΔH_0 is the inhomogeneous linewidth.

From Figure 3-6(a), the *ΔH vs. f* plot reveals that the dependence for all the probed frequencies is mostly linear, this is an indication of a small two-magnon scattering contribution. We can also distinguish two sets of behaviors: one with small inhomogeneous linewidth ΔH_0 (~10 Oe) corresponding to the samples with relatively low

strain ($|\varepsilon_{\parallel}| < 0.10\%$), while the ones with larger strain show a dramatic increase on the value of ΔH_0 (Figure 3-6(b)). We attribute this effect to the increase of crystal defects caused by the increased rate of strain relaxation due to a larger lattice mismatch, causing

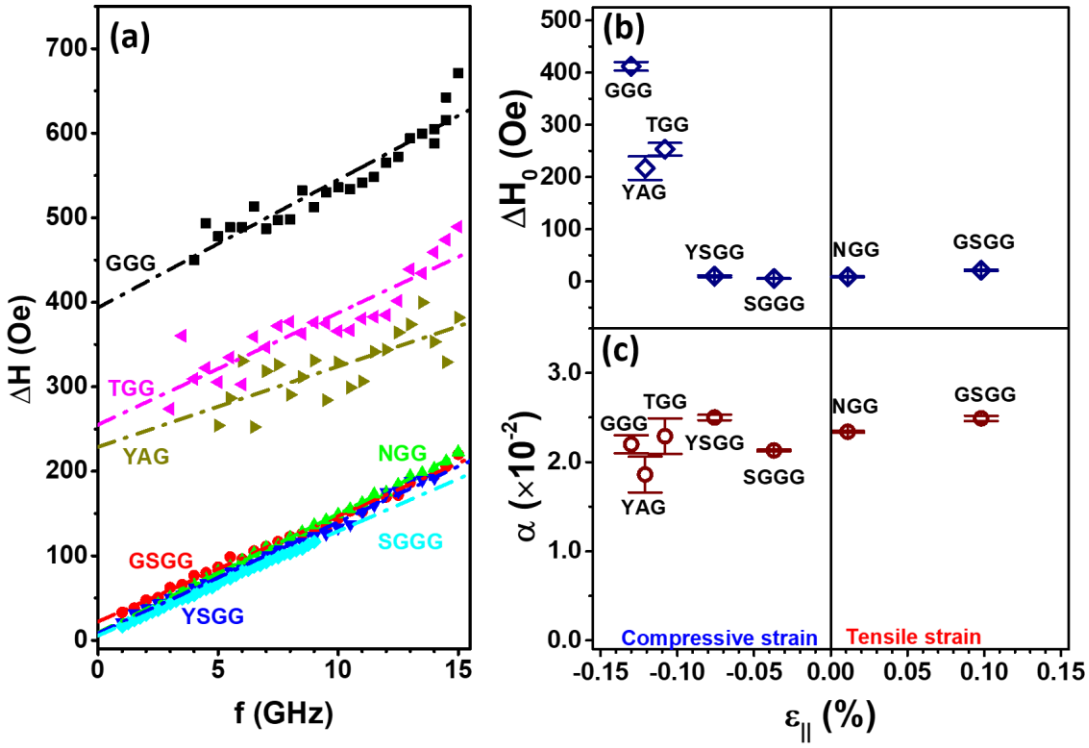

Figure 3-6 Frequency dependent FMR on strained EuIG thin films. *Frequency dependent FMR with applied in-plane static field. (a) HWHM linewidth vs. frequency for EuIG films grown on different substrates, with the corresponding fitting according to Equation (3-6). In-plane strain dependence of the dynamic magnetic parameters (b) ΔH_0 and (c) α extracted from the fitting.*

a larger disorder in the stress distribution and thus an increased distribution per unit volume of magnetic imperfections [33]. The effect is notorious for the compressive tensile

strain, yet it is not observable for the tensile strain case, this might be due to the smaller lattice mismatch for the tensile strain case (|ε| = 0.45% for GSGG substrate) compared with the larger mismatch for the compressive strain case (|ε| > 0.90%). Unfortunately, the lack of garnet substrates that could provide a larger tensile strain limits our capability to verify this assumption. The fitted parameters shows that the effect of strain on the values for the Gilbert damping α is negligible, this result reflects that the Gilbert damping α is an intrinsic property of the material and that the increase in the linewidth observed in FMR experiments in thin films is due to the enlargement of the inhomogeneous linewidth ΔH_o instead. The fitted parameters can be found in Table 3-1.

In summary, we have used lattice mismatch-induced strain on PLD-grown EuIG(111) thin films to study its effect on their magnetic properties. We verified that the demagnetizing field $4\pi M_{eff}$ can be tuned by magnetostriction over a wide range of in-plane strain, and that a second order anisotropy field term $H_{4\perp}$ becomes larger as the in-plane strain increases. More importantly, we found that the increase in the linewidth observed for EuIG thin films in FMR experiments is due to an increase in the inhomogeneous linewidth ΔH_o while the Gilbert damping a remains mostly unaffected, this information can prove to be useful in the design of devices for spintronic applications.

Chapter 4: Rare Earth Iron Garnets as Pure Spin Current Sources

Section 4.1: Spin Seebeck Effect

The phenomenon known as Spin Seebeck Effect (SSE) refers to the generation spin accumulation (that can be visualized as the difference in spin up/spin down chemical potentials) due to a temperature gradient in a magnetic material [34], such spin accumulation will generate a spin current in an similar way on how a charge current is generated by a potential differential across a conducting medium, as it can be observed in Figure 4-1. In the case of metallic magnetic materials, the SSE is always accompanied by the *anomalous Nernst effect* (ANE), which is the generation of an electric field in a magnetic material under a thermal gradient, and as such ANE usually obscures the contribution of SSE in metallic systems [35]. As mentioned previously in Section 1.3:, in

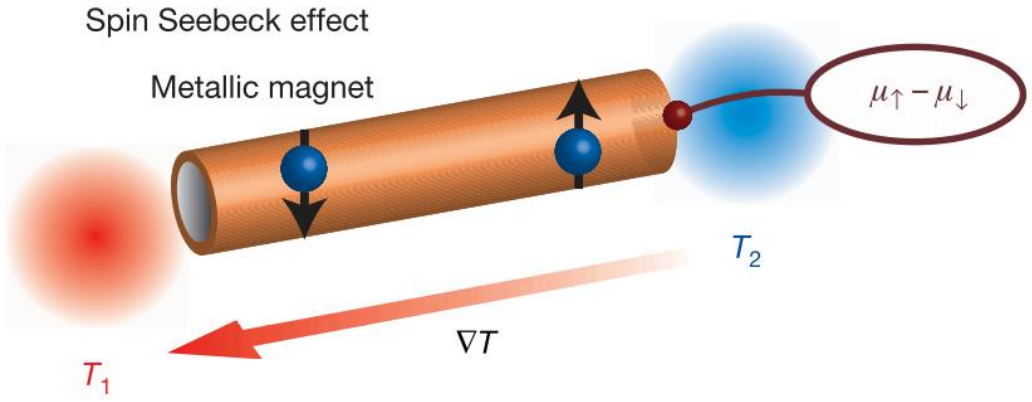

Figure 4-1 Spin Seebeck Effect. *Depiction of the spin Seebeck effect due to a differential in spin chemical potential $\mu_\uparrow - \mu_\downarrow$ caused by a thermal gradient ∇T along a metallic magnet. Adapted from Uchida, K. et al. Nature **455** 7214 (2008).*

the case of insulating materials, a pure spin current will be generated when a thermal gradient, therefore the ANE contribution can be completely suppressed in the ferromagnetic insulator.

There are two common experimental setups to observe SSE: the first consists on applying the thermal gradient ∇T on the same plane of the sample to study, thus generating a spin current j_s that is normal to the plane (i.e. $j_s \perp \nabla T$), this configuration is known as transversal spin Seebeck effect (TSSE); in the second setup ∇T is applied perpendicular to the sample plane, hence $j_s \parallel \nabla T$, this configuration is referred as longitudinal spin Seebeck effect (LSSE) [36].

As ferromagnetic insulators do not generate a voltage by themselves, one method to detect the SSE in these materials is by the use of ISHE (Section 1.3:), the most common way is by creating a layer of a material with large SOC (such as Pt, W, Ta, Sb_2Te_3, etc.) in contact to the ferromagnetic insulator, in this way the spin current will be injected into this adjacent layer and converted in a charge current that can be readily measured by electrical means. This measurement configuration can be observed in Figure 4-2.

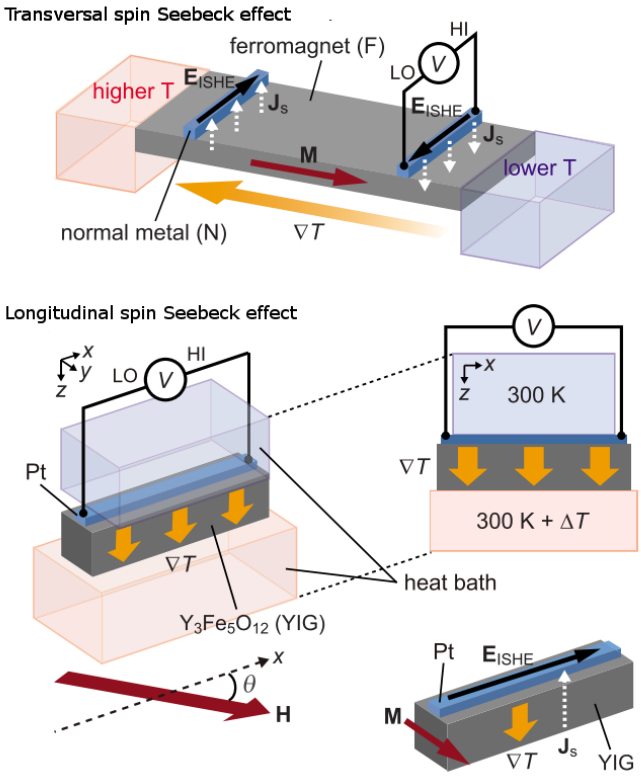

Figure 4-2 Spin Seebeck effect configurations. *Measurement set ups for transversal and longitudinal spin Seebeck effect. Adapted from Uchida, K. et al. Appl. Phys. Lett. 97 172505 (2010).*

Section 4.2: Spin pumping

Spin pumping refers to a series of techniques on which a spin wave generated in a magnetic layer transmits part of its angular momentum into an adjacent non-magnetic layer [37], translating into a spin accumulation. If this layer is a material with high SOC then this accumulation of spins can be measured by ISHE as described in Section 1.3:. In order to generate a spin wave in a magnetic layer, the most recurred way is by excitation

of the ferromagnetic material with microwave [38], driving the magnetization into precession by ferromagnetic resonance (Figure 4-3).

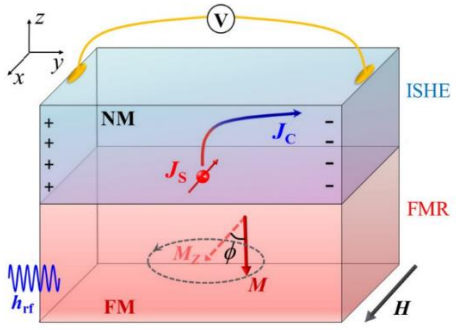

Figure 4-3 Spin pumping experiment configuration. *FMR driven spin pumping experiment, where the ferromagnetic layer (FM) generates a spin current in the normal metal (NM), which in turn can be measured by ISHE. Adapted from Yang, F. and Hammel, C. J. Phys. D **51** 253001 (2018).*

Section 4.3: Examples of rare earth iron garnet as sources of pure spin currents

4.3.1 Effect of electrostatic gating on topological spin Seebeck effect

Topological insulators (TI) are a family of materials with high SOC with bulk band gap and gapless surface states, this attribute has been revealed experimentally by angle-resolved photoemission spectroscopy (ARPES), where a Dirac cone from the surface states is observed (Figure 4-4) [39] [40]. The large SOC in Tis grants the electrons in their surface a spin-momentum character, this means that when a spin imbalance is present in the surface states of the TI, a charge current perpendicular to the spin polarization and to the vector normal to the surface will be generated. For this reason, if a TI layer forms part of

a magnetic heterostructure, the two-dimensional character of the surface states of TI would not allow spin diffusion into its bulk, with all the spin-charge conversion happening

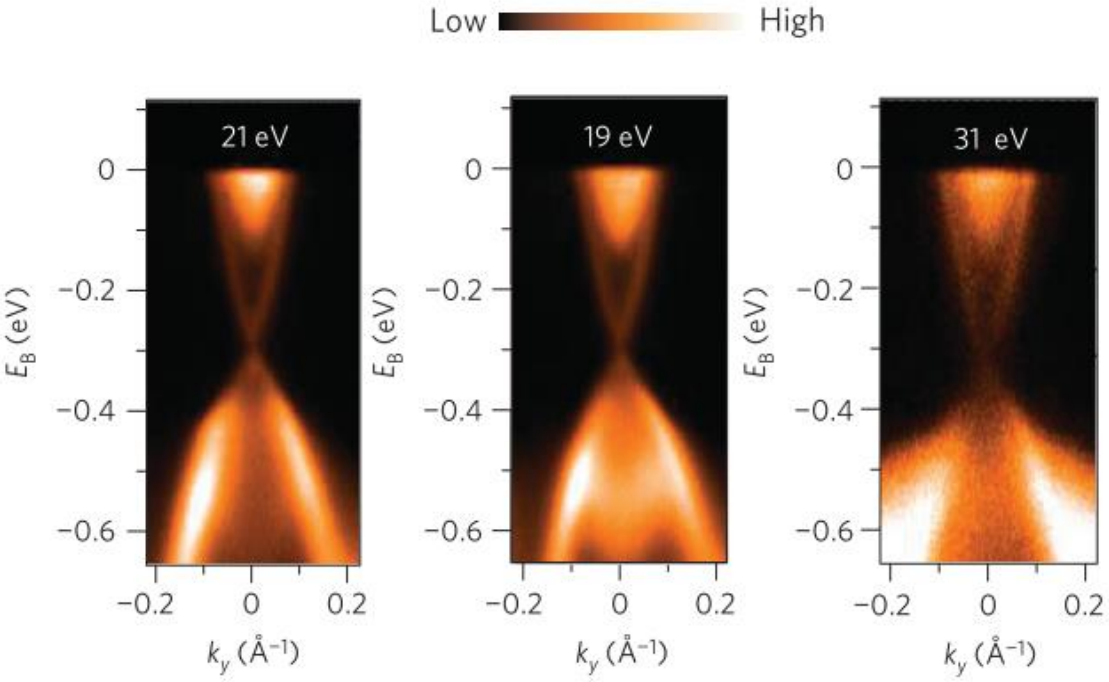

Figure 4-4 Observation of the Dirac cone by ARPES experiment. *Energy dispersion data obtained from ARPES experiment, along the $\overline{\Gamma} - \overline{M}$ cut, showing the Dirac-like bands, the Dirac point appears inside the bulk band gap. Adapted from Xia, Y. et al. Nat. Phys.* ***5*** *6 (2009).*

at the interface, this attribute grants TIs a greater spin-charge conversion efficiency compared with heavy metals [41] [42] [43]. However, for this effect to happen, it is a necessary condition to have the Fermi level in the bulk band gap inside the topological surface state, this has been successfully demonstrated by doping into the TI structure, showing an enhancement of the LSSE signal in a YIG/$(Bi_xSb_{1-x})_2Te_3$ (YIG/BST) heterostructure when the doping brought the TI close to the Dirac point (Figure 4-5) [44].

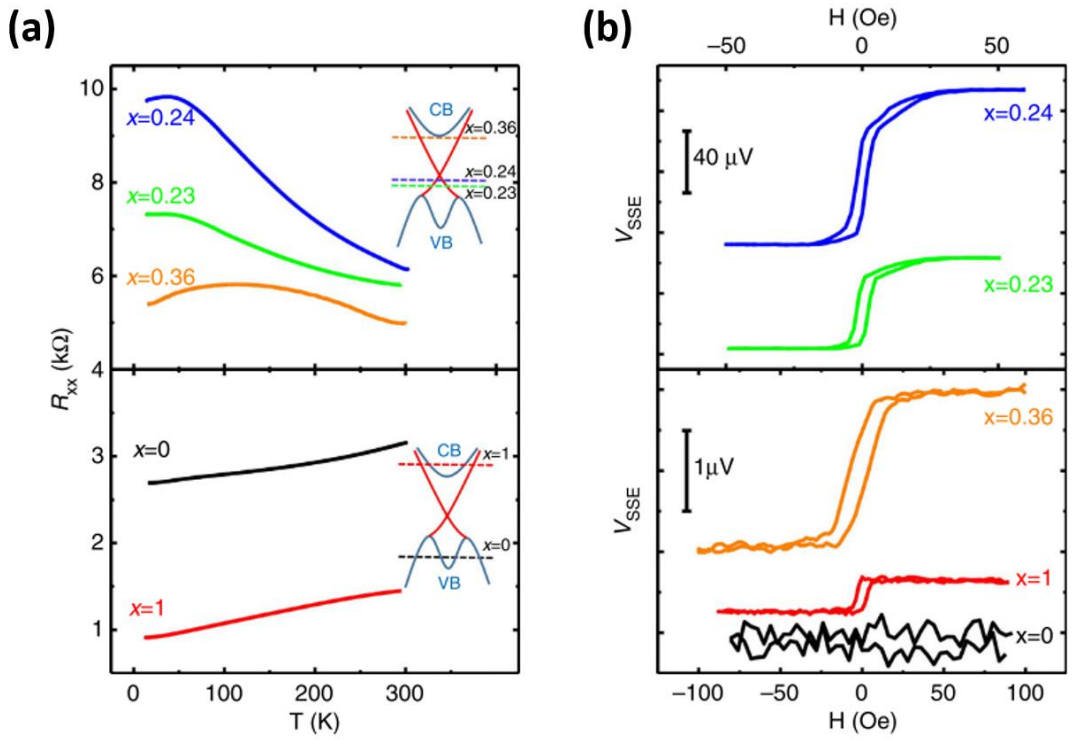

Figure 4-5 Topological LSSE in YIG/TI heterostructures*. a) Temperature dependence of longitudinal resistance for 5 QL $(Bi_xSb_{1-x})_2Te_3$ TI on YIG heterostructures, the inset shows the position of the Fermi level in the electronic band structure for different levels of doping. b) Field dependence of the LSSE ISHE voltage for different TI doping levels. Adapted from Jiang, Z.L. et al. Nat. Comm.* ***7*** *11458 (2016).*

One interesting question that arises is the behavior of the SSE when the Fermi level is exactly tuned in the Dirac point. According to the proposed theoretical model, in the Dirac point there should be no surface carriers available, and therefore the SSE signal should become zero. However, tuning the Fermi level by doping has the caveat of the inability of continuously adjust the chemical potential precisely into the Dirac point, so this impediment might be cleared by the use of electrostatic gating.

The first approach for electrostatic gating we performed was by the use of the same structure that was used by Jiang et al. [45] for their AHE experiments, which is similar to the device structure we used for the LSSE experiment described in Subsection 0. We grew 20 nm YIG on GGG(111) by PLD technique using the process described before in Section 2.2:, after the RTA process the YIG film shows single crystal ordering and the AFM measurement reveals flat and uniform surface with RMS roughness < 2 Å RMS, then we grew as our TI 5 quintuple layers (QL) of $(Bi_xSb_{1-x})_2Te_3$ by molecular beam epitaxy (MBE) process, capped by a 5nm Te layer The TI reveals the typical streaky pattern corresponding to high crystallinity and uniformity (Figure 4-6). For the device fabrication process, we patterned a Hall bar using photolithography and then etched the TI

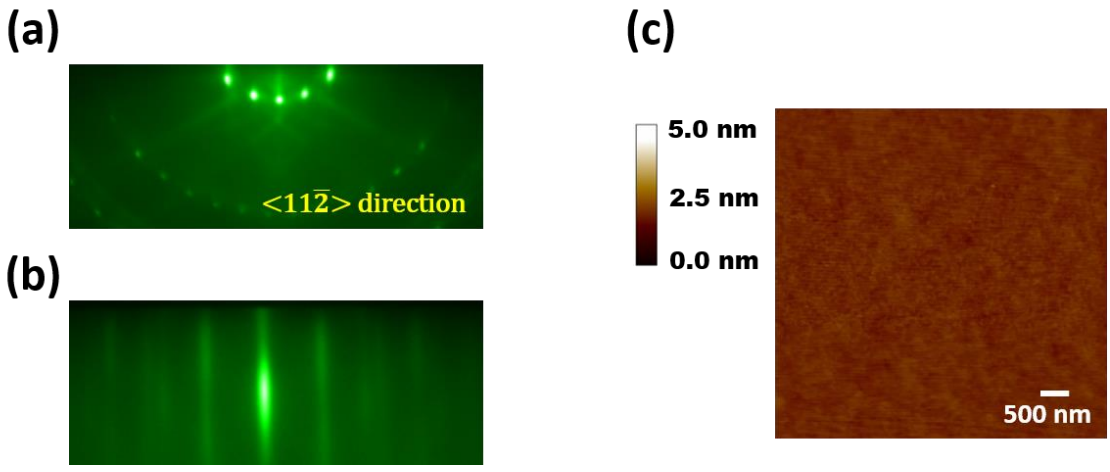

Figure 4-6 Structural and morphology characterization of YIG and YIG/TI film on GGG(111)*. a) RHEED pattern along the $\langle 11\bar{2} \rangle$ direction of YIG, displaying single crystal structure after RTA process. b) RHEED pattern after 5 QL of BST x = 0.3. c) 5 mm × 5 mm AFM surface morphology scan of YIG before TI growth, with an RMS roughness of 1.3 Å.*

on the surface by Ar ion bombardment, after that we fabricated the electrical contacts by depositing 5 nm Ti/45 nm Au in the corresponding region, then we covered the whole structure by a 100 nm layer of HfO_2, and finally we patterned a heater channel vertically aligned to the TI Hall channel, and then deposited 40 nm Ti/10 nm Au as a heater (Figure 4-7). In our approach we replaced the Al_2O_3 layer the previous work used as insulation between the heater and the TI for HfO_2 because the higher dielectric constant of HfO_2 ($\kappa = 25$) would provide a more effective gating capability compared to Al_2O_3 ($\kappa = 9$) [46], enabling a larger response to an applied electric field on the sample to be studied. The reduction of the thickness of the dielectric would also be a contributing factor in the increase of the effectiveness of this top gating approach.

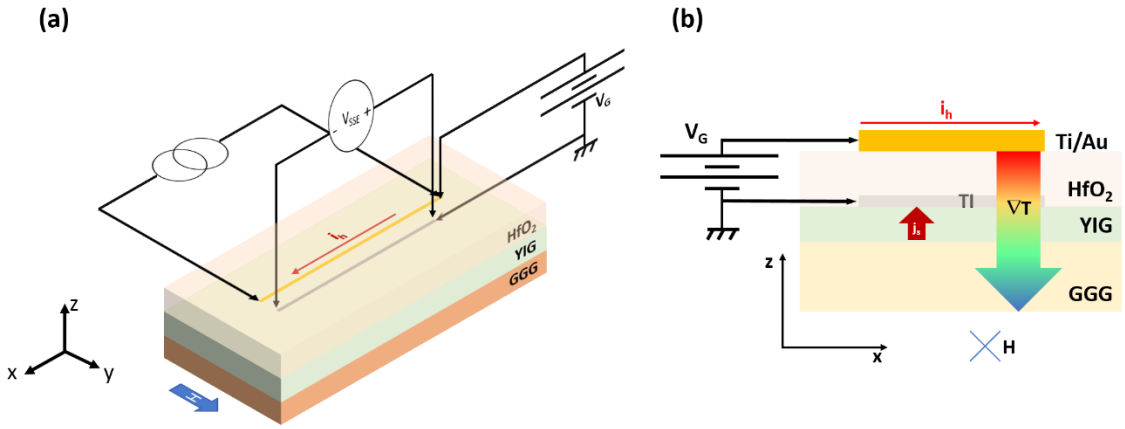

Figure 4-7 Schematic for top-gated LSSE experiment. *a) Electrical connections for the LSSE top gated experiment. A 100 nm thick HfO_2 layer acts as insulating layer between the gate/heater and the TI. b) A current source injects i_h into the gate/heater to produce a temperature gradient through the heterostructure, while a voltage source connected between the TI sample and the gate/heater electrode provides the electric field generated by V_G to tune the Fermi level in the sample.*

We conducted the first experiment on a heterostructure with x = 0.3 (which will be referred from now on as sample A) as substitution in the BST, with a fixed heater current which provided P = 173 mW and a system temperature of 20 K, this temperature was selected to obtain the maximum gating effect on our dielectric. We measured first the longitudinal resistance response of the TI to the applied gate voltage. We can see from Figure 4-8(b) that the sheet resistance of the TI sample increases as the gate voltage becomes more positive, then reaches a maximum at $V_G \approx 20V$, and then slowly decreases

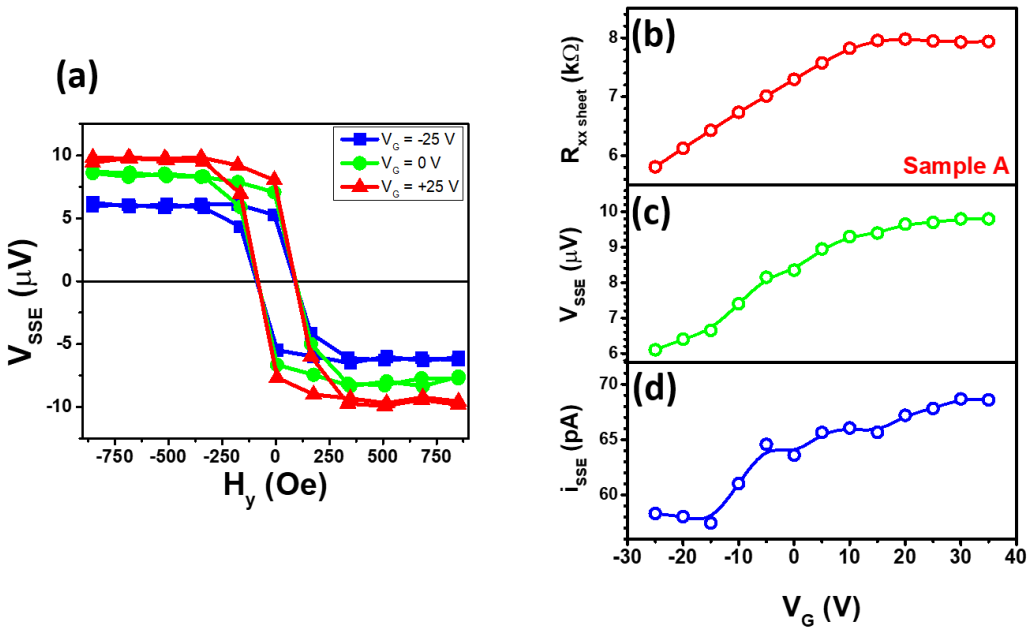

Figure 4-8 Top gate effect on longitudinal spin Seebeck effect of TI*. a) Field dependence of the LSSE voltage of a YIG/BST (x = 0.3) heterostructure (sample A) for different top gate voltages, showing an increase on the SSE signal as the gate becomes more positive. b) Sheet resistance, c) SSE voltage and d) SSE induced charge current i_{SSE} dependence to top gate voltage, showing all similar trend.*

about 1% of its maximum value for the remaining gate sweep. This behavior suggests that the Fermi level approaches the Dirac point from the valence band. After the gating effect on resistivity experiment, we swept the magnetic field in the y-axis direction where the in-plane hysteresis loop of YIG is expected[1], changing the V_G in steps of 5 V. Figure 4-8(a) shows clearly that the LSSE signal is modified by the change of gate voltage, becoming larger as the gate becomes more positive. The general trend of V_{SSE} and the charge current induced by magnon decay i_{SSE} can be observed in Figure 4-8(c,d), where it is evident that both follow the increase in the sheet resistance R_{xx}. From these results, we can see that the i_{SSE} increases 18.96% in the interval the top gate is swept.

We repeated the experiments for two other samples, a second one with x = 0.3 (sample B) and another with x = 0.225 (sample C), we performed the experiments at T = 20 K and P = 173 mW. The corresponding data can be visualized in Figure 4-9.

From sample B, we can observe that even though it has the same nominal substitution as sample A (x = 0.3), the behavior that it presents under the same measurements conditions differs one to the other, for instance, Figure 4-9(a) shows that sample B reaches the maximum resistivity value at $V_G \approx$ -15V, in contrast to sample A where the maximum happens at $V_G \approx$ +20V. The resistivity after the peak in sample B shows an 8% decay of its

[1] Under the connection configuration of our system, a positive thermal gradient (i.e, from top to bottom) will generate a positive V_{SSE} for negative H and vice versa.

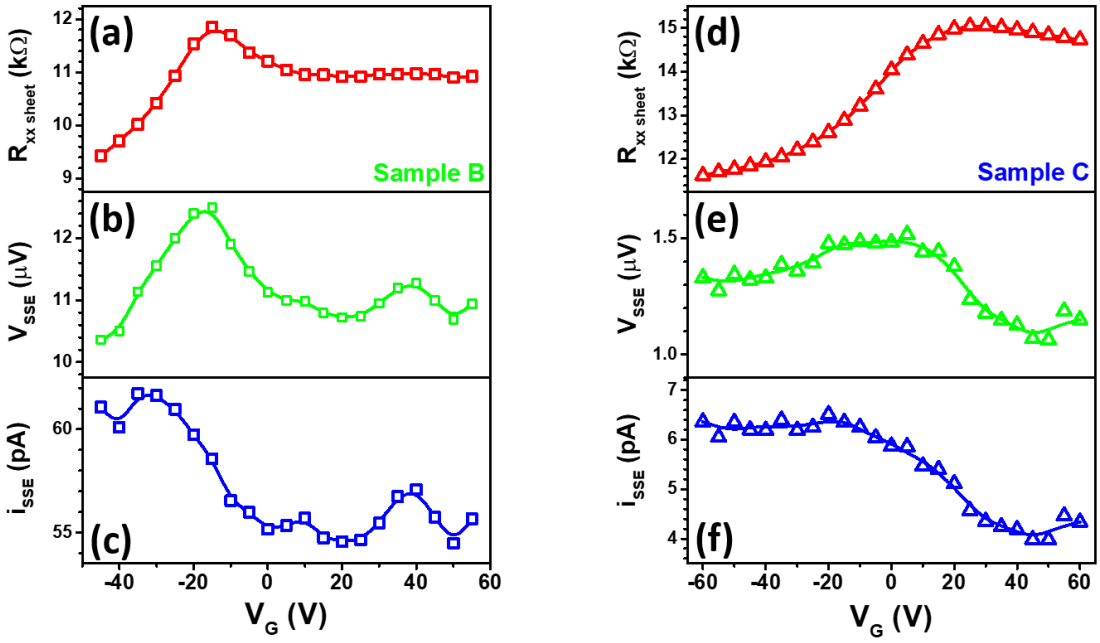

Figure 4-9 Summary of top gate effect on LSSE for two different TI samples. *a) & d) Sheet resistance, b) & e) SSE voltage and c) & f) induced SSE current dependence to top gate voltage for Sample B (x = 0.3) and Sample C (x = 0.225) respectively, at T = 20K and heating power P = 173 mW.*

value for the rest of the gating interval, compared to the mere 1% variation of sample A, however in both cases the responses to gate voltage show little variation once they get to their saturation state. As in the case of sample A, the SSE voltage (Figure 4-9(b)) and the induced SSE current (Figure 4-9(c)) show a trend that follows the TI resistivity, as in the case of sample A. In this case, the i_{SSE} has a -12.72% variation in the swept gate interval.

From sample C, we can see that the maximum value of resistivity is achieved at $V_G \approx +25V$ (Figure 4-9(d)). Just as in the case of sample A, the decrease of resistivity after the

maximum is reached is about 2%. In the case of sample C, however, the SSE voltage shows a decreasing trend after the maximum in resistivity is achieved, a similar behavior is observed for the case of the induced SSE current (Figure 4-9(e,f)), with the i_{SSE} having a decrease of 34.51% for the gate interval.

A summary with the values measured can be seen in Table 4-1, with a comparison made with the Fermi level tuning done by chemical substitution done by Jiang et al. [44], here

Sample	**x**	**$R_{xx\ sheet}$ @ V_G = 0V, T = 20K (kΩ)**	**V_G (R_{xx} max) (V)**	**i_{SSE}/P (max) pA/W**	**Δ_{iSSE} (%)**
A	0.3	7.29	+20	396	18.96
B	0.3	11.21	-14	356	-12.72
C	0.225	14.03	+25	36	34.51
Ref. [44]	0.24 - 1	10 (x = 0.24) 1 (x = 1)	0	2730 (x = 0.24) 2 (x = 1)	1.3×10^5

Table 4-1 Comparison of LSSE values obtained by top gating*. The values from Jiang et al. [44] are included for comparison.*

we normalize the i_{SSE} by the applied heater power P to make a fair comparison between the two experiments. We can observe that for the gated samples, the one with highest resistivity at V_G = 0V corresponds to sample C, followed by sample B and sample A having the smallest of the ones studied. Even though samples A and B have the same nominal bismuth substitution (x = 0.3), the gate voltage at which the maximum resistivity happens shows a large difference, making evident that sample to sample variation is an important factor when studying these systems; even so the i_{SSE}/P values between sample A and sample B are comparable. In the case of sample C, the resistivity at V_G = 0V is larger

compared to all the other samples, however the i_{SSE}/P ratio becomes lower due to a smaller SSE voltage generated. Even though the resistivity of the TI samples we studied is comparable to the ones used by Jiang et al. [44], the normalized induced SSE current differs by one order of magnitude. The tuning of the i_{SSE} by top gate voltage is only in the range of 30% in the best case we studied, while the Bi doping is able to affect by a factor of 50 when going from the range x = 1 to x = 0.24. Even if we consider the case of x = 0.23 to x = 0.24, the increase on the i_{SSE} is almost by a factor of 2.

Another factor to be considered is the effective tuning of the Fermi level by this method of gating. In single layer 2D systems like graphene, the maximum in resistivity corresponds to the Dirac point. In the case of our TI samples, however, this is not the case. We can model the TI samples as a combination of three layers: the top and bottom surface layers and a middle one corresponding to the bulk carriers, each layer contributes as a conduction channel. In the proposed model for topological SSE, the magnon-charge conversion takes place at the interface of the YIG/TI, i.e. in the bottom surface of TI. When tuning the Fermi level by top gate voltage, the largest effect occurs at the top surface, with a decreased effect on the underlying layers as a consequence of field screening. Under these circumstances, the top and bulk layers will act as shunting channels, the measured SSE voltage will be $R_{xx}\frac{V_B}{R_B}$ where R_B is the resistance of the bottom channel, V_B the voltage generated by the magnon-charge conversion and R_{xx} the total resistance of the three channels, this way the VSSE will follow the behavior of the

tuned R_{xx} but since R_B is barely effected, then the induced SSE current will have a small effect.

The effect of multiple conduction channels in TI has been studied by other groups [47], in order to effectively tune the Fermi level in TI samples a dual-gate approach has been taken with some certain degree of success. However, in the case of SSE where the interface between the materials is important, the technique of wet transfer will have a deteriorating effect. For this reason, we explore different approaches of TIG/TI growth with bottom gating capabilities:

a) YIG grown on Si/SiO_2 wafer. This approach yields a flat, polycrystalline YIG, as revealed by RHEED after the RTA process. Surprisingly, TI is able to grow layer by layer, as the characteristic streaky RHEED pattern appears while growing TI by MBE technique. However, when testing the bottom gating capabilities, the current leaking from the bottom gate electrode to the TI becomes excessively large (i_{leak} > 2 nA) for small gating intervals (V_{bg} < 2 V), and the effect on the TI resistivity and in the SSE signal is negligible (0.1%). It appears that the RTA process degrades the insulating capabilities of the 300nm SiO_2 layer, which degrades its insulating characteristics.

b) YIG grown on Pt electrode. Following the process by Aldosary et al. [48], we deposited a 5nm thick Pt strip on GGG(111) substrate, and then grew 100nm YIG, which showed single crystal order according to the obtained RHEED pattern.

Unfortunately, this approach has the same leaking problem as the YIG/SiO_2/Si approach. In the tests performed in Aldosary et al., the leaking on YIG becomes small when the temperature is decreased, however as the SSE demands the flow of heat through the structure this causes the YIG temperature to reach the interval on which its insulating capabilities as a gating interface are negated.

c) YIG grown on $SrTiO_3$(111). Strontium titanate (STO) has the appealing characteristic of displaying an extraordinary increase in its dielectric constant at low temperatures ($\kappa \approx 1000$ for $T < 20K$), which makes it on the paper the ideal candidate as a substrate for backgating, as it has been used in other experiments [49] [50]. However, this approach has its own challenges, which will be described next.

For the STO(111) substrate (500 μm thick), it is required first to prepare the surface, the process requires deionized water etching followed by RTA process at 1100°C for 2 minutes, repeating these steps three times in total [51]. This way, the STO shows very low roughness (< 2Å RMS). If the YIG layer is grown directly on top of the STO substrate, the YIG will disgregate into YIG and $YFeO_3$ (yttrium iron perovskite, YIP) phases, as corroborated by XRD analysis, this may be caused by STO being a perovskite itself will favor the FeO sublattices of YIG to rearrange in the different YIP and YIG grains that are shown in XRD (Figure 4-10(a)). The VSM measurement reveals no magnetic signal on the samples grown under these conditions. The YIP phase has a canted antiferromagnetic ordering, that for our purposes is useless in the arrangement it grows from a YIG target.

In order to favor the YIG phase over the YIP phase, we grow a buffer layer of 30nm YAG, which is grown under the same conditions as YIG; then after RTA we proceed to grow 70nm of YIG on top of this buffer layer. After the second RTA process for the buffered YIG, the XRD reveals that the YIP phase is mostly

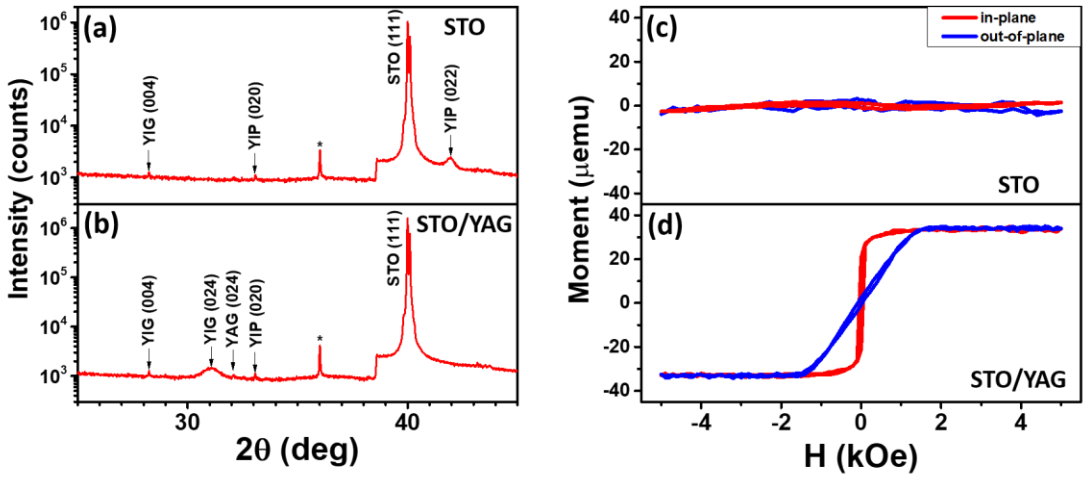

Figure 4-10 YIG grown on STO substrate. *a) XRD for 100nm YIG grown directly on STO substrate, showing the formation of YIP phase. b) XRD for 30nm YAG/70 nm YIG grown on STO, with this method the YIP phase is mostly suppressed, having the formation of polycrystalline YIG. c) VSM measurement of the YIG/STO and d)YIG/YAG/STO samples. The hysteresis loop in d) is self-explanatory.*

gone and the peaks corresponding to YIG dominate the present phases. The VSM for the samples grown under this method clearly show the magnetic behavior corresponding to YIG.

After the YIG/YAG/STO samples had the TI (x = 0.2) grown on top of them, we proceeded to do the SSE measurements using the dual gating capabilities, under the same conditions used for the top-gated devices studied previously (T = 20K, P = 173mW). The gating effect on the resistivity can be observed in Figure 4-11. The bottom gating shows a low effect

on the overall resistivity of the TI, having an increase of 1.4% in the gating interval; evidently there is no maximum/minimum value achieved by bottom gating (Figure 4-11(a)). We tuned afterwards the top gate under different bottom gate values, the difference among the three resistivity curves is an indication that even if the bottom gating effect is small, it is still measurable and not caused by any drifting effects.

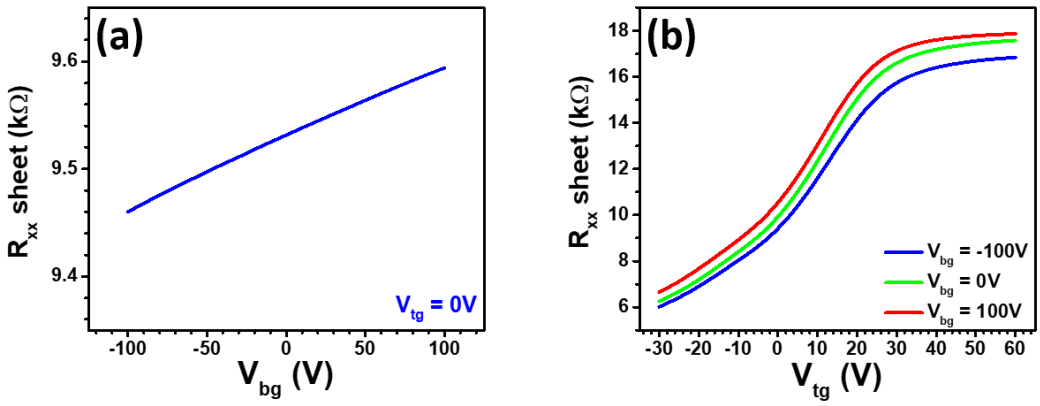

Figure 4-11 Dual gate effect on TI resistivity*. a) Bottom gate effect on sheet resistance of BST x = 0.20 at T = 20K, with a heating power P = 173 mW. b) Top gate effect on sheet resistance of the same sample, under different bottom gating conditions.*

We proceeded then to measure the LSSE on this sample to different combinations of top/bottom gate voltage values, the representative field dependence of LSSE voltage of some selected gate values can be seen in Figure 4-12(a). The effect of the bottom gate voltage on the SSE voltage is noticeable, considering the effect it has on the resistivity. For instance, for the measurements done at V_{TG} = +60V, the difference between V_{SSE} with V_{BG} = -100V and V_{BG} = +100V is 1.14 μV, which represents a change of 13.5% on the bottom gated interval. This result contrasts with the minuscule change of 1.3% in the

resistivity for the same gating interval. If we compare with the top gated effect only, we observe that there is a change in V_{SSE} of about 1.23 μV for a 300% change in the resistivity that the top gate provides. This result reveals that a small change on the bottom gate provides a much larger effect compared to the top gate, confirming that the V_{SSE} is mostly generated in the interface of the YIG/TI sample. Regarding the induced SSE current, just

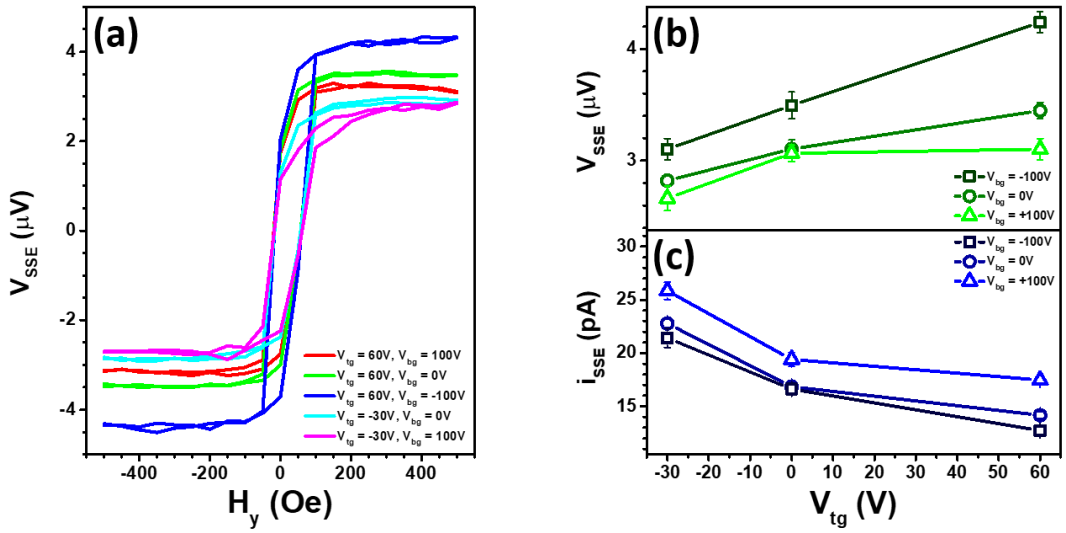

Figure 4-12 Dual gate effect on LSSE. *a) Field dependence of the LSSE voltage of a YIG/BST (x = 0.2) heterostructure for different top and bottom gate voltages. b) Longitudinal SSE voltage and c) induced SSE current dependence of top and bottom gating.*

the bottom gating provides an average change of 37.23%, which is about the same effect that the top gating exerts on i_{SSE} (about 47.91%). When combined together, the dual gate can provide up to 103% change in the induced current in the studied interval, which is an improvement compared to top gating only approach but still far away from the Fermi

level tuning by doping as it can be seen in Table 4-1, being in the same effect caused by the 1% change in doping (from x = 0.23 to x = 0.24) observed in Jiang et al. experiment.

Even with the large effect the bottom gating provides on the SSE signal, the issue about the limited effectiveness in tuning the overall Fermi level remains. It has been observed that when TI grows on polycrystalline YIG, the overall amount of charge carriers in TI increases, for the reported sample (x=0.2) we found that the charge carrier density was $n_{2D} \approx 10^{14}$ cm^{-2}, with a reduction to 10^{13} cm^{-2} when approaching the maximum in resistivity, this is one order of magnitude larger than the samples studied by Jiang et al., where for a Bi substitution that gets the Fermi level of TI close to the Dirac point (x = 0.24) the carrier density is as low as 10^{12} cm^{-2} [44]. As the quality of the interface is primordial for the observation of topological SSE, it is necessary to find a different material that can grow on substrates that may provide back gating capabilities without major alterations to the structure of the magnetic material.

In conclusion, we found that the electrostatic gating affects both the SSE voltage and SSE induced charge current, with a tunability up to 100% on the spin to charge conversion when both gates are controlled. For the topological SSE, the bottom gating provides a larger effect as expected, since the magnon to charge conversion occurs in the interface of YIG/TI. More research is deemed necessary to achieve a more efficient control of the electronic properties of YIG/TI heterostructures in order to effectively tune the TI surfaces into the Dirac point.

4.3.2 Coherent-incoherent spin wave detection on YIG/Pt bilayer

One of the main differences between SSE and spin pumping in a ferromagnetic material is the nature of the spin current generated. In the case of SSE, the spin waves are a consequence of the temperature gradient across the material, which generates incoherent spin waves in return. On the other hand, in the spin pumping technique spin waves are generated by ferromagnetic resonance, offering the prospect of a coherent mode.

In the case of ferromagnetic metal systems, the presence of parasitic effects in spin pumping, such as rectification of anomalous Nernst effect can contribute to the voltage signal, causing complications of their quantification when obtaining the ISHE measurement [52] [53], for the case of ferromagnetic insulators, as there is no charge current in the magnetic layer, this problem is mostly absent. However, the generation of spin waves by microwave injection comes with the corresponding heating from the electromagnetic wave itself, with the corresponding SSE contribution to the total ISHE, for this reason, it is necessary to study the contribution coming from both coherent and incoherent sources.

A YIG thin film with thickness equal to 20 nm is grown on a GGG (111) substrate by PLD technique as described before in Section 2.2:. RHEED image reveals single crystal structure after ex-situ RTA process, while AFM shows flat and uniform films with roughness equal to 1.3 Å RMS (Figure 4-13).

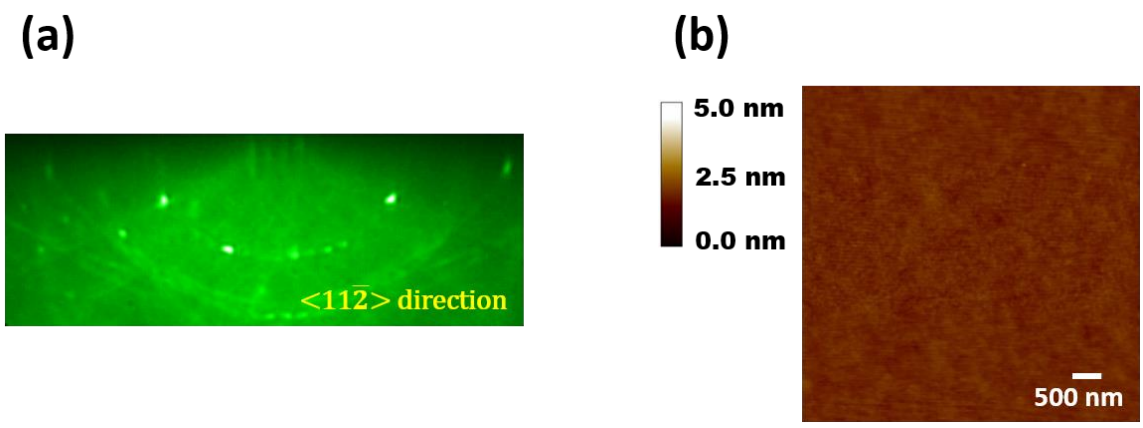

Figure 4-13 Structural and morphology characterization of YIG film on GGG(111)*. a) RHEED pattern of YIG film along the* $\langle 11\bar{2} \rangle$ *direction, displaying single crystal structure after RTA process. b) 5 μm × 5 μm AFM surface morphology scan, with an RMS roughness of 1.3 Å.*

For the SSE/spin pumping measurement, using photolithography we fabricated on top of the YIG films a 20 μm × 2 mm, 5 nm thick Pt strip as spin detector by RF sputtering, then we fabricated a 5nm Ti/45nm Au CPW parallel to each Pt detector, with a 25 μm gap between the detector and the CPW terminals. Then we performed temperature dependent LSSE/spin pumping measurements, which were carried out in a closed-cycle system down to T = 25K, and an external magnetic field up to 3.5 kOe. The microwave signal (with frequency range from 2 to 12 GHz, with 1 GHz steps) was amplitude modulated with a frequency of 2.81 kHz and an AM depth of 50%, and a power of 16 dBm (≈40 mW), the ISHE signal in the Pt detector was first measured using a lock-in amplifier. The measurement configuration can be seen in (Figure 4-14).

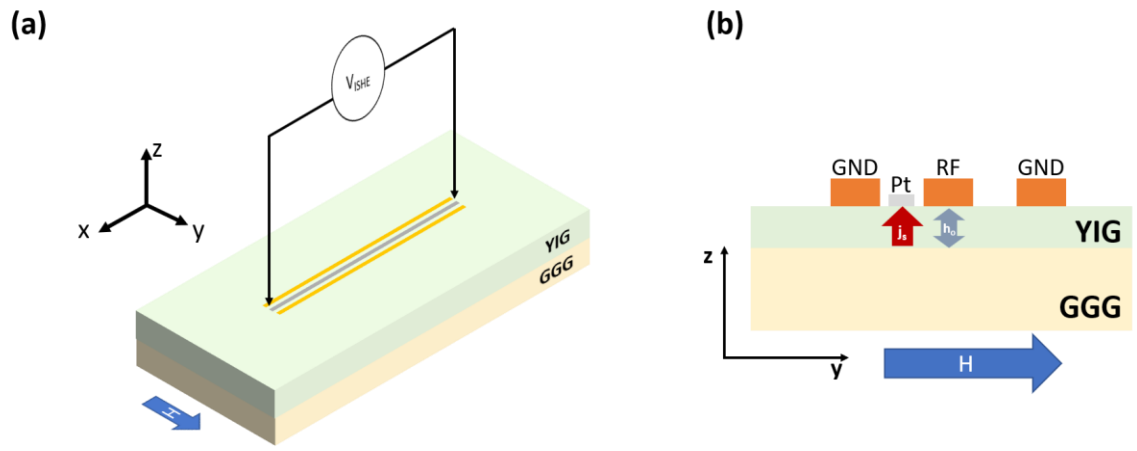

Figure 4-14 Spin pumping experimental schematic. *a) Measurement setup for spin pumping measurement, for the GGG(111)/YIG sample, indicating the direction of the applied external field and the configuration of the ISHE measurement. b) Cross section image of the spin pumping set up, indicating the direction of the generated spin current and the direction of the magnetic field vector in the microwave.*

We then proceeded to measure the ISHE voltage generated by the injection of the microwave into the sample as we swept the static magnetic field H. Figure 4-15 shows the signals measured at 300K. In Figure 4-15(a), we observe that the ISHE signal consists of two peaks, each one at $\pm H_{res}$ but with opposite sign, this is an indication that the signal is being generated by spin currents coming from YIG. The obtained peaks can be fitted by a single symmetric Lorentzian, with no evidence of antisymmetric contribution, the difference on the amplitude of these peaks is related to the LSSE generated by the increase of temperature of YIG at H_{res}, therefore this difference will be accounted in the quantification of ISHE due to coherent spin waves. There is also a step in ISHE happening at the coercive field of YIG, this signal is associated to the LSSE and it may be originated by the thermal gradient generated by the antenna in the CPW, this may be caused by dissipation caused by impedance mismatch. Figure 4-15(b) shows the frequency

dependence of the ISHE generated by spin pumping, we can appreciate in this graph that the magnitude of the ISHE signal at the FMR field for each frequency has a different amplitude, this behavior will be analyzed next.

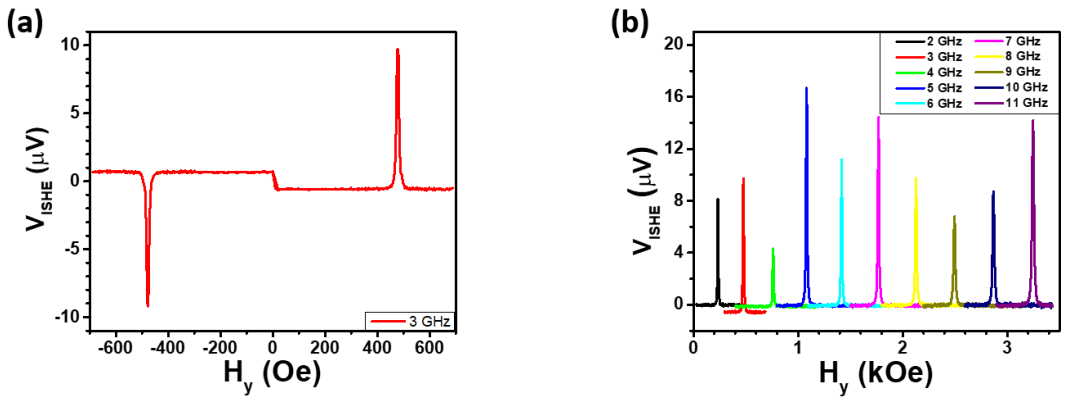

Figure 4-15 Inverse spin Hall Effect voltage in YIG/Pt bilayer. *a) Field dependent ISHE voltage for a 3 GHz microwave injected in the bilayer at T = 300K, where it can be clearly appreciated the peaks at FMR field and the switching corresponding to LSSE. b) Field dependence of the ISHE voltage at T = 300K for different microwave frequencies.*

In order to quantify the contribution of the different sources to the spin current we need to first consider the possible power absorbed by the impedance mismatch, for that purpose we take the ratio between the SSE-like signal (V_{SSE}) and the spin pumping (V_{SP}) signals at FMR field, for this purpose, we performed the temperature dependence of the first experiment and then calculated the ratio V_{SSE}/V_{SP} for different temperatures, down to T = 25K. In Figure 4-16 it can be observed the magnitude of the ISHE signal from the different sources for some selected frequencies. It can be appreciated that for the signal

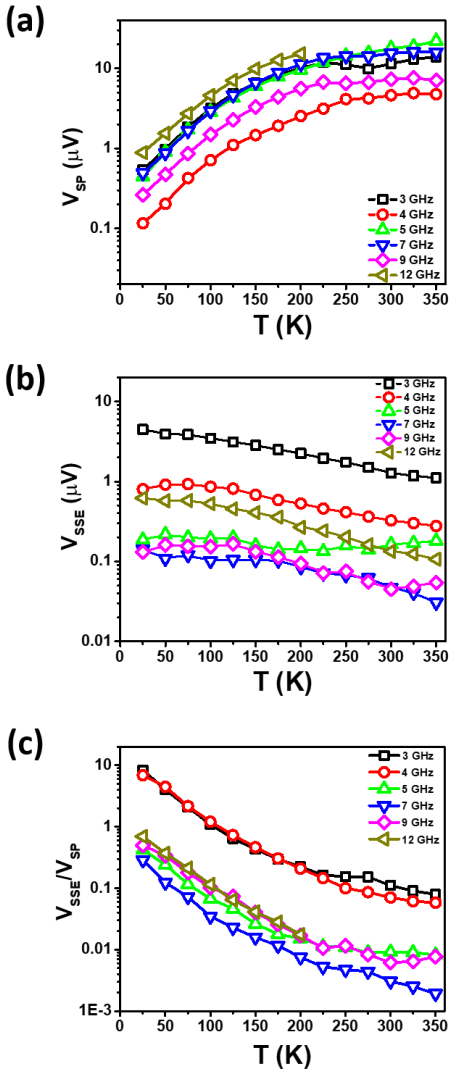

Figure 4-16 Inverse spin Hall effect signals vs. temperature in YIG/Pt bilayer. *a) ISHE voltage at FMR field and b) LSSE voltage for different microwave frequencies. It can be observed in both cases that the behavior differs among the different frequencies. c) V_{SSE}/V_{SP} ratio for the selected frequencies, showing the increasing trend as temperature decreases.*

generated by spin pumping decreases for all frequencies as temperature becomes lower although the way it decreases is different for every frequency (Figure 4-16(a)); however for the signal coming from SSE it has not a real consistent trend, as in for some frequencies it increases steadily (3 GHz), reaches a maximum values (4 GHz) or experiences ups and

downs as the temperature changes (5, 9 GHz) (Figure 4-16(b)). This behavior differs to the regular SSE observed under the standard measurement geometry, where it is observed an increasing trend as the temperature decreases, showing a maximum in the SSE signal around 100K, and then steadily decreases as T approaches to zero, this might be due to the fact that in the standard geometry (temperature gradient perpendicular to the surface) we have multiple contributions that form a continuous spin wave spectrum, while in this method we may be limiting the response to the harmonics of the microwave injected.

Once we take the ratio of V_{SSE}/V_{SP}, we realize that the curves obtained describe the same trend, with an offset on respect to the others (Figure 4-16(c)). It was observed that for the signals from microwaves with $f \leq 4$ GHz, they have a larger offset compared with the rest. This behavior has been observed before in YIG/Pt bilayers, and it is attributed to an enhancement in the spin current emission due to three-magnon splitting process [54].

To find the offset factor in the SSE/SP ratio, we find the factor *b(f)* that will make all the curves to collapse into a single one. In order to investigate if the origin of this factor *b(f)* is thermal, we evaluate the change in the resistance of the Pt with respect to temperature at different frequencies, and then compare the increase of resistance of Pt with factor *b(f)*. In this case, as it was mentioned earlier, for $f \leq 4$GHz the effect of three magnon splitting plays an important role in the spin current generation, so we are leaving out those values for this analysis. The comparison can be observed in Figure 4-17.

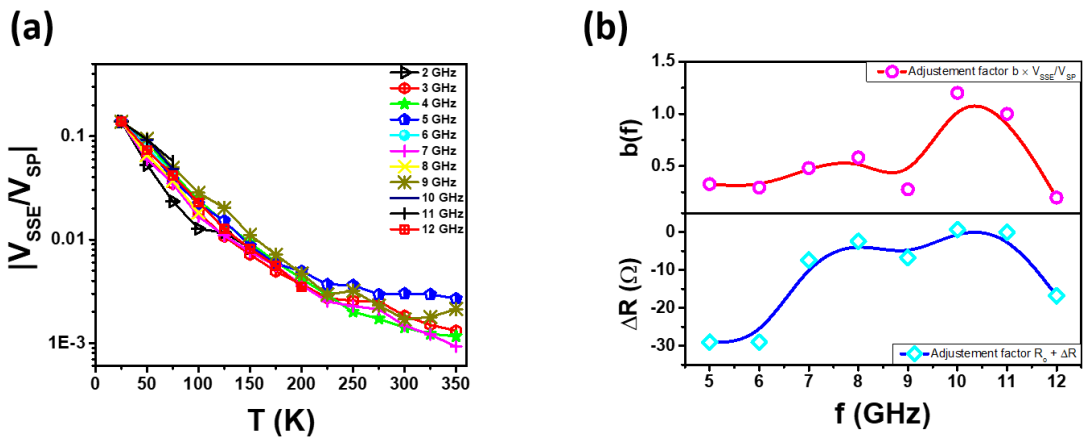

Figure 4-17 Scaling factor between spin Seebeck and spin pumping contributions. *a) Ratio V_{SSE}/V_{SP} collapsed by the term b(f). b) Comparison between the scaling factor b(f) and the change in resistance of the Pt detector at different microwave frequencies.*

It can be seen that the scaling factor *b(f)* follows roughly the same trend as the change in Pt resistance. The change in the resistance of Pt can be due to a) increased spin-current conversion, that leads in an increase of voltage between the terminals of Pt and consequently, "increasing" the resistance of Pt; b) to a change of temperature given by $\Delta R = \alpha \Delta T$, with α being the resistivity temperature coefficient for Pt. The current used to measure the R vs T curves is 200 μA, which leads to a current density of 2×10^9 A/m^2, this current density is small enough to provoke additional thermal contributions of consideration by itself. In the most extreme case (f = 5GHz), the change of voltage between terminals in Pt is about 6 mV, whereas the measured voltage coming from converted spin current into charge current is in the order of 10 μV; therefore we attribute this change in resistivity by the change of temperature due to the power absorbed by the system due to the microwave signal, in consequence the scaling factor b(f) should have a

contribution from this temperature increase. This analysis allows us to establish the bases for a more complete analysis in the study of coherent/incoherent spin wave transmission. According to the theoretical proposal for spin pumping, coherent spin waves should be possible (i.e, having a non-zero contribution) at T = 0K [37]. An experiment by Chen et al. has been performed to elucidate the coherent/incoherent contribution to the spin pumping in YIG/Pt [55], showing that both uniform FMR and spin wave resonance modes display a power-law relationship thus revealing their incoherent nature. Further work is necessary to elucidate the contributions of the different sources of spin currents through a ferromagnetic insulator such as YIG.

4.3.3 Spin-current generation through compensation in TbIG

As it has been stated previously, the SSE is a consequence of the spin current generated by a temperature gradient in a magnetic material. Moreover, in the case of a ferromagnetic insulator this spin current is the consequence of spin waves created by the thermal excitations, however the mechanism under which the SSE contributes to the distinct spin wave modes is still under debate. In the case of REIGs, the presence of different magnetic sublattices causes a more complicated magnon spectrum compared to materials with a single magnetic sublattice. In the case of TbIG, the Tb^{3+} ion has a contribution to the magnetization that can make $\vec{M}$ switch from being antiparallel to parallel to the d sublattices below the compensation temperature (Figure 4-18).

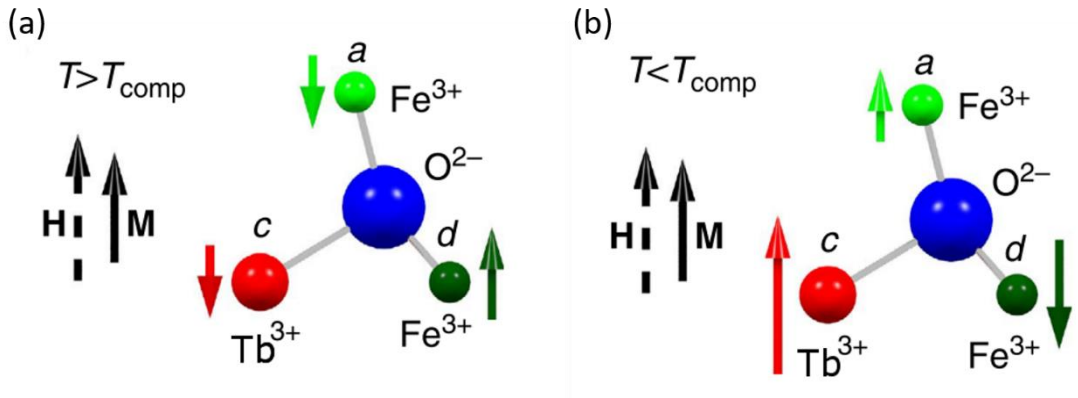

Figure 4-18 Magnetic sublattices through compensation in TbIG. *The different magnetic sublattices in TbIG shown for a) $T > T_{comp}$ and b) $T < T_{comp}$. Below compensation, the magnetization M is parallel to the d sublattice, while above compensation, M is antiparallel to the d-site. Adapted from Geprägs, S. et al. Nat. Comm.* ***7*** *10452 (2015).*

In an attempt to understand the mechanism of spin wave generation in TbIG, we performed LSSE and spin pumping experiments on GGG(100)/TbIG and SGGG(111)/TbIG, these substrates were chosen because according to (2-4) and (2-5), the magnetoelastic effect on TbIG will align the magnetization in the in-plane direction. Additionally, we prepared a GGG(110)/TbIG sample, which is PMA at room temperature, as this sample has its magnetization out-of-plane, the feasibility of getting a ISHE signal from spin pumping is null due to being in the wrong geometry, therefore we measured only the LSSE on this sample (GGG(110)/TbIG).

The TbIG thin films with thickness equal to 20nm were grown by PLD technique as described in Section 2.2: RHEED image reveals single crystal structure after ex-situ RTA process, while AFM shows flat and uniform films with roughness < 2.5 Å RMS (Figure 4-19).

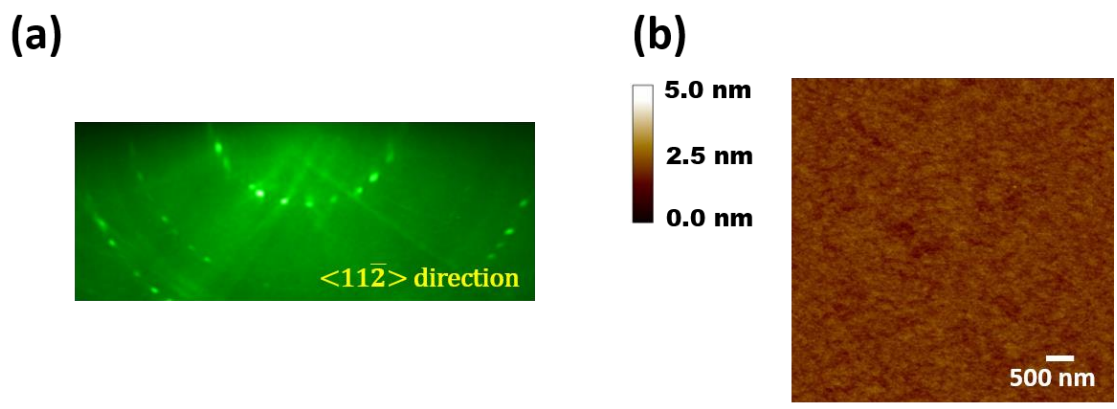

Figure 4-19 Structural and morphology characterization of TbIG film on SGGG*. A) RHEED pattern of TbIG film along the* $\langle 11\bar{2} \rangle$ *direction, displaying single crystal structure after RTA process. b) 5* $\mu m \times 5$ μm *AFM surface morphology scan, with an RMS roughness of 2.2 Å.*

For the LSSE experiment, we patterned a 1.8 mm × 100 μm Hall bar using photolithography, and then deposited 5 nm Pt on top of the TbIG film. Then, we grew 100 nm Al_2O_3 on top of the Hall bar as an insulating layer, and finally we fabricated a 5 nm Ti/45 nm Au bar aligned right on top of the Hall channel, this way when we inject a current through this line it will act as a heater to the device. For the spin pumping experiments,

we fabricated a CPW on top of the TbIG films as described in Subsection 4.3.2 (Figure 4-14). (Figure 4-14).

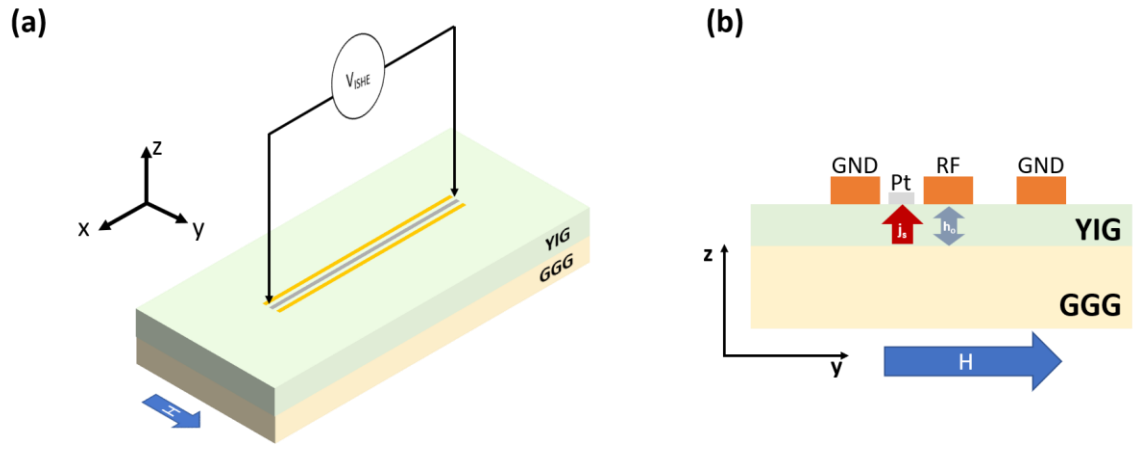

Figure 4-14 Spin pumping experimental schematic. *a) Measurement setup for spin pumping measurement, for the GGG(111)/YIG sample, indicating the direction of the applied external field and the configuration of the ISHE measurement. b) Cross section image of the spin pumping set up, indicating the direction of the generated spin current and the direction of the magnetic field vector in the microwave.*

We performed the temperature dependent LSSE in a Quantum Design PPMS system down to T = 2K, and an external magnetic field up to 14 T. The heater current was set to 20 mA and the ISHE signal in the Pt detector was measured using a Keithley 2182 nanovoltmeter. The temperature of the Pt was calibrated by an R vs T curve measured with both the heater on and off, and its effects were considered in the results.

We performed first the LSSE experiment, in order to ascertain the existence of spin currents in our heterostructures due to a thermal gradient. An example of the behavior we observed can be seen in Figure 4-20. For this sample, we can see a at first that the hysteresis loop is negative ($V_{SSE} > 0$ for $H_y < 0$), as observed in YIG/Pt heterostructure

under the same experimental geometry. As we decreased the temperature, the magnitude of V_{SSE} decreases until it the signal becomes flat, and then it reverses the sign of the LSSE hysteresis loop ($V_{SSE} > 0$ for $H_y > 0$).

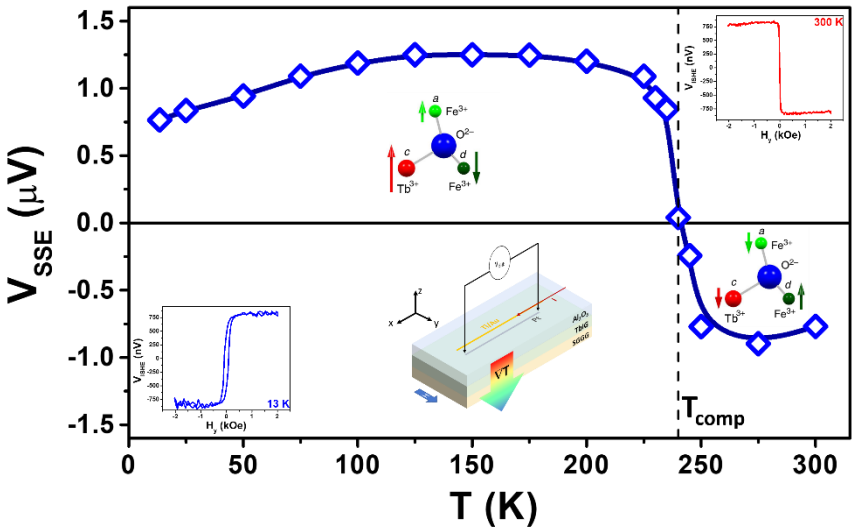

Figure 4-20 Temperature dependence of longitudinal SSE in SGGG(111)/TbIG(20nm). *The magnitude of the SSE decreases abruptly at T = 240K and changes sign, as a consequence of the reversal of the magnetization sublattices in the garnet structure.*

To make a fair comparison among the different studied samples, we obtained the induced SSE current (i_{SSE}) and then normalized it by the power applied by the heater. The behavior of T_{comp} among the measured samples is not only different to the values corresponding to TbIG bulk ($T_{comp(bulk)}$ = 245K) but different among themselves (Figure 4-21). This behavior has been observed in GdIG thin films [56], although there is no clear answer on the origin of this variation on T_{comp}. The running hypotheses are based on a reduction of the magnetic exchange strength due to a) an iron deficiency in the rare earth iron garnet structure [57],

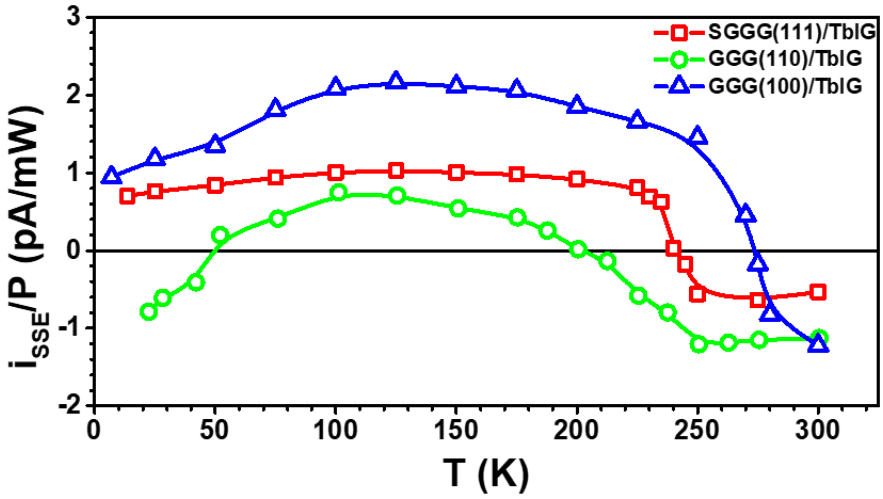

Figure 4-21: Normalized induced SSE current in TbIG grown on different substrates. *The graph clearly shows different compensation temperatures among the samples, and it also shows a second sign change for TbIG grown on GGG(110).*

b) interdiffusion of another element in the rare earth iron garnet [56] and c) strain in the lattice structure. The iron deficiency , although not impossible, is quite improbable in our case, since the samples were grown under the same conditions using the same target. The interdiffusion with another element was mentioned by Geprägs et al. as a possibility since in their experimental setup they provided the thermal gradient by direct contact of Cu/AlN blocks; under our geometry the Al_2O_3 layer is grown at 200°C by ALD which makes highly unlikely the migration of Al atoms into the garnet structure, therefore the strain cause seems to be the more feasible explanation, however a systematic study of strain effect on the compensation temperature is necessary. Another difference among the samples is that the one grown on GGG(110) is the only one to display a second change in SSE sign around T ≈ 50K. In GdIG thin films, this second change of sign has been observed

and it has been attributed to the competition of two transmission modes of magnons: one soft, gapless dispersion mode (α-mode) and one gapped optical mode (β-mode) [56]. In order to validate this model, it is needed to analyze the case of TbIG and explore the effects of both strain and film orientation in the spin current transmission.

Once we have confirmed the presence of spin current by SSE, we proceeded to do the spin pumping experiment on the samples with in-plane anisotropy (GGG(100) and SGGG(111)). Before proceeding, we measured the Hall/SMR in both samples in order to establish the magnetic field necessary to saturate the sample and then estimate the required frequency to obtain the resonance according to Kittel equation (Equation (3-5) For the sample on GGG(100), we found that $H_{sat} = 4\pi M_{eff} = 5600$ Oe, and for SGGG(111), $4\pi M_{eff} = 2500$ Oe (Figure 4-22). Assuming $g_{TbIG} = 1.5$ from Landé equation [58], then we obtain for f = 3GHz, $H_{res} = 345$ Oe for the sample grown on GGG(100), and $H_{res} = 650$ Oe for the sample grown on SGGG(111).

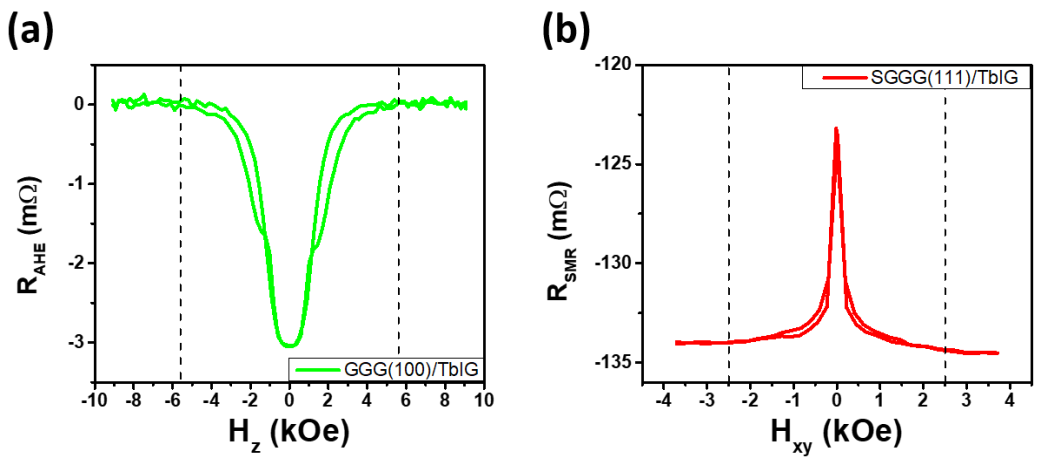

Figure 4-22 Saturation field of TbIG thin films. *Extraction of the demagnetizing field $4\pi M_{eff}$ by sweeping magnetic field a) along the hard axis using AHE, b) along X-Y axis using SMR. The shape of AHE in GGG(100)/TbIG is due to heavy mixing with SMR.*

For the spin pumping experiment, we used the same experimental setup as used in Subsection 4.3.2. We performed a first measurement at room temperature with a microwave signal of 3 GHz and P = 16 dBm (≈ 40mW), sweeping from positive to negative field in order to observe the SSE signal obtained by the previous method. Since we were able to recover the SSE signal with this method for both samples, thus ensuring the presence of spin current coming from the TbIG layer, then we proceeded to sweep the field in the positive range exclusively. No spin pumping signal was observed in the whole interval of magnetic field swept (Figure 4-23). We attempted changing the microwave frequency to different values between 1-20 GHz, yet we were unable to detect a feature corresponding to ISHE generated by spin pumping.

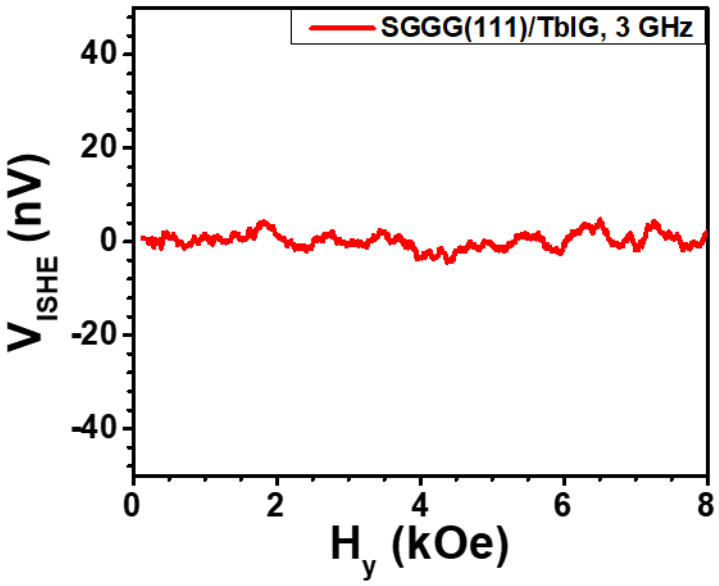

Figure 4-23 Field dependent ISHE signal for SGGG(111)/TbIG. *Dependence of ISHE signal to applied external field H in an interval from 0-8 kOe, after linear background subtraction. No peak is observed in the whole interval.*

The lack of observable peak in the spin pumping signal is something that we were not expecting, and it deserves further investigation. One possibility is that the coherent spin waves generated by spin pumping are scattered by the magnetic sublattices of Tb, another possibility is that the resonance peak becomes too broad that it gets lost within the background of the ISHE signal, therefore it is necessary to design a series of experiments to verify the previous hypotheses.

4.3.4 Effect of antiferromagnetic ordering in spin wave transmission on YIG/Cr_2O_3/Pt heterostructures

The use of antiferromagnetic insulators have attracted a great deal of attention due to their unique interesting properties such as ultra-fast spin dynamics, absence of stray fields and robustness against magnetic field perturbations [59]. Recently, it was found that thin antiferromagnetic insulator layers enhance spin current transmission around their antiferromagnetic phase transition temperature when they are inserted between a ferromagnetic insulator and a heavy metal, such as the NiO and CoO layers in YIG/NiO/Pt [60] and YIG/CoO/Pt [61] [62] respectively. In both cases, the enhancement is attributed to the magnon and spin fluctuations happening in the antiferromagnetic layer. Another antiferromagnetic insulator that has interesting properties is Cr_2O_3, this material has a hexagonal crystal structure on which the Néel vector (the antiferromagnetic equivalent to the $\vec{M}$ vector in ferromagnetic materials) lays parallel to the c-axis [63](Figure 4-24).

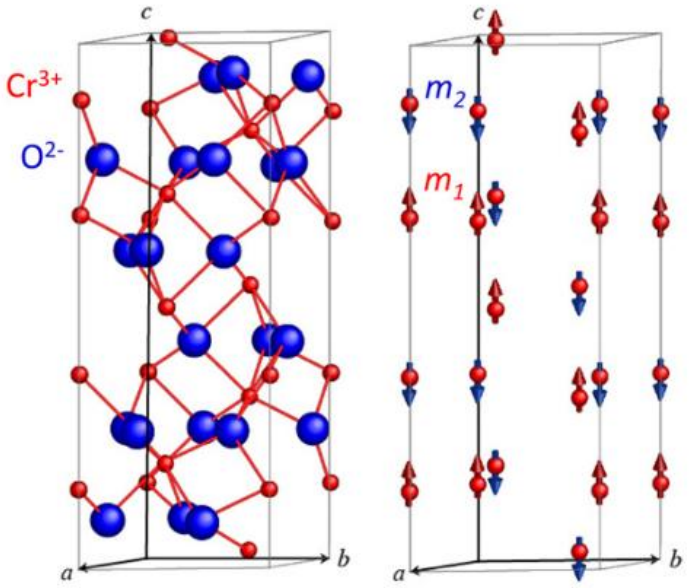

Figure 4-24 Crystal and magnetic structure of Cr_2O_3. *Diagram displaying the array of Cr3+ and O2- ions in the hexagonal crystal structure of Cr_2O_3, and the orientation of the Néel vector $\vec{m}_1 + \vec{m}_2$. Adapted from Iino, T. et al. Appl. Phys. Lett.* ***114*** *2 (2019).*

Recently, Qiu et al. [64] showed in a YIG/Cr_2O_3/Pt heterostructure a sharp decrease on the SSE signal when the temperature was below the Néel temperature of Cr_2O_3 ($T_N \approx$ 295K, Figure 4-25), this spin current blockage is attributed to the spin-orbit torque absorption exerted by the out-of-plane component of the Néel vector in Cr_2O_3, however, it remains unclear the effect of the orientation of the antiferromagnetic spin in the spin current transmission. To prove this, it is necessary to investigate the effects on spin current transmission of intermediate Cr_2O_3 layers with orientation different to the one studied by Qiu et al.

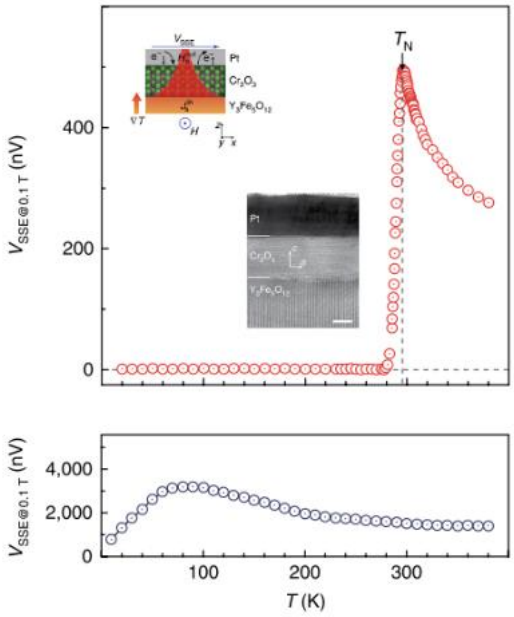

***Figure 4-25 Spin current transmission through AFM Cr_2O_3 layer**. SSE voltage along a Pt detector for a YIG/Cr2O3/Pt (top) and YIG/Pt (bottom) heterostructures. The TEM image reveals the single crystal structure of Cr_2O_3, with the c-axis perpendicular to the plane in this experiment. Adapted from Qiu et al. Nat. Mater. **17** 7 (2018)*

We grew a 20 nm thick YIG thin film on top of a GGG(111) substrate, by the procedure described before in Section 2.2:. We obtained the RHEED pattern after the RTA process which corroborates its single crystal structure, the AFM revealed an ultra-flat surface with roughness equal to 1.5 Å RMS (Figure 4-26(a,b)). We measured then the FMR derivative absorption using a X-band microwave cavity with f = 9.32 GHz with the field parallel to the sample, which showed a single peak which can be fitted with a single Lorentzian derivative. Right after this, we covered half of our sample and then deposited on the exposed region 10nm of Cr_2O_3 at 400°C by PLD technique. After this, we annealed one more time the sample at 800°C for 120 seconds in an attempt to improve its crystallinity.

The RHEED of the YIG/Cr_2O_3 side of the sample showed the formation of concentric rings, this is a characteristic of a polycrystalline structure of the grown Cr_2O_3 (Figure 4-26(c)). The AFM performed in that region showed a rougher surface (8 Å RMS), however there was no evidence of cracks or pinholes (Figure 4-26(d)).

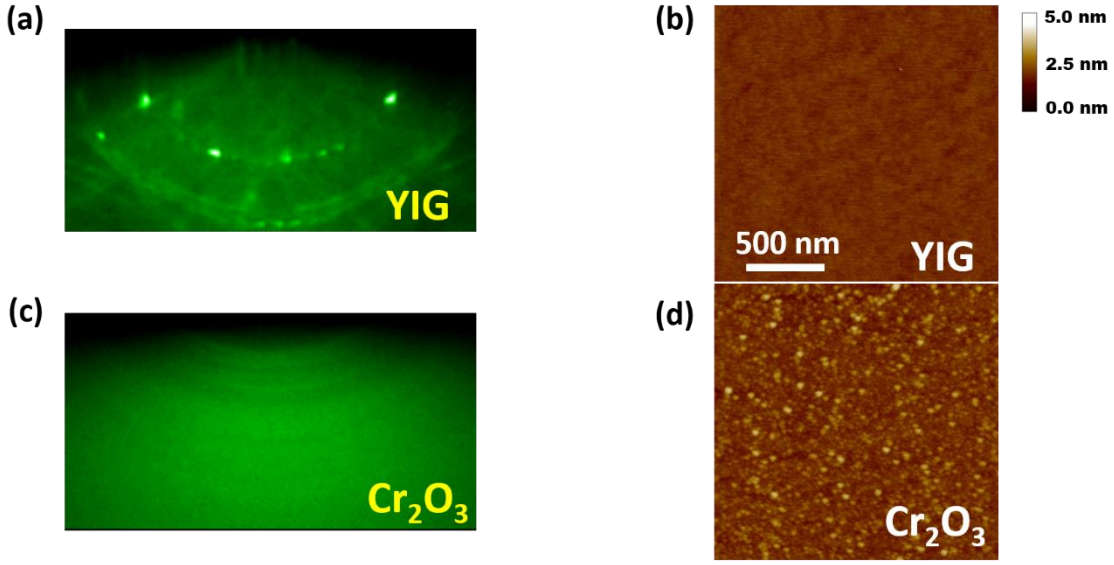

Figure 4-26 Surface characterization of YIG/Cr_2O_3 bilayer*. a) RHEED pattern for YIG film along the* $\langle 11\bar{2} \rangle$ *direction, showing single crystal structure. b) AFM of YIG, with a roughness of 1.5 Å RMS. c) RHEED pattern of Cr_2O_3 on top of YIG, the concentric rings are evidence of polycrystalline array. d) AFM of Cr_2O_3 on top of YIG, with a roughness of 8 Å RMS, there is no evidence of cracks or holes on the probed surfaces.*

For the spin current transmission experiment, we fabricated a CPW in the way described in Subsection 4.3.2, in both sections of the sample (YIG/Cr_2O_3/Pt and YIG/Pt). We then performed temperature dependent LSSE/spin pumping measurements using a setup equivalent to the one shown in Figure 4-14, which were carried out in a closed-cycle system in a 25K - 340K temperature interval, and an external magnetic field up to 3.5 kOe.

The microwave signal (with frequency range from 2 to 12 GHz, with 1 GHz steps) was amplitude modulated with a frequency of 2.81 kHz and an AM depth of 50%, and a power of 16 dBm (≈40 mW), the ISHE signal in the Pt detector was first measured using a lock-in amplifier. The resulting signal in both YIG/Pt and YIG/Cr_2O_3/Pt heterostructures showed a sign reversal on the ISHE signal when the direction of the applied field is inverted, and the small field measurement describes the magnetic hysteresis of YIG, indicating that the signal is generated indeed by the spin currents coming from the YIG layer, also from the LSSE signal we do not observe any exchange bias, so any magnetic interface effect due to exchange coupling between YIG and Cr_2O_3 is discarded.

As we varied the temperature, we observe that for both spin pumping and LSSE experiments that the magnitude of the ISHE signal increased as it approached T = 295K, experiencing a decrease as the temperature goes apart of this value (Figure 4-27). For T < 295K, we can appreciate that the decrease of the magnitude of the ISHE decreases abruptly for both spin pumping and LSSE experiments, while for T > 295K this decreases exponentially corresponding to the behavior of the Cr_2O_3 in its paramagnetic regime, where the spin fluctuations allow the transmission of the spin current through the Cr_2O_3 layer. The sudden decrease in the ISHE signal below 295K corresponds to the results observed by Qiu et al. [64] These results show that there is no difference in the behavior between coherent and incoherent transmission modes through the Cr_2O_3 layer.

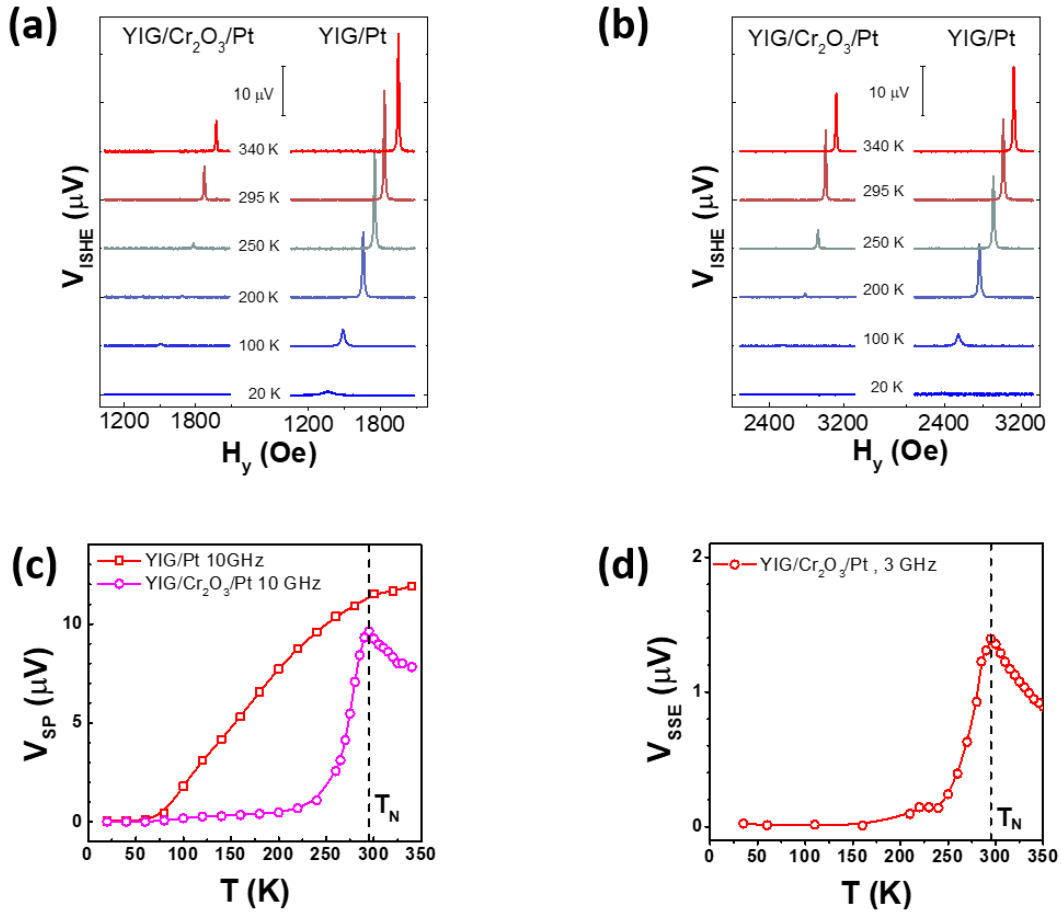

Figure 4-27 Spin current transport in YIG/Cr_2O_3/Pt heterostructure. *Comparison of the magnetic field dependence of the ISHE voltage obtained by spin pumping at different temperatures at a microwave frequency a) 7GHz and b) 10 GHz between the YIG/Pt/Cr_2O_3 heterostructure and the control sample YIG/Pt, showing an evident decrease of the magnitude of the ISHE below Néel temperature of Cr_2O_3. c) Temperature dependence of the ISHE signal at FMR field obtained at 10 GHz for both YIG/Pt and YIG/Cr_2O_3/Pt heterostructures, d) LSSE voltage generated at 3 GHz in the YIG/Cr_2O_3/Pt heterostructure, showing the same behavior as the signal obtained by spin pumping.*

From the spin pumping results, we extracted the temperature dependence of the resonance field H_{res} and the linewidth ΔH of both YIG/Pt and YIG/Cr_2O_3/Pt heterostructures and using the same procedure as in Chapter 3: , we obtained the temperature dependence of the Gilbert damping α in order to study the effect of the

antiferromagnetic ordering. The corresponding graph of α vs T for both YIG/Pt and YIG/Cr_2O_3/Pt heterostructures can be observed in Figure 4-28.

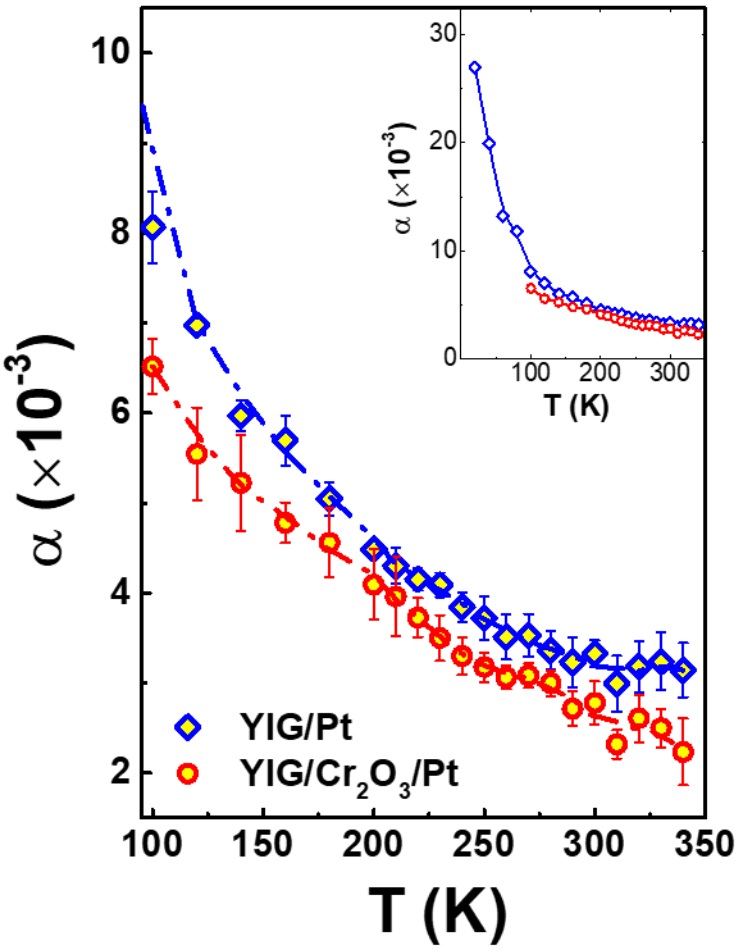

Figure 4-28 Temperature dependence of Gilbert damping α on YIG/Cr_2O_3/Pt and YIG/Pt heterostructures. *The inset shows the full temperature range (25K – 340K), for the YIG/Cr_2O_3/Pt heterostructure no signal at any frequency was measurable below 100K.*

The first thing that we notice is that in both samples, α shows an increase as the temperature decreases, this behavior has been consistently observed in YIG thin films and it is attributed to the presence of crystalline defects [65]. One interesting fact is that for

all the temperatures probed, the damping showed to be slightly larger in YIG/Pt than in YIG/Cr_2O_3/Pt samples, this can be explained if we remember that α is associated to the angular momentum of the precessing magnetization vector (Section 1.2:). When the incoming spin wave goes through the Cr_2O_3 layer, it loses angular momentum so when it gets to the Pt interface, the transferred angular momentum is smaller, giving a smaller damping as a result. However, the most interesting finding in this experiment is the fact that the damping is not altered by the antiferromagnetic phase transition. This result demands a careful analysis and further experimental for its confirmation.

Transmission electron microscopy (TEM) and energy dispersive spectroscopy (EDS) were performed in a second sample prepared under the exact same conditions as the first one, we corroborated first it had a similar RHEED pattern and morphology as the ones showed in Figure 4-26, we deposited a 10 nm Pt layer to study the interface of Pt and Cr_2O_3 as well. A total of thirty images from different regions within the sample were taken and analyzed. The EDS shows sharp and well-defined interfaces, showing no indication of layer intermixing (Figure 4-29(a)). The high resolution TEM showed what we had previously observed in RHEED: the Cr_2O_3 layer displays polycrystalline grains, with an average diameter of 15 nm (Figure 4-29(b)).

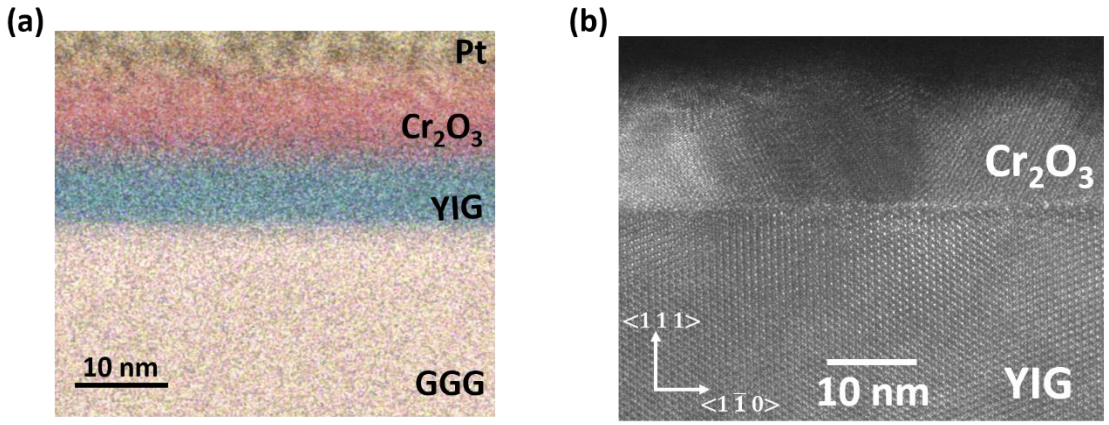

Figure 4-29 Structural characterization of YIG/Cr_2O_3/Pt heterostructure. *a) EDS image showing the interfaces forming the heterostructures, showing no layer intermixing. b) HRTEM image showing the single crystal structure of YIG, in contrast the Cr_2O_3 layer shows polycrystalline grains, with an average size of 15 nm.*

In order to establish the orientation of the Cr_2O_3 grains in the heterostructure, we performed on the high resolution TEM images the fast Fourier transform (FFT) of selected regions containing both YIG and a single Cr_2O_3 grain, this way we analyzed the corresponding orientation of the different Cr_2O_3 grains present in the heterostructure. In Figure 4-30, we can observe two different examples of the FFT of the selected region in the HRTEM (insets), with the corresponding reflections for (0006) plane in Cr_2O_3 and (444) and $(22\bar{4})$ in YIG . In these representative examples it is evident that the c-axis of Cr_2O_3, on which the Néel vector is aligned (Figure 4-24) is not parallel to the normal vector of the plane of our sample (444), and even in some cases this vector is almost parallel to the sample plane (Figure 4-30(b)). These findings reveal that the model proposed by Qiu et al. [64] for the blocking of the spin current by the Cr_2O_3 layer is not correct. Therefore, it is necessary to propose a new spin-current transmission model for antiferromagnetic

materials. In principle, the propagation of spin currents is determined by the thermal population of magnons, the magnon mean free path and the magnon energy gap [66], although this model does not describe appropriately the sharp decay in the spin current transmission below the Néel temperature. We propose doing a careful analysis of all the tested antiferromagnetic materials in order to propose a unified spin current transmission model.

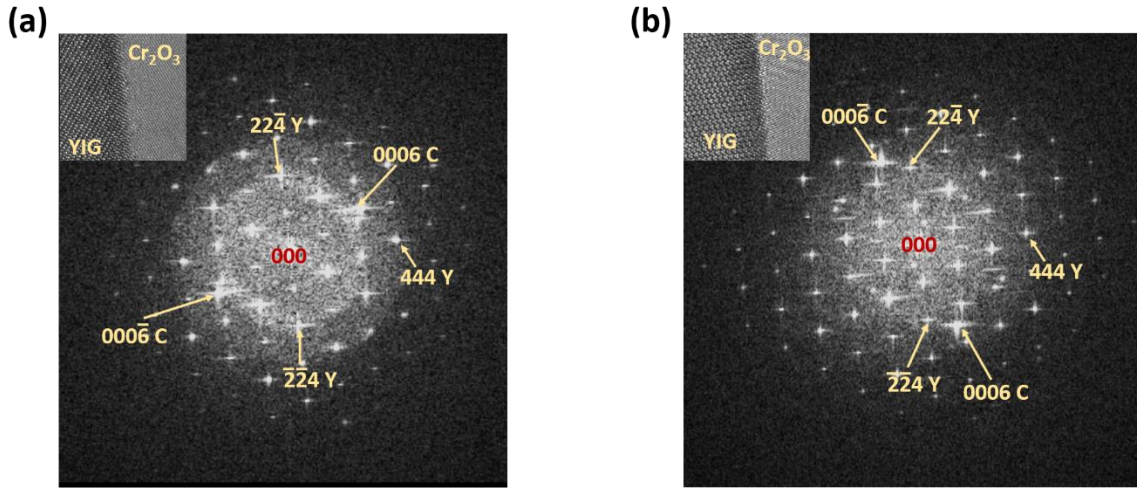

Figure 4-30 FFT analysis of HRTEM images of YIG/Cr_2O_3 bilayer. *The FFT corresponds to the area shown in the inset of each image, it can be appreciated the reflection corresponding to the c-axis vector of Cr_2O_3, labeled as 0006 C, which is clearly not aligned in any case to the vector normal to the plane, which is labeled as 444 Y. In these images, the angle between (0006) C and (444) Y is a) 23°, b) 77°.*

References

[1] S. Geller and M. A. Gilleo, "The crystal structure and ferrimagnetism of yttrium-iron garnet, Y3Fe2(FeO4)3," *J. Phys. Chem. Solids,* vol. 3, 1957.

[2] S. Geller, H. J. Williams, R. C. Sherwood, J. P. Remeika and G. P. Espinosa, "Magnetic study of the lighter rare-earth ions in the iron garnets," *Phys. Rev.,* vol. 131, no. 3, 1963.

[3] S. Geller, J. P. Remeika, R. C. Sherwood, H. J. Williams and G. P. Espinosa, "Magnetic study of the heavier rare-earth iron garnets," *Phys. Rev.,* vol. 137, no. 3A, 1965.

[4] P. Sharma, "How to create a spin current," *Science,* vol. 28, no. 5709, 2005.

[5] J. E. Hirsch, "Spin Hall Effect," *Phys. Rev. Lett.,* vol. 83, no. 9, 1999.

[6] B. F. Miao, S. Y. Huang, D. Qu and C. L. Chien, "Inverse Spin Hall Effect in a Ferromagnetic Metal," *Phys. Rev. Lett.,* vol. 111, no. 6, p. 066602, 2013.

[7] Y. Kajiwara, K. Harii, S. Takahashi, J. Ohe, K. Uchida, M. Mizuguchi, H. Umezawa, H. Kawai, K. Ando, K. Takanashi, S. Maekawa and E. Saitoh, "Transmission of electrical signals by spin-wave interconversion in a magnetic insulator," *Nature,* vol. 464, no. 7286, pp. 262-266, 2010.

[8] M. N. Baibich , J. M. Broto, A. Fert, F. Nguyen van Dau, F. Petroff, P. Etienne, G. Creuzet, A. Friederich and J. Chazelas, "Giant magnetoresistance of (001)Fe/(001)Cr magnetic superlattices," *Phys. Rev. Lett.,* vol. 61, no. 21, 1988.

[9] M. Farle, B. Mirwald-Schulz, A. N. Anisimov, W. Platow and K. Baberschke, "Higher-order magnetic anisotropies and the nature of the spin-reorientation transition in face-centered-tetragonal Ni(001)/Cu(001)," *Phys. Rev. B,* vol. 55, no. 6, pp. 3708-3715, 1997.

[10] Z. Q. Qiu, J. Pearson and S. D. Bader, "Asymmetry of the spin reorientation transition in ultrathin Fe films and wedges grown on Ag(100)," *Phys. Rev. Lett.,* vol. 70, no. 7, pp. 1006-1009, 1993.

[11] C. Tang, P. Sellappan, Y. W. Liu, Y. D. Xu, J. E. Garay and J. Shi, "Anomalous Hall hysteresis in Tm3Fe5O12/Pt with strain-induced perpendicularmagnetic anisotropy," *Phys. Rev. B,* vol. 94, no. 14, p. 140403, 2016.

[12] M. Kubota, A. Tsukazaki, F. Kagawa, K. Shibuya, Y. Tokunaga, M. Kawasaki and Y. Tokura, "Stress-Induced Perpendicular Magnetization in Epitaxial Iron Garnet Thin Films," *Appl. Phys. Express,* vol. 5, no. 10, p. 103002, 2012.

[13] S. Iida, "Magnetostriction Constants of Rare Earth Iron Garnets," *J. Phys. Soc. Jpn.,* vol. 22, no. 5, pp. 1201-1209, 1967.

[14] P. Sellappan, C. Tang, J. Shi and J. E. Garay, "An integrated approach to doped thin films with strain tunable magnetic anisotropy: Powder synthesis, target preparation and pulsed laser deposition of Bi:YIG," *Mater. Res. Lett.,* vol. 5, pp. 41-47, 2017.

[15] G. Winkler, Magnetic garnets, Braunschweig: Vieweg, 1981.

[16] E. R. Rosenberg, L. Beran, C. O. Avci, C. Zeledon, B. Song, C. González Fuentes, J. Mendil, P. Gambardella, M. Veis, C. García, G. S. Beach and C. A. Ross, "Magnetism and spin transport in rare-earth-rich epitaxial terbium and europium iron garnet film," *Phys. Rev. Mater.,* vol. 2, 2018.

[17] E. Anastassakis, "Strained superlattices and heterostructures: Elastic considerations," *J. Appl. Phys.,* vol. 68, no. 9, pp. 4561-4568, 1990.

[18] A. Navarro-Quezada, A. G. Rodríguez, M. A. Vidal and H. Navarro-Contreras, "In-plane and out-of-plane lattice parameters of [11n] epitaxial strained layers," *J. Cryst. Growth,* vol. 291, no. 2, pp. 340-347, 2006.

[19] T. B. Bateman, "Elastic Moduli of Single-Crystal Europium Iron Garnet and Yttrium Iron Garnet," *J. Appl. Phys.,* vol. 37, no. 5, pp. 2194-2195, 1966.

[20] H. L. Alberts, "Elastic constants of single crystal terbium iron garnet," *J. Phys. Chem. Solids,* vol. 41, no. 10, p. 1161, 1980.

[21] G. Bochi, C. A. Ballentine, H. E. Inglefield, C. V. Thompson and R. C. O'Handley, "Perpendicular magnetic anisotropy, domains, and misfit strain in epitaxial Ni/Cu 1− x Ni x/Cu/Si (001) thin films," *Phys. Rev. B,* vol. 52, no. 10, p. 7311, 1995.

[22] C. Chappert and P. Bruno, "Magnetic anisotropy in metallic ultrathin films and related experiments on cobalt films," *J. Appl. Phys.,* vol. 64, no. 10, pp. 5736-5741, 1988.

[23] L. J. Cornelissen, J. Liu, R. A. Duine, J. B. Youssef and B. J. van Wees, "Long-distance transport of magnon spin information in a magnetic insulator at room temperature," *Nat. Phys.,* vol. 11, no. 12, pp. 1022-1026, 2015.

[24] B. L. Giles, Z. H. Yang, J. S. Jamison and R. S. Myers, "Long-range pure magnon spin diffusion observed in a nonlocal spin-Seebeck geometry," *Phys. Rev. B,* vol. 92, no. 22, p. 224415, 2015.

[25] V. H. Ortiz, M. Aldosary, J. Li, Y. Xu, M. I. Lohmann, P. Sellappan, Y. Kodera, J. E. Garay and J. Shi, "Systematic control of strain-induced perpendicular magnetic anisotropy in epitaxial europium and terbium iron garnet thin films," *APL Mat.,* vol. 6, no. 12, 2018.

[26] Y. Krockenberg, K. S. Yun, T. Hatano, S. Arisawa, M. Kawasaki and Y. Tokura, "Layer-by-layer growth and magnetic properties of Y3Fe5O12 thin films on Gd3Ga5O12," *J. Appl. Phys,* vol. 106, no. 12, 2009.

[27] H. Wang, C. Du, P. C. Hamel and F. Yang, "Strain-tunable magnetocrystalline anisotropy in epitaxial Y3Fe5O12 thin films," *Phys. Rev. B,* vol. 89, no. 13, 2014.

[28] J. J. Bauer, E. R. Rosenberg and C. A. Ross, "Perpendicular magnetic anisotropy and spin mixing conductance in polycrystalline europium iron garnet thin films," *Appl. Phys. Lett.,* vol. 114, no. 5, 2019.

[29] C. L. Jermain, H. Paik, S. V. Aradhya, R. A. Buhrman, D. G. Schlom and D. C. Ralph, "Low-damping sub-10-nm thin films of lutetium iron garnet grown by molecular-beam epitaxy," *Appl. Phys. Lett.,* vol. 109, no. 19, 2016.

[30] R. C. LeCraw, W. G. Nilsen, J. P. Remeika and J. H. van Vleck, "Ferromagnetic Relaxation in Europium Iron Garnet," *Phys. Rev. Lett.,* vol. 11, no. 11, 1963.

[31] R. Skomski, H. P. Oepen and J. Kirschner, "Unidirectional anisotropy in ultrathin transition-metal films," *Phys. Rev. B,* vol. 58, no. 17, 1998.

[32] I. Barsukov, P. Landeros, R. Meckenstock, J. Lindner, D. Spoddig, Z. A. Li, B. Krumme, H. Wende, D. L. Mills and M. Farle, "Tuning magnetic relaxation by oblique deposition," *Phys. Rev. B,* vol. 85, no. 1, 2012.

[33] M. Farle, "Ferromagnetic resonance of ultrathin metallic layers," *Reg. Prog. Phys.,* vol. 61, 1998.

[34] K. Uchida, S. Takahashi, K. Harii, J. Ieda, W. Koshibae, K. Ando, S. Maekawa and E. Saitoh, "Observation of the spin Seebeck effect," *Nature,* vol. 455, no. 7214, 2008.

[35] S. Y. Huang, W. G. Wang, S. F. Lee, J. Kwo and C. L. Chien, "Intrinsic Spin-Dependent Thermal Transport," *Phys. Rev. Lett.,* vol. 107, no. 216604, 2011.

[36] K. Uchida, H. Adachi, T. Ota, H. Nakayama, S. Maekawa and E. Saitoh, "Observation of longitudinal spin-Seebeck effect in magnetic insulators," *Appl. Phys. Lett.,* vol. 97, no. 172505, 2010.

[37] Y. Tserkovnyak, A. Brataas and G. E. Bauer, "Enhanced Gilbert Damping in Thin Ferromagnetic Films Yaroslav," *Phys. Rev. Lett.,* vol. 88, no. 11, 2002.

[38] E. Saitoh, M. Ueda, H. Miyajima and G. Tatara, "Conversion of spin current into charge current at room temperature: Inverse spin-Hall effect," *Appl. Phys. Lett.,* vol. 88, no. 182509, 2006.

[39] Y. Xia, D. Qian, D. Hsieh, L. Wray, A. Pal, H. Lin, A. Bansil, D. Grauer, Y. S. Hor, R. J. Cava and M. Z. Hasan, "Observation of a large-gap topological-insulator class with a single Dirac cone on the surface," *Nat. Phys.,* vol. 5, no. 6, 2009.

[40] Y. L. Chen, J. G. Analytis, J. H. Chu, Z. K. Liu, S. K. Mo, X. L. Qi, H. J. Zhang, D. H. Lu, X. Dai, Z. Fang, S. C. Zhang, I. R. Fisher, Z. Hussain and Z. X. Shen, "Experimental Realization of a Three-Dimensional Topological Insulator, Bi2Te3," *Science,* vol. 325, no. 5937, 2009.

[41] Y. Shiomi, K. Nomura, Y. Kajiwara, K. Eto, M. Novak, K. Segawa, Y. Ando and E. Saitoh, "Spin-Electricity Conversion Induced by Spin Injection into Topological Insulators," *Phys. Rev. Lett.,* vol. 113, no. 196601, 2014.

[42] H. L. Wang, J. Kally, J. S. Lee, T. Liu, H. C. Chang, D. Reifsnyder-Hickey, K. A. Mkhoyan, M. Z. Wu, A. Richardella and N. Samarth, "Surface-State-Dominated Spin-Charge Current Conversion in Topological-Insulator–Ferromagnetic-Insulator Heterostructures," *Phys. Rev. Lett.,* vol. 117, no. 7, 2016.

[43] A. R. Mellnik, J. S. Lee, A. Richardella, J. L. Grab, P. J. Mintun, M. H. Fischer, A. Vaezi, A. Manchon, E. A. Kim, N. Samarth and D. C. Ralph, "Spin-transfer torque generated by a topological insulator," *Nature,* vol. 511, no. 7510, 2014.

[44] Z. L. Jiang, C. Z. Chang, M. R. Masir, C. Tang, Y. D. Xu, J. S. Moodera, A. H. MacDonald and J. Shi, "Enhanced spin Seebeck effect signal due to spin-momentum locked topological surface states," *Nat. Commun.,* vol. 7, no. May, p. 11458, 2016.

[45] Z. L. Jiang, C. Z. Chang, C. Tang, P. Wei, J. S. Moodera and J. Shi, "Independent Tuning of Electronic Properties and Induced Ferromagnetism in Topological Insulators with Heterostructure Approach," *Nano Lett.,* vol. 15, no. 9, pp. 5835-5840, 2015.

[46] J. Robertson, "High dielectric constant oxides," *Eur. Phys. J.,* vol. 28, no. 3, 2004.

[47] F. Yang, A. A. Tasking, S. Sasaki, K. Segawa, Y. Ohno, K. Matsumoto and Y. Ando, "Dual-Gated Topological Insulator Thin-Film Device for Efficient Fermi-Level Tuning," *ACS Nano,* vol. 9, no. 4, pp. 4050-4055, 2015.

[48] M. Aldosary, J. X. Li, C. Tang, Y. D. Xu, J. G. Zheng, K. N. Bozhilov and J. Shi, "Platinum/yttrium iron garnet inverted structures for spin current transport," *Appl. Phys. Lett.,* vol. 108, no. 24, 2016.

[49] C. Z. Chang, J. S. Zhang, X. Feng, J. Shen, Z. C. Zhang, M. H. Guo, K. Li, Y. B. Ou, P. Wei, L. L. Wang, Z. Q. Ji, Y. Feng, S. H. Ji, X. Chen, J. F. Jia, X. Dai, Z. Fang, S. C. Zhang, K. He, Y. Y. Wang, L. Lu, X. C. Ma and Q. K. Xue, "Experimental Observation of the Quantum Anomalous Hall Effect in a Magnetic Topological Insulator," *Science,* vol. 340, no. 6129, 2013.

[50] C. Z. Chang, W. W. Zhao, D. Y. Kim, H. J. Zhang, B. A. Assaf, D. Heiman, S. C. Zhang, C. X. Liu, M. H. W. Chan and J. S. Moodera, "High-precision realization of robust quantum anomalous Hall state in a hard ferromagnetic topological insulator," *Nat. Mater.,* vol. 14, no. 4204, 2015.

[51] J. G. Connell, B. J. Isaac, G. B. Ekanayake, D. R. Strachan and S. S. Seo, "Preparation of atomically flat SrTiO3 surfaces using a deionized-water leaching and thermal annealing procedure," *Apl. Phys. Lett.,* vol. 101, no. 25, 2012.

[52] M. Harder, Y. S. Gui and C. M. Hu, "Electrical detection of magnetization dynamics via spin rectification effects," *Phys. Rep.,* vol. 661, no. 1, 2016.

[53] R. Iguchi and E. Saitoh, "Measurement of Spin Pumping Voltage Separated from Extrinsic Microwave Effects," *J. Phys. Soc. Jpn.,* vol. 86, no. 011003, 2017.

[54] H. Kurebayashi, O. Dzyapko, V. E. Demidov, D. Fang, A. J. Ferguson and S. O. Demokritov, "Controlled enhancement of spin-current emission by three-magnon splitting," *Nat. Mater.,* vol. 10, no. 9, 2011.

[55] Y. S. Chen, J. G. Lin, S. Y. Huang and C. L. Chien, "Incoherent spin pumping from YIG single crystals," *Phys. Rev. B,* vol. 99, no. 220402(R), 2019.

[56] S. Geprägs, A. Kehlberger, F. della Coletta, Z. Qiu, E. J. Guo, T. Schulz, C. Mix, S. Meyer, A. Kamra, M. Althammer, H. Huebl, G. Jakob, Y. Ohnuma, H. Adachi, J. Barker, S. Maekawa, G. E. Bauer, E. Saitoh, R. Gross, S. T. Goennenwein and M. Kläui, "Origin of the spin Seebeck effect in compensated ferrimagnets," *Nat. Comm.,* vol. 7, 2016.

[57] E. Sawatzky and E. Kay, "Some Magnetic and Structural Properties of Epitaxial Garnet Films Prepared by rf Sputtering," *J. Appl. Phys.,* vol. 40, no. 3, 1969.

[58] A. Landé, "Über den anomalen Zeemaneifekt (Teil I).," *Z. Phys.,* vol. 5, no. 4, 1921.

[59] V. Baltz, A. Manchon, M. Tsoi, T. Moriyama, T. Ono and Y. Tserkovnyak, "Antiferromagnetic spintronics," *Rev. Mod. Phys.,* vol. 90, no. 1, 2018.

[60] A. Prakash, J. Brangham, F. Y. Yang and J. P. Heremans, "Spin Seebeck effect through antiferromagnetic NiO," *Phys. Rev. B,* vol. 94, no. 1, 2016.

[61] W. W. Lin, K. Chen, S. F. Zhang and C. L. Chien, "Enhancement of Thermally Injected Spin Current through an Antiferromagnetic Insulator," *Phys. Rev. Lett.,* vol. 116, no. 18, 2016.

[62] Z. Y. Qiu, J. Li, D. Z. H., E. Arenholz, A. T. N'Diaye, A. Tan, K. Uchida, K. Sato, S. Okamoto, Y. Tserkovnyak, Z. Q. Qiu and E. Saitoh, "Spin-current probe for phase transition in an insulator," *Nat. Comm.,* vol. 7, no. 1, 2016.

[63] T. Iino, T. Moriyama, H. Iwaki, H. Aono, Y. Shiratsuchi and T. Ono, "Resistive detection of the Néel temperature of Cr2O3 thin films," *Appl. Phys. Lett.,* vol. 114, no. 2, 2019.

[64] Z. Y. Qiu, D. Z. Hou, J. Barker, K. Yamamoto, O. Gomonay and E. Saitoh, "Spin colossal magnetoresistance in an antiferromagnetic insulator," *Nat. Mater.,* vol. 17, no. 7, 2018.

[65] C. L. Jermain, S. V. Aradhya, N. D. Reynolds, R. A. Buhrman, J. T. Brangham, M. R. Page, P. C. Hammel, F. Y. Yang and D. C. Ralph, "Increased low-temperature damping in yttrium iron garnet thin films," *Phys. Rev. B.,* vol. 95, no. 17, 2017.

[66] S. Foner, "High-Field Antiferromagnetic Resonance in Cr2O3," *Phys. Rev.,* vol. 130, no. 1, 1963.

[67] Z. Y. Wang, C. Tang, R. Sachs, Y. Barlas and J. Shi, "Proximity-Induced Ferromagnetism in Graphene Revealed by the Anomalous Hall Effect," *Phys. Rev. Lett.,* vol. 114, no. 1, p. 016603, 2015.

[68] K. Uchida, J. Xiao, H. Adachi, J. Ohe, S. Takahashi, J. Ieda, T. Ota, Y. Kajiwara, H. Umezawa, H. Kawai, G. E. Bauer, S. Maekawa and E. Saitoh, "Spin Seebeck insulator," *Nat. Mater.,* vol. 9, pp. 894-897, 2010.

[69] J. X. Li, Y. D. Xu, M. Aldosary, C. Tang, Z. S. Lin, S. F. Zhang, R. Lake and J. Shi, "Observation of magnon-mediated current drag in Pt/yttrium iron garnet/Pt(Ta) trilayers," *Nat. Commun.,* vol. 7, p. 10858, 2016.